Nuclear Argonaute protein NRDE-3 switches small RNA partners during embryogenesis to mediate temporal-specific gene regulatory activity

Shihui Chen and Carolyn M. Phillips

Affiliations

[1] Department of Biological Sciences, University of Southern California, Los Angeles, CA 90089

Corresponding author: Carolyn M. Phillips, Department of Biological Sciences, University of Southern California, 1050 Childs Way RRI 201, Los Angeles, CA 90089-2910. Email: cphil@usc.edu

Abstract

RNA interference (RNAi) is a conserved gene regulation mechanism that utilizes the Argonaute protein and their associated small RNAs to exert regulatory function on complementary transcripts. While the majority of germline-expressed RNAi pathway components reside in perinuclear germ granules, it is unknown whether and how RNAi pathways are spatially organized in other cell types. Here we find that the small RNA biogenesis machinery is spatially and temporally organized during embryogenesis. Specifically, the RNAi factor, SIMR-1, forms visible concentrates during mid-embryogenesis that contain an RNA-dependent RNA polymerase, a poly-UG polymerase, and the unloaded nuclear Argonaute protein, NRDE-3. We also observe that many other RNAi factors form foci in embryonic cells distinct from "SIMR granules", including the Argonaute protein CSR-1, underscoring a potential role for cytoplasmic concentrates of RNAi factors to promote gene regulation in embryos. Curiously, coincident with the appearance of the SIMR granules, the small RNAs bound to NRDE-3 switch from predominantly CSR-class 22G-RNAs to ERGO-dependent 22G-RNAs. Prior work has shown that NRDE-3 binds ERGO-dependent 22G-RNAs in the somatic cells of larvae and adults to silence ERGO-target genes; here we demonstrate that NRDE-3-bound, CSR-class 22G-RNAs repress transcription in oocytes. Thus, our study defines two separable roles for NRDE-3, targeting germline-expressed genes during oogenesis to promote global transcriptional repression, and switching during embryogenesis to repress recently duplicated genes and retrotransposons in somatic cells, highlighting the plasticity of Argonaute proteins and the need for more precise temporal characterization of Argonaute-small RNA interactions.

Introduction

Precise gene expression is essential for organisms at all developmental stages. Small RNAs and their partners, the Argonaute (AGO) proteins, play an important role in regulating gene expression by targeting and silencing complementary nucleic acid sequences. This small RNA-mediated gene silencing process is known as RNA interference (RNAi) (Fire et al. 1998). The nematode *Caenorhabditis elegans*, distinguished by its expanded Argonaute family and intricate RNAi pathway, is a well-established model organism to study the RNAi pathway. *C. elegans* has 19 functional Argonaute proteins and various classes of small RNAs (Yigit et al. 2006; Seroussi et al. 2023), which is greatly expanded compared to 8 Argonaute proteins in mammals, 5 in *Drosophila melanogaster*, and 1 in *Schizosaccharomyces pombe* (Höck and Meister 2008). This expansion of the Argonaute family in nematodes may be linked to the diversity of habitats in which nematodes reside and environmental cues to which they must respond. First, RNAi has been

well-studied in plants for its role as an antiviral defense mechanism (Ding et al. 2004); and like plants, worms lack an adaptive immune system, making the RNAi system a primary means to respond to viral intruders (Félix et al. 2011; Ashe et al. 2013; Sarkies and Miska 2013). Second, nematodes have a specialized nucleic acid transporter required for the uptake of double-strand (ds)RNA from the intestinal lumen (McEwan et al. 2012; Winston et al. 2007), indicating that environmental sensing mediated by ingested dsRNA is an important aspect of nematode physiology (Sarkies and Miska 2013). Lastly, it has been proposed that Ago diversity and rapid evolution could be linked to the environmental plasticity of nematodes, including the capacity for parasitism and challenges of invading and colonizing a host (Buck and Blaxter 2013). Regardless of the evolutionary origin for the expansion of RNAi pathway proteins in nematodes, these pathways are not only important for a response to the environment, but are essential for the regulation of thousands of endogenous genes. Therefore, untangling the details of RNA silencing in *C. elegans* will shed light on the mechanisms of small RNA-mediated gene regulation in *C. elegans* and other organisms.

Argonaute proteins can be subdivided into three clades. Proteins are grouped into the AGO and PIWI clades based on their similarity to *Arabidopsis thaliana* AGO1 and *Drosophila melanogaster* PIWI, respectively. The third, WAGO, clade represents a nematode-specific expansion of the Argonaute protein family (Yigit et al. 2006). While small RNAs bound by the AGO- and PIWI-clade Argonaute proteins tend to be processed from longer, precursor transcripts, the WAGO-clade Argonaute proteins bind 22-nucleotide, 5'-triphosphorylated small RNAs (22G-RNAs) with which are each de novo synthesized by RNA-dependent RNA polymerases (RdRPs) (Gu et al. 2009; Pak and Fire 2007; Aoki et al. 2007). However, even within the WAGO clade, each of the 11 Argonaute proteins exhibits specificity for a unique group of 22G-RNAs and exhibits distinct tissue and developmental expression patterns (Seroussi et al. 2023). For example, WAGO-1 binds 22G-RNAs that target transposons, pseudogenes, and aberrant transcripts, and silences genes post-transcriptionally in the germline cytoplasm (Gu et al. 2009), while CSR-1 binds 22G-RNAs targeting germline-expressed genes, functioning to clear maternal mRNA in early embryos while licensing and tuning gene expression in the adult germline (Quarato et al. 2021; Gu et al. 2009; Claycomb et al. 2009). Other WAGO Argonautes, such as SAGO-1 and SAGO-2, function exclusively in somatic cells and play roles in regulating endogenous genes, exogenous RNAi, and immunity (Seroussi et al. 2023). Unique amongst the WAGO Argonautes for their nuclear localization are HRDE-1 and NRDE-3, which are thought to silence genes co-transcriptionally in germline and soma respectively, and are required for the inheritance of RNA silencing signals from parents to offspring (Buckley et al. 2012; Guang et al. 2008). Despite

extensive characterization of the *C. elegans* Argonaute proteins, we still know little about the factors that promote the spatiotemporal expression of each Argonaute protein and the mechanisms that promote Argonaute-small RNA binding specificity. Furthermore, most Argonaute-small RNA sequencing experiments have been performed at a single time point, usually in adult *C. elegans*, meaning that we have little understanding as to how the RNA targets of each Argonaute protein change across development.

In the *C. elegans* germline, many of the RNAi components, including Argonaute proteins, RdRPs, and other small RNA processing machinery, localize within phase-separated germ granules. Often, proteins acting in different functional branches of the RNAi pathway seem to reside in separate compartments of the germ granules, suggesting that there are specialized areas within the germ granules where distinct molecular reactions occur. Presently, six sub-compartments of the germ granule have been identified in *C. elegans*: P granules, Z granules, *Mutator* foci, SIMR foci, and more recently, E granules and D granules (Brangwynne et al. 2009; Phillips et al. 2012; Wan et al. 2018; Manage et al. 2020; Chen et al. 2024; Huang et al. 2024). Processing bodies (P-bodies), a well-characterized condensate that contains proteins associated with mRNA turnover and translationally repressed mRNAs, also closely associate with germ granules (Du et al. 2023). These germ granule compartments are situated at the cytoplasmic side of the nucleus, proximal to nuclear pores. However, the mechanisms governing their spatial organization remain unknown. Moreover, with the majority of studies focusing on mechanisms of RNA silencing and germ granule organization in the germline, there is limited understanding of how each of these germ granule compartments assembles and functions in embryos. It has been observed that in *C. elegans* embryogenesis, the primordial germline cell P4 divides into Z2 and Z3 progenitor germ cells (PGCs) at around the 100-cell stage, coinciding with the demixing of Z granules from P granules, the appearance of *Mutator* foci and SIMR foci, and the initiation of germ cell transcription (Updike and Strome 2010; Uebel et al. 2021; Wan et al. 2018; Seydoux and Dunn 1997). Together, the assembly of this more complex germ granule organization coinciding with a burst of transcription from the germ cells, may indicate that these multi-compartment structures are necessary to monitor the newly synthesized germline transcripts. Yet even these limited studies of RNAi pathway factors in embryos fail to address a role for ribonucleoprotein granules in RNA silencing in the soma.

Here, we discovered that SIMR-1, the founding component of the germline SIMR foci, is also found in cytoplasmic granules in the somatic cells of *C. elegans* embryos. These embryonic “SIMR granules” additionally contain factors involved in 22G-RNA amplification and associated with the nuclear Argonaute protein, NRDE-3. However, NRDE-3 itself only associates with the

SIMR granules when not bound to small RNAs. Strikingly, the SIMR granules exhibit temporal dynamics where they first appear in early embryogenesis (around the 8-cell stage), peak around the 100-cell stage, and have mostly disappeared by the comma stage of embryogenesis. Curiously, these embryonic SIMR granules are by no means the only RNAi-related embryonic granules, as numerous other RNAi factors are found in separate granules in embryos, including components of the CSR pathway, the Argonaute CSR-1 and its RdRP EGO-1. Interestingly, clearance of many of these granules, including the embryonic SIMR, CSR, Z and P granules, is regulated by a common mechanism of autophagic degradation. Furthermore, by sequencing the small RNAs bound by NRDE-3 in early and late embryogenesis, we found that the formation of the SIMR granules coincides with a switch in NRDE-3 small RNA targets, from CSR-class 22G-RNAs to ERGO-class 22G-RNAs. Together, our data demonstrates that NRDE-3 has two separate functions, first acting in oogenesis to repress RNA Polymerase II and promote genome-wide transcription repression, and second acting downstream of ERGO-1 to transcriptionally silence retrotransposons, pseudogenes, and aberrant transcripts. Further, the SIMR granules themselves appear to be sites of NRDE-3-bound 22G-RNA biogenesis and loading and may contribute to the efficiency or specificity of Argonaute-small RNA interactions during embryogenesis.

Results:

SIMR-1 and ENRI-2 localize to cytoplasmic granules during embryogenesis

In previous work, we sought to identify proteins that associate with SIMR-1 and ultimately found that SIMR-1 associates with HRDE-2 and the nuclear Argonaute protein, HRDE-1, to promote correct HRDE-1 small RNA binding in germ cells (Chen and Phillips 2024a). In that work, we also identified another nuclear Argonaute protein, NRDE-3, as an interactor of SIMR-1. NRDE-3 has been shown previously to bind ERGO-dependent 22G-RNAs and silence ERGO-target genes in somatic cells (Figure 1—figure supplement 1 A-B). To delve further into this potential interaction between SIMR-1 and NRDE-3, we first systematically compiled a list of the protein interactions identified from previous studies for both SIMR-1 and NRDE-3 (Figure 1A). Interestingly, the HRDE-2 paralog, ENRI-2, had been shown to interact with both SIMR-1 and NRDE-3 in embryos by immunoprecipitation (IP) followed by mass spectrometry (mass-spec), and another HRDE-2 paralog, ENRI-1, was similarly shown to interact with only NRDE-3 (Lewis et al. 2020). These findings suggest that SIMR-1, NRDE-3, ENRI-2, and possibly ENRI-1 proteins may function together in the somatic nuclear RNAi pathway, analogous to the roles of SIMR-1, HRDE-1, and HRDE-2 in the germline nuclear RNAi pathway.

Here, we first aimed to address whether and where NRDE-3, SIMR-1, ENRI-1, and ENRI-2 colocalize. NRDE-3 has previously been shown to be expressed in the nucleus of most somatic cells (Guang et al. 2008). Until recently, all characterization of NRDE-3 was done using a low-copy, integrated transgenic strain in which the nuclear localization was not visible until the ~30-80-cell stage of development, and it was presumed that this localization reflected the endogenous NRDE-3 localization (Guang et al. 2008; Lewis et al. 2020). However, a more recent study constructed an endogenously-tagged NRDE-3 strain using CRISPR and found that NRDE-3 additionally localizes to the nucleus of oocytes and early embryos (Seroussi et al. 2023, 2022). In a recent study, we addressed this discrepancy, and demonstrated that the older, transgenic NRDE-3 construct is targeted for RNAi-mediated gene silencing in germ cells and early embryos (Chen and Phillips 2024b). SIMR-1 is a component of the SIMR foci, a sub-compartment of germ granules, that appears as punctate foci at the periphery of *C. elegans* germ cells starting in embryos through the adult stage (Manage et al. 2020; Uebel et al. 2021). ENRI-1 has been reported to localize to the cytoplasm of oocytes and embryos while ENRI-2 localized to both the nucleus and cytoplasm, varying depending on developmental stage (Lewis et al. 2020). With these four proteins showing distinct localization patterns from one another, it was unclear how these proteins could physically interact.

To investigate where and how these interactions might potentially occur, we chose to initially examine localization of these proteins in the germline of adult *C. elegans* using the endogenously-tagged NRDE-3 strain which is visible starting in late pachytene. As expected based on previous work, NRDE-3 localizes to the nucleus of germ cells, while SIMR-1 is found in the cytoplasm in SIMR foci, a compartment of the germ granule (Figure 1—figure supplement 2A) (Seroussi et al. 2022, 2023; Manage et al. 2020). Next, we decided to examine NRDE-3 and SIMR-1 localization in embryos, carefully dividing the embryos into distinct developmental stages, from 4-cell to comma stage. As expected, we found that NRDE-3 is consistently localized to the nucleus in all embryonic stages (Figure 1B). Interestingly, we observed that SIMR-1 forms granules in the cytoplasm of somatic cells during some embryonic stages (Figure 1B). By quantifying the total number of granules per embryo across embryonic development, we found that the “SIMR granules” first appear around the 8-cell stage and reach a peak at approximately the 100-cell stage, coinciding with the division of the germline precursor cell P_4 into the primordial germ cells Z_2 and Z_3 (Wang and Seydoux 2013). Subsequently, the number of SIMR granules decreases, and in late embryos, SIMR-1 localizes primarily to the germ granules surrounding the two germ cells, as previously observed (Uebel et al. 2021) (Figure 1B-C). We had previously shown that the Tudor domain of SIMR-1 was important for its assembly into germline SIMR foci.

171 Therefore, we next explored the requirement for the Tudor domain in assembling SIMR-1
172 cytoplasmic granules in embryos (Manage et al. 2020). We found that the Tudor domain mutant,
173 SIMR-1(R159C), fails to assemble in cytoplasmic granules in the embryos (Figure 1—figure
174 supplement 2B), indicating that, similar to germline SIMR foci, the Tudor domain is also required
175 for assembly of the cytoplasmic SIMR granules in embryos.

176 We next focused on ENRI-1 and ENRI-2 and observed that ENRI-2 shows similar
177 cytoplasmic granule localization and colocalizes with SIMR-1 in embryos, but it does not localize
178 to the germ granules in Z_2 and Z_3, suggesting that the activity of ENRI-2 is restricted to somatic
179 cells (Figure 1B). Finally, we examined the localization of N-terminal tagged 2xTy1::GFP::ENRI-
180 1, and could not detect any specific localization in either nuclei or cytoplasmic granules (Figure
181 1—figure supplement 2C) (Lewis et al. 2020). Consequently, we constructed a new strain with C
182 terminal tagged ENRI-1::mCherry::2xHA and confirmed the presence of full-length ENRI-1 protein
183 with Western Blot (Figure 1—figure supplement 2D). Nonetheless, we could not detect any ENRI-
184 1 localization in embryos with our newly generated strain (Figure 1—figure supplement 2C).
185 These results are consistent with the fact that ENRI-1 does not interact directly with either SIMR-
186 1 or ENRI-2 by immunoprecipitation (Figure 1A) (Lewis et al. 2020). Altogether, these data
187 indicate that SIMR-1 and ENRI-2 colocalize at cytoplasmic granules in the somatic cells of
188 embryos and suggest that ENRI-2 and SIMR-1 may function together at these sites. In contrast,
189 NRDE-3 is spatially separated in the nucleus and no clear expression pattern was observed for
190 ENRI-1.
191

192 **Unloaded NRDE-3 associates with SIMR-1 in cytoplasmic granules**

193 Next, to determine whether SIMR-1 and ENRI-2 are required for NRDE-3 localization, we
194 introduced the *simr-1* mutant, *enri-2* mutant, *enri-1* mutant, and *enri-1; enri-2* double mutant in
195 the endogenously tagged GFP::3xFLAG::NRDE-3 strain, and examined NRDE-3 localization
196 across embryonic developmental stages. We observed no changes in NRDE-3 expression or
197 nuclear localization in any of the mutants examined at any developmental stage (Figure 2—figure
198 supplement 1A).

199 In previous work, we demonstrated that the germline nuclear Argonaute protein HRDE-1
200 loses nuclear localization and associates in the cytoplasm with the SIMR compartment of germ
201 granules when it is unable to bind small RNAs (Chen and Phillips 2024a). Additionally, ENRI-2
202 interacts more strongly with NRDE-3 in an *eri-1* mutant background compared to wild-type (Lewis
203 et al. 2020), suggesting that the interaction occurs when NRDE-3 does not bind small RNAs.
204 Localization of unloaded NRDE-3 has been examined in the seam cells of L3 stage animals,

where, like HRDE-1, it loses nuclear localization and becomes restricted to the cytoplasm (Guang et al. 2008). Therefore, we next sought to examine the localization of NRDE-3 when it is unbound to small RNA in embryos and germline. First, we aimed to deplete the preferred small RNA binding partners of NRDE-3. NRDE-3 has previously been shown to bind secondary 22G-RNAs downstream of ERGO-class 26G-RNAs, dependent on ERI-1, which is required for 26G-RNA biogenesis (Guang et al. 2008; Han et al. 2009; Seroussi et al. 2023), and RDE-3/MUT-2, which is a component of the *Mutator* complex and necessary for 22G-RNA production (Chen et al. 2005; Phillips et al. 2012, 2014) (Figure 1—figure supplement 1A-B). Therefore, we introduced an *eri-1* mutant and a *rde-3/mut-2* mutant into the endogenously GFP-tagged NRDE-3 background. We observed that NRDE-3 associates with somatic granules with a similar spatiotemporal pattern to SIMR-1 and ENRI-2, peaking around the 100-cell stage, although the total number of granules per embryo is lower for NRDE-3 granules in the *eri-1* and *rde-3/mut-2* mutant backgrounds compared to SIMR granules (Figure 2A-B). Next, to fully abolish the small RNA binding capacity of NRDE-3 and to confirm that the observed granule localization was due to the loss of small RNA loading, we introduced mutations to abolish small RNA binding into the GFP-tagged NRDE-3; specifically, residues 687H and 691K in the Mid domain were mutated to alanine, hereafter referred to as NRDE-3(HK-AA) (Ma et al. 2005; Guang et al. 2008; Chen and Phillips 2024a). NRDE-3(HK-AA) localizes exclusively to the cytoplasm across embryonic development and in the adult germline, accumulating in somatic granules at 100-cell stage similar to SIMR-1 and ENRI-2 (Figure 2A). Quantification of the number of NRDE-3 granules per embryo in the NRDE-3(HK-AA) strain shows that the dynamics of NRDE-3 granule appearance and disappearance are similar to that of SIMR-1, where the number of granules increases from early embryos up until about 100-cell stage and then decreases as the embryos progress to later stages of development (Figure 2C). Overall, the total number of NRDE-3(HK-AA) granules quantified per embryo are similar to or modestly higher than SIMR-1 granules (Figure 1C, Figure 2C). Western blot analysis reveals that overall protein level are similar for wild-type NRDE-3 and NRDE-3(HK-AA) (Figure 2—figure supplement 1B), indicating that unloaded NRDE-3 is not subject to degradation. This result contrasts with our previous results for unloaded HRDE-1 (HRDE-1(HK-AA), which does show reduced protein expression compared to wild-type HRDE-1 (Chen and Phillips 2024a). Together, these data indicate that NRDE-3 forms granules in the cytoplasm of somatic cells when not associated with a small RNA binding partner.

It is also worth noting that despite the similarity in timing of NRDE-3 granule appearance and disappearance in the *eri-1* and *rde-3* mutants compared to the *nrde-3(HK-AA)* mutant, we observed a striking difference in the NRDE-3 localization in early embryos. Specifically, in *eri-1*

239 and *rde-3* mutants, NRDE-3 localizes to the nucleus in early embryos while NRDE-3(HK-AA)
240 localizes exclusively to the cytoplasm (Figure 2A). Similarly, in the Z2 and Z3 primordial germ
241 cells of late embryos, NRDE-3 is still found in the nucleus in *eri-1* and *rde-3* mutants. In contrast,
242 NRDE-3 localizes exclusively to the cytoplasm in the somatic cells of late embryos of all three
243 mutants. This result suggests that there may be a fundamental difference in the small RNAs
244 bound by NRDE-3 in early compared to late embryos, and that the small RNAs bound by NRDE-
245 3 in early embryos are produced independently of ERI-1 and RDE-3.
246 To determine whether unloaded NRDE-3 localizes to SIMR granules, we examined the
247 localization of SIMR-1 and NRDE-3 together in the *nrde-3(HK-AA)* mutant and *eri-1* mutant
248 backgrounds. We found that SIMR-1 colocalizes with unloaded NRDE-3 in embryonic granules
249 (Figure 2D, Figure 2—figure supplement 1C). Further, the SIMR granules in the *nrde-3(HK-AA)*
250 mutant background exhibit dynamics similar to the wild-type background (Figure 2—figure
251 supplement 1D), indicating that *nrde-3(HK-AA)* does not affect the localization of SIMR-1.
252 Interestingly, NRDE-3(HK-AA) does not form granules in germ cells and is instead present
253 exclusively in the cytoplasm, thus it does not colocalize with the SIMR compartment of germ
254 granules (Figure 2—figure supplement 1E). These results demonstrate that unloaded NRDE-3
255 associates with SIMR-1 and ENRI-2 in cytoplasmic granules in the somatic cells of *C. elegans*
256 embryos, indicating a potential role for SIMR-1 in the NRDE-3 nuclear RNAi pathway.
257
258 **SIMR-1 and ENRI-2 recruit unloaded NRDE-3 to cytoplasmic granules**
259 As previously described, unloaded NRDE-3 localizes to cytoplasmic granules in embryos
260 and colocalizes with SIMR-1. Next, we aimed to determine whether SIMR-1 and ENRI-2 are
261 required for the NRDE-3 granule localization. To this end, we introduced a *simr-1* mutant and an
262 *enri-2* mutant into the GFP-tagged NRDE-3(HK-AA) strain and assessed NRDE-3(HK-AA)
263 localization. Strikingly, we found that NRDE-3(HK-AA) granules disappear completely and NRDE-
264 3(HK-AA) is instead found exclusively in the cytoplasm in all cells across all embryonic stages
265 (Figure 3A). Similarly, in a *simr-1; eri-1* double mutant, NRDE-3 granules are absent though
266 NRDE-3 remains in the nucleus in early embryos (Figure 3A), similar to NRDE-3 expression in
267 the *eri-1* single mutant (Figure 2A). However, neither wild-type NRDE-3 nor NRDE-3(HK-AA)
268 protein levels are affected by loss of *simr-1* (Figure 3—figure supplement 1A), indicating that loss
269 of granule localization in *nrde-3(HK-AA); simr-1* is not due to reduced NRDE-3 protein expression.
270 These results demonstrate that both SIMR-1 and ENRI-2 are required for the recruitment of
271 NRDE-3 to cytoplasmic granules.

To investigate the dependence of SIMR-1 and ENRI-2 on one another, we examined ENRI-2 localization in a *simr-1* mutant and SIMR-1 localization in an *enri-2* mutant. We found that ENRI-2 granules are lost in the *simr-1* mutant, while SIMR-1 granules are still present in the *enri-2* mutant, indicating that SIMR-1 functions upstream of ENRI-2 for granule assembly (Figure 3B).

To further assess whether ENRI-1 plays a role in the accumulation of unloaded NRDE-3 in cytoplasmic granules, we introduced an *enri-1* mutant into the GFP-tagged NRDE-3(HK-AA) strain and found that NRDE-3 association with cytoplasmic granules was not disrupted (Figure 3—figure supplement 1B). We further examined NRDE-3(HK-AA) granule association in the *enri-1; enri-2* double mutant and found it to be fully cytoplasmic, indistinguishable from the *enri-2* single mutant (Figure 3—figure supplement 1B). While we had already determined that ENRI-1::mCherry did not form visible foci in embryos; to rule out the possibility of partial redundancy between ENRI-1 and ENRI-2, we introduced an *enri-2* mutant into the mCherry-tagged ENRI-1 strain but still unable to detect any distinct ENRI-1 expression (Figure 3—figure supplement 1C). Lastly, to determine if NRDE-3 recruitment to granules could alter ENRI-1 localization, we introduced the mCherry-tagged ENRI-1 into the GFP-tagged NRDE-3(HK-AA) strain, and still we could not see any granule localization for ENRI-1 (Figure 3—figure supplement 1D). Therefore, we excluded ENRI-1 from further investigation, and conclude that SIMR-1 and ENRI-2, but not ENRI-1, recruit unloaded NRDE-3 to cytoplasmic granules, with SIMR-1 also acting to recruit ENRI-2.

SIMR-1 does not localize to P bodies or other previously identified embryonic granules

A variety of RNA-associated proteins have previously been shown to form granules in *C. elegans* embryos. To determine whether the SIMR-1, ENRI-2, and unloaded NRDE-3 granules that we have observed coincide with a previously identified granule, we examined the colocalization between SIMR-1 and all other embryonic granule-associated proteins that we could identify. It is well known that Processing (P) bodies, the condensates of translationally inactive mRNAs and proteins, localize to cytoplasmic foci of soma in *C. elegans* embryos (Parker and Sheth 2007; Gallo et al. 2008). To examine if the SIMR-1 cytoplasmic granules are P bodies, we examined the localization of SIMR-1 and CGH-1, a core P body component, using a strain expressing GFP-tagged SIMR-1 and mCherry-tagged CGH-1 (Du et al. 2023). We found that CGH-1 does not colocalize with SIMR-1 (Figure 4—figure supplement 1A). CGH-1 also does not colocalize with NRDE-3 cytoplasmic granules in the *eri-1* mutant (Figure 4—figure supplement 1B). Together, these data indicate that the cytoplasmic SIMR granules found in embryos are not P bodies.

306 Next, we examined two proteins previously shown to colocalize with SIMR foci in the germ
307 cells of adult animals, RSD-2 and HRDE-2 (Manage et al. 2020; Chen and Phillips 2024a). RSD-
308 2 is a small RNA factor required for the response to low doses of exogenously-introduced double-
309 stranded RNA (Sakaguchi et al. 2014; Han et al. 2008; Tijsterman et al. 2004; Zhang et al. 2012)
310 and HRDE-2 is a factor critical for RNAi inheritance that promotes correct small RNA loading into
311 the nuclear Argonaute HRDE-1 (Chen and Phillips 2024a; Spracklin et al. 2017). However, we
312 did not observe any granule localization for RSD-2 and HRDE-2 in embryos (Figure 4—figure
313 supplement 1C-D). In addition, SIMR-1 cytoplasmic granules were not affected by the loss of
314 *hrde-2* (Figure 4—figure supplement 1E). These results suggest that HRDE-2 and RSD-2 do not
315 function together with SIMR-1, ENRI-2, and NRDE-3 in embryonic granules and indicate that
316 embryonic SIMR granules and the SIMR compartment of germ granules are distinct, each
317 containing a unique set of proteins.
318 RDE-12 interacts with Argonaute proteins and RNAi-targeted mRNAs, and has also been
319 shown to localize to cytoplasmic granules in the somatic cells of *C. elegans* embryos (Shirayama
320 et al. 2014; Yang et al. 2014). We next assessed the localization of mCherry-tagged SIMR-1
321 relative to GFP-tagged RDE-12 and found that they do not colocalize (Figure 4—figure
322 supplement 1F). RSD-6 is a Tudor domain-containing RNAi factor that partially colocalizes with
323 RDE-12 in the R2 bodies in adult germ cells (Yang et al. 2014; Sakaguchi et al. 2014; Zhang et
324 al. 2012). We examined the expression of GFP-tagged RSD-6 in embryos and, while we did
325 observe RSD-6 at granules in somatic cells, no colocalization with mCherry-tagged SIMR-1 could
326 be detected (Figure 4—figure supplement 1G). The RNAi-inheritance factor and defining member
327 of the Z compartment of the germ granule, ZNFX-1, has also been observed in cytoplasmic
328 granules in the somatic cells of embryos (Wan et al. 2018; Ouyang et al. 2019), however these
329 somatic ZNFX-1 granules also fail to colocalize with SIMR-1 (Figure 4—figure supplement 1H).
330 Finally, we compared SIMR-1 localization to peri-centrosomal foci marked tubulin, based on a
331 recent report that NRDE-3 accumulates at these foci (Jin et al. 2024), but we did not observe any
332 colocalization between SIMR-1 and tubulin in a wild-type background (Figure 4—figure
333 supplement 1I). Altogether, we found that SIMR-1 fails to localize to any previously characterized
334 embryonic granules. These results further indicate that there are numerous granule-localized
335 proteins in the somatic cells of embryos, such as RDE-12, RSD-6, and ZNFX-1, which may play
336 important roles in the RNA biology of early embryos.
337
338 **Multiple *Mutator* complex proteins localize to SIMR granules in embryos**

339 *Mutator* foci localize adjacent to SIMR foci in the adult germline (Manage et al. 2020; Chen
340 and Phillips 2024a), so we next investigated the localization of *Mutator* components in embryos.
341 We first examined *Mutator* foci component RDE-3/MUT-2, a poly(UG) polymerase required for
342 WAGO-class 22G-RNA production (Figure 1—figure supplement 1A-B) (Phillips et al. 2012;
343 Shukla et al. 2020) and found that GFP-tagged RDE-3 is prominently localized to cytoplasmic
344 granules in embryos that colocalize with SIMR-1 (Figure 4A-B). This colocalization led us to the
345 hypothesis that SIMR-1 cytoplasmic granules are sites of WAGO-class 22G-RNA biogenesis.
346 Therefore, we speculated that more small RNA production machinery might be localized with
347 SIMR-1 at these cytoplasmic granules. We next examined the RNA-dependent-RNA-polymerase
348 (RdRP) RRF-1, which synthesizes WAGO-class 22G-RNAs and localizes to *Mutator* foci in the
349 adult germline (Figure 1—figure supplement 1A-B) (Sijen et al. 2001; Gent et al. 2010; Vasale et
350 al. 2010; Phillips et al. 2012). As we predicted, RRF-1 also colocalizes with SIMR-1 in somatic
351 granules (Figure 4B-C), and it fails to localize to somatic granules in the *simr-1* mutant (Figure
352 4D).
353 MUT-16 is the scaffolding protein for germline *Mutator* foci, thus we next investigated
354 whether MUT-16 similarly scaffolds the cytoplasmic SIMR granules in early embryos (Phillips et
355 al. 2012). We found that MUT-16 can be observed in cytoplasmic granules in the embryonic
356 somatic cells (Figure 4—figure supplement 1J), similar to what has been observed in a previous
357 study (Ouyang et al. 2019), and both SIMR-1 and RDE-3 fail to assemble into cytoplasmic
358 granules in the *mut-16* mutant (Figure 4E, Figure 4—figure supplement 1K). Notably, the germ
359 granule association of SIMR-1 is unaffected, as SIMR-1 still localizes to germ granules at comma
360 stage embryos and in the adult germline (Figure 4E) (Manage et al. 2020). Together, these data
361 indicate that MUT-16 functions upstream of SIMR-1 and mediates the assembly of cytoplasmic
362 granules in embryos. It is curious to note that, in a *mut-16* mutant where SIMR-1 association with
363 cytoplasmic granules is lost in the somatic cells, SIMR-1 instead associates with mitotic spindles
364 (Figure 4E), similar to the localization observed for NRDE-3 in embryos (Jin et al. 2024). To
365 conclude, we have shown that the SIMR granules found in the somatic cells of early embryos
366 contain the biogenesis machinery for WAGO-class 22G-RNAs, including RDE-3 and RRF-1, and
367 depend on the scaffolding protein MUT-16 for assembly (Figure 4J). The differential requirement
368 for MUT-16 on the assembly of somatic and germline SIMR granules highlights a key difference
369 between these two compartments, which have some parallel functions but distinct composition.
370
371 **CSR-1 and EGO-1 associate with a distinct type of granule in early embryos**

372 The Argonaute protein CSR-1 has also been previously seen at cytoplasmic granules in
373 the soma of early embryos, a time at which CSR-1 is functioning to clear maternal-inherited
374 mRNAs (Quarato et al. 2021; Seroussi et al. 2023; Ouyang et al. 2019). Using a GFP-tagged
375 CSR-1 strain we constructed previously (Nguyen and Phillips 2021), we confirmed that CSR-1
376 forms prominent cytoplasmic granules in embryos visible prior to the 4-cell stage and present
377 through 100-cell stage embryos, but disappear by the 200-cell stage, at which point only germ
378 granule localization is visible (Figure 4F). Quantification of the total number of "CSR granules" per
379 embryo across development shows that the CSR granules are more abundant than the SIMR-1
380 and NRDE-3(HK-AA) granules and differ in the timing of their appearance and disappearance
381 relative to SIMR-1 and NRDE-3(HK-AA) granules (Figure 1C, 2C, 4G). Specifically, CSR granules
382 appear earlier and peak at the 28-cell stage, while SIMR-1 and NRDE-3(HK-AA) granules appear
383 between 8- and 28-cell stages and peak at the 100-cell stage (Figure 1C, 2C, 4G). The small
384 RNAs bound by CSR-1 are synthesized by the RdRP, EGO-1, so we next assessed the
385 localization of EGO-1 in early embryos. We found that EGO-1 colocalizes with CSR-1 in the
386 somatic CSR granules (Figure 4B,H) and neither CSR-1 nor EGO-1 fully colocalizes with SIMR-
387 1, although we occasionally observed adjacent localization between SIMR-1 and CSR-1 (Figure
388 4B,I, Figure 4—figure supplement 1L). Lastly, unlike RRF-1 which requires SIMR-1 to localize to
389 embryonic foci, EGO-1 localizes to cytoplasmic granules in the absence of *simr-1* (Figure 4D).
390 Together, our results show that the RdRPs, RRF-1 and EGO-1, localize to different cytoplasmic
391 granules in the somatic cells of *C. elegans* embryos, where they colocalize with Argonaute
392 proteins, NRDE-3 and CSR-1, respectively. Thus, we postulate that WAGO-class and CSR-class
393 22G-RNA biogenesis and loading are compartmentalized into cytoplasmic granules, differing from
394 one another both spatially and temporally, in the somatic cells of early embryos (Figure 4J).
395

396 **Autophagy regulates the removal of SIMR granules and other cytoplasmic granules during**
397 **embryogenesis**

398 Both SIMR and CSR granules exhibit dynamic expression patterns across embryonic
399 development, where the granules increase in abundance from early to mid-embryogenesis, and
400 then subsequently disappear from somatic cells, becoming restricted to germ cells by late
401 embryogenesis (Figure 1B-C, Figure 4F-G). In contrast, P granules become enriched at the
402 posterior half of one-cell embryos and are subsequently partitioned with the germline progenitor
403 cells through the remainder of embryonic development (Strome and Wood 1983). Previous work
404 has shown that autophagic degradation is one mechanism by which P granules are removed from
405 somatic blastomeres (Zhang et al. 2009). Autophagy, often referred to as the 'self-eating'

406 pathway, is one of the two major protein degradation systems in eukaryotic cells. Autophagy
407 involves the formation of autophagosomes, which engulf cytoplasmic structures and proteins and
408 deliver the contents to lysosomes for degradation (Klionsky 2005; Mizushima 2007). In contrast,
409 the ubiquitin-proteasome system degrades proteins though ubiquitination and degradation by the
410 26S proteosome complex, bypassing lysosomes (Nedelsky et al. 2008). In the absence of the
411 autophagy protein LGG-1, the *C. elegans* ortholog of *S. cerevisiae* Atg8, the core P granule
412 proteins PGL-1 and PGL-3 are ectopically expressed in somatic foci during mid to late
413 embryogenesis (Zhang et al. 2009). So we sought to test whether the removal of SIMR and CSR
414 granules from the somatic cells during mid-to-late embryogenesis might similarly depend on the
415 autophagy pathway.

416 To address this possibility, we first examined the expression of PGL-1 and SIMR-1 at 8-
417 cell, 100-cell, and comma stages of embryogenesis following *lgg-1* or control (L4440) RNAi
418 treatment of the parental animals. Consistent with previous work (Zhang et al. 2009), RNAi of *lgg-*
419 *1* leads to ectopic expression of PGL-1 in cytoplasmic foci of the somatic cells at mid (100-cell)
420 and late (comma) embryonic stages, while its germ granule localization remains unaffected
421 (Figure 5A). Similarly, we found that the number of somatic SIMR granules at the 100-cell stage
422 increases by approximately 2-fold in *lgg-1* RNAi-treated embryos compared to control (L4440)
423 (Figure 5A-B). Further, in the comma stage, somatic SIMR granules remain in the soma in *lgg-1*
424 RNAi-treated embryos, whereas SIMR granules are cleared from the somatic cells and restricted
425 to germ cells in control (L4440) RNAi-treated embryos (Figure 5A). Examination of other somatic
426 SIMR granule-associated proteins, including ENRI-2, RDE-3, and RRF-1, and unloaded NRDE-
427 3 revealed that they also exhibit ectopic expression in the somatic cells of comma-stage embryos
428 and continue to colocalize with SIMR-1 (Figure 5—figure supplement 1A-B). These findings
429 indicate that the removal of SIMR granules from somatic cells during mid and late embryogenesis
430 is regulated by autophagy, similar to the role of autophagy in the degradation of P granules form
431 early somatic blastomeres.

432 Since both SIMR granules and P granules are regulated by the autophagy pathway during
433 embryogenesis, we also examined the role for autophagy in regulating other granule-associated
434 proteins in early embryos, specifically CSR-1 and ZNFX-1. Similar to PGL-1 and SIMR-1, CSR-1
435 and ZNFX-1 show increased numbers of somatic granules in 100-cell and comma stage embryos
436 following parental treatment with *lgg-1* RNAi compared to control (L4440) (Figure 5C). To further
437 investigate the spatial organization of these somatic granules in the absence of autophagy-
438 mediated degradation, we examined the 100-cell stage embryos following *lgg-1* RNAi treatment
439 using strains expressing PGL-1::BFP; SIMR-1::GFP; RFP::ZNFX-1, and GFP::CSR-1; SIMR-

440 1::mCherry. Interestingly, these proteins display a variety of configurations relative to one another,
441 distinct from their typical organization in the germline (Uebel et al. 2023). These configurations
442 included granules composed of individual protein, multiple proteins adjacent to one another, and
443 large aggregates composed of multiple proteins (Figure 5D). We speculate that many of the PGL-
444 1-containing granules, including the larger aggregates, are associated with autophagosomes, as
445 has been shown previously (Zhang et al. 2009). Overall, our findings demonstrate that the
446 autophagy pathway is utilized to regulate the spatial-temporal expression of many embryonic
447 granule-associated proteins, including proteins found in P, Z, SIMR, and CSR granules. Further,
448 it is worth noting that P, Z, SIMR, and CSR granules are not all removed at the same
449 developmental timepoint (for example, Figure 1C, 4G), suggesting the presence of additional
450 regulatory mechanisms controlling the timing of their degradation.
451
452 **NRDE-3 switches small RNA partners during embryonic development**
453 The nuclear localization of NRDE-3 in the somatic cells of larvae depends on ERGO-1
454 and other proteins required for the biogenesis of ERGO-class 26G-RNAs (Figure 1—figure
455 supplement 1A-B) (Guang et al. 2008). Sequencing of NRDE-3-bound 22G-RNAs at the L4 to
456 young adult transition identifies a set of endogenous targets that overlaps substantially with those
457 of ERGO-1 (Seroussi et al. 2023). Together, these data have led to the conclusion that NRDE-3
458 acts downstream of ERGO-1 to transcriptionally silence ERGO-target genes. Yet our data looking
459 at the nuclear localization of NRDE-3 in embryos, demonstrate that this model may be an
460 incomplete picture. Specifically, in *eri-1* and *rde-3* mutants where 26G-RNA or WAGO-class 22G-
461 RNA biogenesis are abolished, respectively, NRDE-3 remains localized to the nucleus in early
462 embryos (Figure 2A). The small RNA binding-defective NRDE-3(HK-AA) is localized exclusively
463 to the cytoplasm at the same time point, indicating that small RNA binding is critical for nuclear
464 import at this stage (Figure 2A). Accordingly, we must postulate that NRDE-3 binds another class
465 of small RNA to promote nuclear entry in very early embryos. To investigate the identity of NRDE-
466 3-bound small RNAs across embryonic development and to explore the role of the SIMR granules
467 in promoting NRDE-3 small RNA binding, we immunoprecipitated NRDE-3 and sequenced
468 associated small RNAs (IP-sRNA seq) in early embryos (<=100-cell) and late embryos (>=300-
469 cell) in wild-type, *eri-1* mutant, *simr-1* mutant, and *enri-2* mutant animals (Figure 6A).
470 Prior to analyzing our data, we sought to better define the expected NRDE-3-bound small
471 RNAs. We initially planned to use two previously defined ERGO-target gene lists: the first list
472 (ERGO - Manage) is defined by small RNAs significantly depleted at least two-fold in *ergo-1*
473 mutant compared to wild-type at the gravid adult stage, with at least 10 reads per million (RPM)

474 in wild-type samples and a DESeq2 adjusted p-value of <0.05 (Manage et al. 2020); the second
475 list (ERGO - Fischer) is defined by genes reduced by 67% in *eri-7* adults or an average of 67% in
476 *ergo-1, eri-1, eri-6,* and *eri-7* embryos, with at least 10 RPM in wild-type (Fischer et al. 2011).
477 However, there is a poor overlap between these two datasets (Figure 6—figure supplement 1D),
478 and small RNAs targeting many of these previously defined ERGO targets were not enriched by
479 NRDE-3 in a published NRDE-3 IP-sRNA seq data on young adult animals that have begun
480 oogenesis but do not yet have embryos (Seroussi et al. 2023) (Figure 6—figure supplement 1A-
481 B). To define a more stringent NRDE-3-target gene list at the young adult stage, we chose genes
482 with at least four-fold enrichment ($\log_2$FC ≥2) and 100 RPM (RPM ≥100) from the NRDE-3 IP-
483 sRNA seq in young adults (Seroussi et al. 2023). This new list contains 119 genes and largely
484 overlaps with the two previously defined ERGO-target gene lists (Figure 6—figure supplement
485 1C-D). To further confirm that this newly defined gene list represents NRDE-3 targets, we
486 analyzed published small RNA and mRNA sequencing data from wild-type and *nrde-3* mutant
487 mixed-stage embryos (before the bean stage) (Padeken et al. 2021). Compared to the Manage
488 and Fischer ERGO-target gene lists, the NRDE-3-target gene list shows more significant small
489 RNA depletion and a greater increase in mRNA expression in the *nrde-3* mutant compared to
490 wild-type (Figure 6—figure supplement 1A-C,E-F). Therefore, we use the new NRDE-3-target
491 gene list to represent the ERGO-1 pathway-dependent, NRDE-3-target genes (referred to here
492 as ERGO targets) in the rest of this study.

493 We next examined the small RNAs bound to NRDE-3 in wild-type early embryos and late
494 embryos, comparing our data to the published NRDE-3 IP-sRNA seq data on young adult animals
495 (Seroussi et al. 2023). Strikingly, we found that in early embryos, the majority of small RNAs
496 bound by NRDE-3 are CSR-class 22G-RNAs, which become progressively less enriched as the
497 animals develop into late embryos and then young adults (Figure 6B-D). In contrast, enrichment
498 for small RNAs targeting ERGO-target genes increases as *C. elegans* develops, and they become
499 the majority of NRDE-3-bound small RNAs by young adulthood (Figure 6B-D). NRDE-3 also binds
500 to CSR-target genes in the early embryos of the *eri-1* mutant, when it is observed to localize to
501 the nucleus, indicating that the production of these NRDE-3-bound CSR-class 22G-RNAs is
502 independent of *eri-1* and that CSR-class 22G-RNAs are likely sufficient to promote nuclear entry
503 of NRDE-3 in the early embryo (Figure 2A, Figure 6—figure supplement 2A). To conclude, NRDE-
504 3 binds to CSR-class 22G-RNA in early embryos but switches to bind preferentially to ERGO-
505 dependent 22G-RNA in late embryos and young adults, suggesting that NRDE-3 may have two
506 separable functions at distinct developmental time points. It is also curious to note that the change
507 in small RNA preference of NRDE-3 coincides with the appearance and disappearance of the

508 cytoplasmic SIMR granules, suggesting a potential role for SIMR-1 and ENRI-2 in promoting the
509 switch of small RNA loading of NRDE-3.
510
511 **SIMR-1 and ENRI-2 contributes to an efficient switch of NRDE-3 bound small RNAs**
512 Since ERGO-dependent 22G-RNA loading was mainly observed in late embryos, we
513 focused on NRDE-3-bound small RNAs in the *eri-1* mutant, *simr-1* mutant, and *enri-2* mutant late
514 embryos to determine the role of SIMR granules in promoting NRDE-3 small RNA binding
515 specificity. We first examined the levels of ERGO-dependent small RNAs in the total small RNA
516 samples and observed depletion of small RNAs mapping to ERGO-target genes in the *eri-1*
517 mutant (Figure 6E, Figure 6—figure supplement 2A). This result is consistent with previous
518 research indicating that ERI-1 is required for ERGO-class 26G RNA production and downstream
519 ERGO-dependent 22G-RNA production (Vasale et al. 2010; Han et al. 2009; Guang et al. 2008).
520 ERGO-dependent small RNAs are not substantially depleted in *simr-1* or *enri-2* mutants,
521 indicating that RRF-1 can still synthesize a similar amount of ERGO-dependent 22G-RNAs when
522 the cytoplasmic SIMR granules are absent (Figure 6E). Following NRDE-3 immunoprecipitation
523 in the *eri-1* mutant, we observed a reduction in NRDE-3 binding to ERGO-dependent small RNAs
524 and an increase binding to CSR-class small RNAs (Figure 6F-G, Figure 6—figure supplement
525 2A). These data indicate that in the absence of ERGO-dependent small RNAs, some NRDE-3
526 protein remains associated with CSR-class small RNAs into late embryogenesis. In the *simr-1*
527 and *enri-2* mutants, although we did not observe a significant reduction of NRDE-3-bound ERGO-
528 dependent small RNAs, we saw a significant increase of CSR-class 22G-RNA binding in the *simr-*
529 *1* mutant and a more modest but still significant increase of CSR-class 22G-RNA binding in the
530 *enri-2* mutant (Figure 6F-G, Figure 6—figure supplement 2B). These results indicate that SIMR-
531 1 and ENRI-2 are not required for the production of the ERGO-dependent small RNAs during
532 embryogenesis, but may be required for an efficient switch from CSR-class to ERGO-dependent
533 22G RNAs.
534
535 **NRDE-3 binds to CSR-class 22G-RNAs but does not silence CSR targets in early embryos**
536 We discovered that NRDE-3 unexpectedly binds to CSR-class 22G-RNAs in early
537 embryos, suggesting a potential new role for NRDE-3 that has not been previously reported. We
538 hypothesized that NRDE-3 may function with CSR-1, perhaps to transcriptionally repress
539 germline-expressed genes in early embryos while CSR-1 utilizes its catalytic activity to clear the
540 same maternally-deposited transcripts (Quarato et al. 2021). To begin to address this hypothesis,
541 we first sought to assess the degree to which NRDE-3-bound 22G-RNAs are similar to CSR-1-

542 bound 22G-RNAs in early embryos. First, we examined the overlap of NRDE-3-targeted genes in
543 early embryos with CSR-1-targeted genes in embryos or young adult animals. We found that the
544 genes targeted by NRDE-3 substantially overlap with CSR-target genes at both stages (Figure
545 7A) (Quarato et al. 2021; Nguyen and Phillips 2021). Furthermore, the CSR-target genes yielding
546 the highest abundance of CSR-1-bound small RNAs in embryos also have the highest abundance
547 of NRDE-3-bound small RNAs (Figure 7B). These CSR-target genes with highly abundant CSR-
548 bound small RNAs are highly enriched by NRDE-3 only in embryos and not in young adults
549 (Figure 7—figure supplement 1A). Next, CSR-class 22G-RNAs tend to be enriched at the 3' ends
550 of mRNAs while WAGO-class 22G-RNAs are more evenly distributed across the gene bodies in
551 adult animals (Ishidate et al. 2018; Singh et al. 2021). Comparing NRDE-3-bound small RNAs
552 from early embryos to a published dataset of CSR-1-bound small RNA from mixed-stage
553 embryos, we found that both NRDE-3 and CSR-1 are heavily enriched for small RNAs derived
554 from the 3' ends of CSR-target genes in embryos (Figure 7C). Interestingly, in adult animals,
555 CSR-1-bound 22G-RNAs are still enriched for small RNA derived from the 3' end of CSR-target
556 genes, however there is additionally a much higher enrichment of small RNAs derived from the
557 gene bodies compared to in embryos (Figure 7C). It has previously been proposed that two types
558 of CSR-class 22G-RNAs exist, those that depend on CSR-1 catalytic activity for their production
559 and are derived primarily from target gene bodies, and those that are produced independently of
560 CSR-1 catalytic activity and are derived primarily from target 3' UTRs (Singh et al. 2021). Our
561 data points to both NRDE-3 and CSR-1 binding only the latter, CSR-1 catalytic activity-
562 independent, type of CSR-class 22G-RNA in early embryos. In contrast, NRDE-3 does not show
563 enrichment for small RNAs derived from the 3' ends of ERGO target genes in embryos, and rather
564 the small RNAs are distributed more evenly across the gene bodies (Figure 7—figure supplement
565 1B). CSR-1 utilizes its catalytic activity to slice and clear maternally-inherited mRNAs from early
566 embryos, preferentially binding to transcripts degraded early in embryogenesis (Quarato et al.
567 2021). We further demonstrate that NRDE-3 similarly binds preferentially to early-degraded
568 transcripts (Figure 7—figure supplement 1C). Lastly, the expression of mRNAs targeted by CSR-
569 1 decreases across embryonic development as CSR-1 actively slices and clears these maternal
570 transcripts (Quarato et al. 2021). We similarly find that the mRNAs targeted by NRDE-3 in young
571 embryos, which correspond primarily to CSR-target mRNAs, decrease in expression across
572 development, while its targets in young adults, corresponding primarily to ERGO-target mRNAs,
573 increase in expression across development (Figure 7—figure supplement 1D). Together, these
574 data reveal that NRDE-3 binds to the same group of small RNAs as CSR-1 in early embryos.

575 To further investigate whether NRDE-3 and CSR-1 function synergistically, we examined
576 the fertility of the *csr-1::degron* strain and the *csr-1::degron*; *gfp::nrde-3(HK-AA)* strain upon auxin
577 treatment to deplete CSR-1. As expected, both strains had 100% viable progeny with ethanol
578 control treatment (Figure 7—figure supplement 1E). When growing on 4mM auxin plates, the
579 number of embryos laid by the *csr-1::degron*; *gfp::nrde-3(HK-AA)* double mutant was significantly
580 lower compared to the *csr-1::degron* single mutant and more of the double mutant produced no
581 embryos (11.9%) compared to the *csr-1::degron* single mutant strain (7.5%), indicating a more
582 severe sterility defect in the *csr-1::degron; nrde-3(HK-AA)* double mutant compared to the *csr-*
583 *1::degron* alone (Figure 7D, Figure 7—figure supplement 1E). Additionally, 5.9% of the auxin-
584 treated *csr-1::degron* animals produced some F1 progeny that hatched, compared to no F1
585 hatching for any of the auxin-treated *csr-1::degron; gfp::nrde-3(HK-AA)* double mutant animals
586 (Figure 7—figure supplement 1E). All together, these results indicate that loss of NRDE-3
587 enhances the fertility defects of CSR-1.
588 NRDE-3 is a nuclear Argonaute protein that recruits histone methyltransferases to target
589 genes to deposit histone modifications such as H3K9me3 and H3K27me3 at these loci (Guang
590 et al. 2008; Burton et al. 2011; Mao et al. 2015). To examine whether NRDE-3 promotes
591 deposition of H3K9me3 at CSR-target genes during embryogenesis, we analyzed the published
592 anti-H3K9me3 ChIP-seq data of wild-type and *nrde-3* mutant mixed-staged embryos (Padeken et
593 al. 2021). In wild-type embryos, the targets of NRDE-3 in young adults, which correspond to
594 ERGO-target genes, have high H3K9me3 levels, and are significantly decreased in the *nrde-3*
595 mutant (Figure 7E). These data are consistent with previous research demonstrating that NRDE-
596 3 deposits H3K9me3 at ERGO target genes (Burton et al. 2011). However, NRDE-3 targets in
597 early embryos do not show H3K9me3 enrichment in wild-type and do not have a significant
598 change in the *nrde-3* mutant (Figure 7E). The same trend is also observed in the early degraded
599 and late degraded targets (Figure 7E). These results indicate that the CSR targets are not H3K9
600 trimethylated in the early embryos. However, we cannot rule out the possibility that NRDE-3 may
601 function to deposit other histone modification targets such as H3K27me3 and H3K23me3 or inhibit
602 RNA Polymerase II (Pol II) on CSR targets to transcriptionally silence these genes in early
603 embryos.
604
605 **NRDE-3 associates with CSR-class 22G-RNAs in oocytes**
606 In addition to being expressed in early embryos, NRDE-3 is also expressed in germ cells,
607 starting in late pachytene through oogenesis (Seroussi et al. 2023; Chen and Phillips 2024b).
608 Because we were unable to detect a change in H3K9me3 in early embryos in the *nrde-3* mutant,

609 we next sought to determine whether NRDE-3 binds to CSR-class 22G-RNAs in germ cells.
610 Curiously, in late embryos from *eri-1* mutant and *rde-3* mutant, we have observed nuclear
611 localization of NRDE-3 only in the primordial germ cells (Figure 2A), raising an intriguing
612 hypothesis that NRDE-3 might bind to CSR-class 22G-RNAs in germ cells throughout
613 development and inherit NRDE-3-bound CSR-class 22G-RNAs to early embryos.

614 To determine whether NRDE-3 also binds to CSR-class 22G-RNAs in oocytes, we first
615 asked whether the nuclear localization of NRDE-3 in the adult germline depends on ERI-1 and
616 RDE-3, key components of the ERI and Mutator complexes, respectively (Figure 1—figure
617 supplement 1A-B). Loss of NRDE-3 nuclear localization in these mutants would indicate that
618 NRDE-3 binds to ERGO-dependent 22G-RNAs in oocytes. Instead, we found that NRDE-3
619 localizes to the nuclei of oocytes in *eri-1* and *rde-3* mutants, similar to wild-type, but is restricted
620 to cytoplasm in the *nrde-3(HK-AA)* small RNA binding mutant (Figure 8A). These data
621 demonstrate that NRDE-3 nuclear localization remains dependent on small RNA binding, but
622 ERGO-dependent 22G-RNAs are not required, consistent with NRDE-3 localization in early
623 embryos. Next, to more directly address whether NRDE-3 binds to CSR-class 22G-RNAs in
624 oocytes, we utilized the auxin-inducible degron (AID) system to deplete the RdRP EGO-1 by
625 growing the worms on 4mM auxin plates starting at the L1 stage (Zhang et al. 2015). Surprisingly,
626 NRDE-3 still localizes to nuclei in both germ cells and early embryos upon EGO-1 depletion
627 (Figure 8B), indicating that NRDE-3 either does not exclusively bind CSR-class 22G-RNAs in the
628 germline, or NRDE-3 has the capacity to bind other small RNAs when the CSR-class 22G-RNAs
629 are absent. We did observe some cytoplasmic NRDE-3 granules in a subset of 8-cell stage
630 embryos following EGO-1 depletion (Figure 8B), suggesting that a proportion of NRDE-3 might
631 be unloaded. To further probe which small RNAs NRDE-3 binds to in the germline, we introduced
632 a *rde-3* mutation into the GFP::NRDE-3; degron::EGO-1 strain to deplete all WAGO-class 22G-
633 RNAs, with include the ERGO-dependent 22G-RNAs, along with the CSR-class 22G-RNAs. We
634 observed that NRDE-3 no longer localizes to the nucleus in both germline and early embryos in
635 the absence of both WAGO-class and CSR-class 22G-RNAs (Figure 8B). These results, in
636 combination with our sequencing data, indicate that NRDE-3 likely binds CSR-class 22G-RNAs
637 in the germline and early embryos but has the capacity to additionally bind WAGO-class 22G-
638 RNAs when CSR-class 22G-RNAs are depleted. Furthermore, because somatic transcription is
639 not initiated in early embryos until the 4-cell stage (Seydoux and Fire 1994), we conclude that the
640 NRDE-3 is loaded with CSR-class 22G-RNAs in the parental germline and then transmitted to
641 early embryos.
642

643 **NRDE-3 represses RNA Pol II and promotes global transcriptional repression in oocytes**

644 Oocytes undergo global transcriptional repression across diverse species (Woodland
645 1987). In *C. elegans*, transcriptional shutdown begins during the diakinesis stage of late oocytes
646 to prepare for fertilization, and reactivates at the 4-cell stage embryos to initiate zygotic
647 transcription (Walker et al. 2007). Previous work has shown that topoisomerase II acting with the
648 condensin II complex, H3K9me3, and the zinc-finger containing protein PIE-1 are critical for global
649 transcriptional repression (Belew et al. 2023), but the complete molecular mechanisms underlying
650 the oocyte-to-embryo transition remain not fully understood. We therefore aimed to address
651 whether germline-expressed NRDE-3 could play a role in these pathways.

652 Our hypothesis that NRDE-3 may mediate transcriptional repression in oocytes is
653 supported by several lines of evidence. First, NRDE-3 is expressed at the correct place and time—
654 in the germline, from late pachytene to diakinetic oocytes (Seroussi et al. 2023)—and is known to
655 co-transcriptionally silencing genes by depositing H3K9me3 and inhibiting Pol II transcription
656 (Guang et al. 2008). Second, the slicing activity of CSR-1 is required to inhibit Pol II-dependent
657 transcription in maturing oocytes (Fassnacht et al. 2018). CSR-1 is not known to directly inhibit
658 transcription, but it is required for the production of at least a subset of the CSR-class 22G-RNAs
659 (Singh et al. 2021); therefore, the CSR-1-dependent Pol II inhibition could be mediated by NRDE-
660 3-bound CSR-class 22G-RNAs. Third, H3K9me3 and the H3K9me3 methyltransferase SET-25
661 are required for transcription repression in oocytes (Belew et al. 2023). NRDE-3 can act to recruit
662 SET-25 and establish H3K9me3-containing heterochromatin (Padeken et al. 2021), making it a
663 strong candidate for initiating H3K9me3-dependent transcriptional silencing in oocytes.

664 The above evidence connects Pol II repression in oocytes to the co-transcriptional
665 silencing function of NRDE-3 and the requirement for CSR-class 22G-RNAs in oocytes.
666 Phosphorylation of RNA Polymerase II (Pol II) on its large subunit C-terminal domain (CTD)
667 serves as a well-studied marker of transcription activity, with Ser5 phosphorylation indicating
668 transcription initiation and Ser2 phosphorylation marks elongation. Therefore, to monitor Pol II
669 activity in oocytes, we stained wild-type and *nrde-3(HK-AA)* mutant gonads using an antibody
670 specific for phosphorylated serine 2 (PSer2) on the Pol II C-terminal domain (CTD), a marker for
671 transcription elongation (Belew et al. 2023; Seydoux and Dunn 1997). Consistent with previously
672 reports, PSer2 staining in the most proximal oocytes exhibited distinct patterns of localization: (1)
673 PSer2 excluded from DNA ('excluded from DNA'), (2) PSer2 present both on and off DNA
674 ('diffuse'), and (3) PSer2 enriched on DNA ('enriched on DNA'). The PSer2 signal intensity and
675 the localization pattern serve as indicators of active transcription levels (Belew et al. 2023).
676 Quantification the PSer2 signal intensity shows a significant increase in PSer2 in the *nrde-3(HK-*

677 *AA)* mutant across all oocytes (from -1 to -7), indicating a global increase in transcription
678 elongation in the *nrde-3(HK-AA)* mutant (Figure 8C). Furthermore, by quantifying the PSer2
679 localization patterns, we found that elongating RNA Pol II stays associated with DNA longer in
680 the *nrde-3(HK-AA)* mutant, compared to wild-type. This data is consistent with what has been
681 observed previously in the *set-25* mutant (Belew et al. 2023) (Figure 8D-E). Therefore, we
682 conclude that NRDE-3 contributes to global transcriptional repression in oocytes by repressing
683 RNA Pol II.
684

685 **Discussion**

686 Germ granules are phase-separated condensates that localize to the perinuclear region
687 of germ cells. In *C. elegans*, the known constituents of the germ granule have expanded over the
688 last decades, such that germ granules now comprise multiple domains including P granules,
689 *Mutator* foci, Z granules, SIMR foci, E granules, and D granules. Here we discovered that several
690 components of SIMR foci and *Mutator* foci also localize to cytoplasmic granules during specific
691 stages of embryogenesis, where their temporal expression is regulated by autophagic
692 degradation. We propose that these granules may serve as sites for the synthesis and loading of
693 22G-RNAs into the nuclear Argonaute NRDE-3. Furthermore, we showed that NRDE-3 switches
694 its small RNA targets during embryogenesis, coincident with the formation of SIMR granules;
695 during oogenesis, NRDE-3 binds to CSR-class 22G-RNAs to promote global transcriptional
696 repression prior to the oocyte-to-embryo transition, and then in the developing soma, NRDE-3
697 binds to ERGO-dependent 22G-RNAs to silence retrotransposons and recently duplicated genes.
698 Together, our study reveals a new world of embryonic RNAi factor condensates and uncovers
699 two temporally distinct roles for NRDE-3, underscoring the need for careful examination of
700 localization and targets of RNAi pathways across development (Figure 9).
701

702 **A role for SIMR-1 as a platform for nuclear Argonaute protein loading**

703 Previously we demonstrated that SIMR-1 and HRDE-2 are required to recruit unloaded
704 HRDE-1, the germline nuclear Argonaute protein, to germ granules and to ensure correct 22G-
705 RNA loading (Chen and Phillips 2024a). Here we reveal that SIMR-1 and another HRDE-2
706 paralog, ENRI-2, are similarly essential to recruit unloaded NRDE-3, the somatic nuclear
707 Argonaute protein, to embryonic SIMR granules. We speculate that SIMR-1 and ENRI-2 are
708 similarly important for NRDE-3 22G-RNA loading; however, we did not observe a significant
709 change in the ERGO-dependent 22G-RNAs loaded by NRDE-3 in *simr-1* or *enri-2* mutant
710 embryos compared to wild-type. While initially surprising based on the results of similar

experiments with HRDE-1 in the germline, we envision several possible explanations. First, it is possible that SIMR-1 and ENRI-2 act to bring unloaded NRDE-3 in close proximity to the ERGO-dependent 22G-RNA biogenesis machinery, but that NRDE-3 loading can still occur diffusely in the cytoplasm, albeit with lower efficiency. Both the RdRP RRF-1 and unloaded NRDE-3 diffusely localize to cytoplasm in the *simr-1* mutant (Figure 3A, 4D), suggesting that NRDE-3 may load the ERGO-class small RNAs synthesized in the cytoplasm in the absence of SIMR-1. Differences in NRDE-3 loading efficiency would likely not be detected by our NRDE-3 IP-small RNA sequencing experiment. Second, SIMR-1 and ENRI-2 could act to sequester unloaded NRDE-3 away from other small RNAs (i.e. CSR-class 22G-RNAs) to prevent misloading. Misloading should be detectable in our NRDE-3 IP-small RNA sequencing experiment and we do see a modest increase in CSR-class 22G-RNAs loaded by NRDE-3 in late embryos; however, it is unclear the extent to which newly synthesized, and unloaded CSR-class 22G-RNAs are even present in the cytoplasm, as the primary source for CSR-class 22G-RNAs may be the maternal germline. Thus, unlike in the adult germline where HRDE-1 incorrectly loads CSR-class 22G-RNAs in the absence of HRDE-2, there may not be an equivalent source of incorrect small RNAs that NRDE-3 can bind to (i.e. correct length, 5' nucleotide and modifications) in the embryo. To further probe these possibilities, we need to more carefully assess the dynamics of NRDE-3 loading across embryonic development and possibly disrupt the formation of embryonic CSR granules to determine whether compartmentalization of the CSR-class 22G-RNA pathway is also contributing to correct loading of NRDE-3 in the absence of SIMR-1 and ENRI-2.

We do not know the precise functions of SIMR-1 and ENRI-2, however we have previously proposed that SIMR-1 mediates protein-protein interactions through its extended Tudor domain (Manage et al. 2020). ENRI-2 and its paralog HRDE-2 have structural similarities to a HELICc domain, and SIMR-1, ENRI-2, and HRDE-2 have large unstructured domains (Figure 9—figure supplement 1A) (Lewis et al. 2020; Chen and Phillips 2024a). With the advent of protein complex prediction algorithms (Abramson et al. 2024), we sought to examine the potential physical interactions between ENRI-2 and NRDE-3, as well as their paralogs HRDE-2 and HRDE-1. In both models, the structured HELICc domain of HRDE-2 and ENRI-2 dock on the Mid domain of their respective Argonaute partners. Interestingly, the unstructured C-terminal domains of ENRI-2 and HRDE-2 extend into the small RNA binding pocket of their respective nuclear Argonaute binding partners (Figure 9—figure supplement 1B). At this point, we do not know whether these structures are reflective of the actual geometry of the proteins *in vivo*, but it is tempting to speculate that the C-terminal disordered regions of the ENRI-2/HRDE-2 proteins could regulate 22G-RNA loading through interaction with the small RNA binding pocket of NRDE-3 and HRDE-

745 1. Further study will be necessary to determine whether these interactions between disordered
746 regions and the small RNA binding pocket are necessary for correct small RNA loading and
747 whether that mechanism extends to other WAGO proteins.
748
749 **Compartmentalization of RNAi pathways**
750 Most of the studies on the organization of *C. elegans* RNAi factors in granules focus on
751 the germline. Here we find that multiple proteins associated with 22G-RNA biogenesis and
752 function, including SIMR-1, RDE-3, RRF-1, ENRI-2, and unloaded NRDE-3, are localized to
753 distinct condensates in *C. elegans* embryos. We speculate that these SIMR granules, which
754 appear and then disappear during the course of embryonic development, play a functional role in
755 the NRDE-3 nuclear RNAi pathway. This idea leads to an intriguing question: what role does
756 organization of the RNAi pathways into condensates play in the soma vs. in the germline?
757 In germ cells, RNAi factors are visibly segregated into distinct compartments within the
758 germ granule which assemble hierarchically (Uebel et al. 2023). Germ granules are also intimately
759 linked to nuclear pores, leading to a model where highly concentrated mRNAs, newly exported
760 from and adjacent to the nuclear pore, nucleate assembly of regulatory factors into visible
761 granules. In fact, nuclear pores are clustered beneath germ granules in germ cells, and evidence
762 suggests that most, if not all, nascent mRNAs are exported through pores associated with germ
763 granules (Pitt et al. 2000; Sheth et al. 2010). In contrast, nuclear pores are distributed more evenly
764 across the nuclear periphery in embryos and, in this work, we find that while some embryonic
765 SIMR granules appear adjacent to the nuclear periphery, many are distributed in the cytoplasm
766 (see Figure 2A, for example). Thus, unlike in germ granules, there is no obvious trajectory from
767 the nucleus that RNAs would follow to end up in embryonic SIMR granules. Further, in the
768 germline, we have speculated that the adjacent and hierarchical assembly of germ granule
769 compartments could be determined by the order of molecular events required for RNA silencing
770 (Uebel et al. 2023). While we on occasion see docking between embryonic SIMR granules and
771 CSR granules (Figure 4I), we do not see any more complex arrangement of granule
772 compartments in embryos similar to what we have observed in the germline. What that means
773 regarding the functionality of embryonic SIMR granules is unclear. Another possibility worth
774 considering is that SIMR granules are not actually required for ERGO-dependent 22G-RNA
775 biogenesis and NRDE-3 loading in embryos but rather that they reflect a concentration of the
776 small RNA biogenesis machinery beyond the solubility limit of the cytoplasm, resulting in the
777 demixing of some RNP complexes into visible SIMR granules (Putnam et al. 2023). By this

778 “incidental condensate” model, ERGO-dependent 22G-RNA biogenesis and NRDE-3 loading
779 occur just as efficiently, or perhaps more so, diffusely in the cytoplasm.
780 Both embryonic and germ granules exhibit dynamic expression patterns, suggesting that
781 expression and function of small RNA factors are critical at discrete developmental time points.
782 In the germline, multiple Argonaute proteins are expressed exclusively during oogenesis (ERGO-
783 1) or spermatogenesis (ALG-3, ALG-4, CSR-1b, WAGO-10) (Billi et al. 2012; Han et al. 2009;
784 Conine et al. 2010; Reinke et al. 2004; Nguyen and Phillips 2021; Charlesworth et al. 2021) and
785 MUT-16 expression fluctuates across germ cell development, peaking in the mitotic region (Uebel
786 et al. 2020). Similarly, embryonic SIMR granules appear in early embryos and disappear by late
787 embryogenesis. Regardless as to whether SIMR granules are incidental condensates or
788 functional sites for NRDE-3 loading, these data indicate that the levels or activities of these
789 proteins are developmentally regulated.
790 It is additionally curious that embryonic and germ granules share many protein
791 components yet possess distinct differences in content and assembly requirements. For instance,
792 several RNAi proteins, such as RRF-1 and RDE-3, are shared between *Mutator* foci and
793 embryonic SIMR granules, while the paralogous ENRI-2/NRDE-3 and HRDE-2/HRDE-1 pairs are
794 found in embryonic SIMR granules and germline SIMR foci, respectively. It is unclear why the
795 *Mutator* and SIMR components are visible as separate compartments in germ granules but are
796 together in embryonic SIMR foci. This difference is highlighted by the requirement for MUT-16 in
797 the assembly of embryonic SIMR granules but not germline SIMR foci (Figure 4E) (Manage et al.
798 2020). Further investigation into the assembly and protein components of embryonic and germ
799 granules will be crucial for elucidating the functional differences between embryonic and germ
800 granules and dissecting the mechanisms of 22G-RNA loading into NRDE-3.
801
802 **Spatial-temporal regulation of SIMR and other embryonic granules by autophagy**
803 Autophagy is a conserved eukaryotic protein degradation pathway involving the formation
804 of double-membrane autophagosomes, which fuse with lysosomes for degradation (Nakatogawa
805 et al. 2009). Autophagy has been linked to small RNA pathways and germ granules in *C. elegans*
806 and other organisms. In *Arabidopsis*, the turnover of Argonaute protein AGO1 is controlled by
807 autophagy in both antiviral and nonviral contexts (Derrien et al. 2012). In mammalian cells, AGO2
808 and Dicer are targeted for degradation via autophagy (Gibbings et al. 2012). In *C. elegans*, P
809 granule components PGL-1 and PGL-3 are recruited to somatic aggregates during
810 embryogenesis and degraded by autophagy (Zhang et al. 2009). Interestingly, miRNA pathway

811 components ALG-1, ALG-2 and their interactor AIN-1/GW182 are also degraded by autophagy,
812 while in aggregates distinct from PGL somatic aggregates (Zhang and Zhang 2013).
813 Here, we discovered that, similar to P granule components, the expression of many other
814 granule-associated proteins in *C. elegans*, including the core Z granule protein ZNFX-1, the D
815 granule protein CSR-1, and the SIMR granule protein SIMR-1, are also controlled by autophagy
816 during embryogenesis. It is worth noting that the timing of degradation differs amongst the
817 different granules, with P granules and Z granules being cleared from somatic cells within the first
818 few cell divisions of the developing embryo (Strome and Wood 1983; Wan et al. 2018), while CSR
819 granules are removed between 28- and 100-cell stage (Figure 4G), and SIMR granules disappear
820 between 100- and 200-cell stage of embryonic development (Figure 1C,2C). These results
821 suggest an intriguing hypothesis that different granules might be produced independently at
822 designated developmental stages and cytosolic locations to perform specific functions, and later
823 actively degraded by autophagy when not needed. Future studies will be needed to carefully
824 examine the role and fate of each type of granule during embryogenesis to test this hypothesis.
825 Lastly, while autophagy pathway plays an important role in regulating expression of many
826 granule components, we cannot role the possibility that the ubiquitin-proteasome system may
827 also contribute to protein turnover in the small RNA pathway. In fact, Zhang et al demonstrated
828 that, unlike PGL-1 and PGL-3, the other P granule components GLH-1 and GLH-4 are not
829 degraded via autophagy (Zhang et al. 2009). Additionally, DeRenzo et al showed that germline-
830 expressed CCCH figure proteins, including PIE-1, POS-1, MEX-1, are selectively targeted for
831 degradation in somatic cells by the E3 ubiquitin ligase subunit-interacting protein ZIF-1 through
832 the ubiquitin-proteasome system (DeRenzo et al. 2003). Furthermore, previous research suggest
833 that the proteosome and autophagy pathways can act as compensatory mechanisms under
834 certain contexts (Ji and Kwon 2017). Future studies will be needed to interrogate the roles of
835 these two protein degradation pathways in regulating protein turnover in the small RNA pathway.
836

837 **The small RNA plasticity of NRDE-3**

838 Argonautes are conventionally known to bind small RNAs with high specificity. In this
839 study, we unveil the remarkable versatility of the nuclear Argonaute NRDE-3, demonstrating its
840 ability to bind multiple classes of small RNAs and exhibit distinct functions throughout
841 development. Argonaute proteins with the capacity to bind multiple types or classes of small RNAs
842 have been observed in other organisms. For example, both siRNAs and miRNAs can be loaded
843 into the four human Argonautes (Ago1-4) and both siRNAs and miRNAs can guide Ago2-
844 dependent target cleavage (Meister et al. 2004; Liu et al. 2004). Our discovery is somewhat

845 different, however, in that NRDE-3 binds its two preferred classes of small RNAs, CSR-class 22G-
846 RNAs and ERGO-dependent 22G-RNAs, at distinct developmental stages, indicating that there
847 must be a switch from one class of small RNA to the other during embryogenesis. Interestingly,
848 a more recent study in the parasitic nematode *Ascaris* revealed that the *Ascaris* paralog of NRDE-
849 3, AsNRDE-3, exhibits a dramatic change in associated small RNAs during spermatogenesis,
850 targeting repetitive sequences and transposons in early stages of spermatogenesis and mRNAs
851 in late meiosis (Zagoskin et al. 2022). Curiously, the mRNAs targeted by AsNRDE-3 in late
852 meiosis largely overlap with the targets of AsCSR-1, the *Ascaris* paralog of CSR-1, and it is
853 proposed that AsNRDE-3 could act in concert with AsCSR-1 at the late stages of meiosis to clear
854 spermatogenic and meiotic mRNAs from the developing spermatids (Zagoskin et al. 2022). These
855 data further suggest that the ability of NRDE-3 to target both repetitive sequences and germline-
856 expressed genes at distinct developmental timepoints may be a conserved feature of this protein.
857 It is currently unknown how this small RNA switching is achieved. It is possible that there is an
858 active mechanism to unload the CSR-class 22G-RNAs and replace them with ERGO-dependent
859 22G-RNAs, or to degrade NRDE-3 loaded with CSR-class 22G-RNAs. However, we prefer the
860 simpler model where NRDE-3 loaded with CSR-class 22G-RNAs, initially deposited into embryo
861 from the maternal germline, are diluted out as the animal develops. Newly synthesized NRDE-3
862 in the embryo is loaded with ERGO-dependent 22G-RNAs to execute the small RNA "switch".
863 The idea that Argonaute proteins can be utilized at distinct timepoints with different small RNA
864 partners to create multi-functionality is intriguing, especially in the vein of rapidly clearing
865 transcripts from a cell to engineer a new developmental program. Achieving higher resolution
866 small RNA-Argonaute interactions with tissue- and developmental-specific staging will be crucial
867 to fully elucidate the roles of Argonaute proteins during development in *C. elegans* and other
868 organisms.

869 In summary, this work investigating the role of SIMR granules in embryos, together with
870 our previous study of SIMR foci in the germline (Chen and Phillips 2024a), has identified a new
871 mechanism for regulating nuclear Argonaute protein localization in *C. elegans*. The two
872 paralogous proteins, HRDE-2 and ENRI-2, recruit unloaded nuclear Argonautes HRDE-1 and
873 NRDE-3 to small RNA production centers organized by SIMR-1, where we speculate that loading
874 can occur. These small RNA loading sites are essential in the germline to promote small RNA
875 binding specificity, however they may also contribute to efficiency and specificity of small RNA
876 loading in embryos. We further discovered an intriguing repository of cytoplasmic granules during
877 embryogenesis that do not exhibit the same organization or hierarchical assembly as germ
878 granules, but share the same autophagy-mediated degradation as one another. These results

879 highlight the importance of further investigation into the relationship between RNA silencing
880 pathways and RNA granules during embryogenesis. Lastly, we observed a striking phenomenon
881 where the NRDE-3 nuclear Argonaute protein possesses the ability to switch small RNA binding
882 partners, altering mRNA targets and function during development. Together, these findings reveal
883 that the precise regulation of small RNA pathway components through diverse mechanisms, such
884 as spatial-temporal separation and hierarchical physical interactions, is crucial for accurate gene
885 regulation and developmental transitions in *C. elegans*.
886

887 **Materials and methods**

888 ***C. elegans* stains**

889 *C. elegans* strains were maintained at 20°C on NGM plates seeded with OP50 *E. coli*
890 according to standard conditions unless otherwise stated (Brenner 1974). All strains used in this
891 project are listed in Supplementary File 1.
892

893 **CRISPR-mediated strain construction**

894 For *nrde-3(cmp324[HK-AA])*, *enri-1(cmp328)*, *enri-2(cmp318)*, and *rde-3/mut-2(cmp337)*,
895 we used an oligo repair template and RNA guide. For *enri-1(cmp320[enri-1::mCherry::2xHA])*, we
896 used an RNA guide and PCR amplified repair template (Supplementary File 2). For injections
897 using a single gene-specific crRNA, the injection mix included 0.25 µg/µl Cas9 protein (IDT),
898 100 ng/µl tracrRNA (IDT), 14 ng/µl dpy-10 crRNA, 42 ng/µl gene-specific crRNA, and 110 ng/µl of
899 the oligo repair template. For injections using two gene-specific crRNAs, the injection mix included
900 0.25 µg/µl Cas9 protein (IDT), 100 ng/µl tracrRNA (IDT), 14 ng/µl dpy-10 crRNA, 21 ng/µl each
901 gene-specific crRNA, and 110 ng/µl of each repair template.

902 The following strains were used for injection: *enri-2(cmp318)* and *enri-1(cmp320[enri-*
903 *1::mCherry::2xHA])* into wild-type N2 strain. *nrde-3(cmp324[HK-AA]) and enri-1(cmp328)* into
904 JMC237: *nrde-3(tor131[GFP::3xFLAG::nrde-3]) X*. *rde-3*/*mut-2(cmp337)* into USC1615*: ego-*
905 *1(cmp317[ego-1::degron]) I; ieSi38 [Psun-1::TIR1::mRuby::sun-1 3' UTR] IV; nrde-*
906 *3(tor131[GFP::3xFLAG::nrde-3]) X*. Following injection, F1 animals with the Rol phenotype were
907 isolated and genotyped by PCR to identify heterozygous animals with the mutations of interest,
908 then F2 animals were further singled out to identify homozygous mutant animals.
909

910 **RNAi assays**

911 For RNAi experiment, control L4440 and *lgg-1* RNAi *E. coli* clones were sequenced
912 verified and cultured at 37°C for 16 hours, then RNAi bacteria were seeded on fresh RNAi plates.

913 Two L4 animals were transferred to seeded RNAi plates and raised at 20°C. When the progenies
914 of the L4 animals turn into young adults (about 4 days), the embryos of young adult animals were
915 imaged to assess somatic granule expression.
916
917 **Immunofluorescence imaging and quantification**
918 For immunofluorescence, *C. elegans* were dissected in egg buffer containing 0.1%
919 Tween-20 and fixed in 1% formaldehyde in egg buffer as described (Phillips et al. 2009). Samples
920 were immunostained with anti-RNA Polymerase II CTD (phosphoSer2) at 1:500 (Abcam ab5095).
921 The secondary antibody, anti-Rabbit IgG AlexaFluor 555 was used at 1:1000 (Thermo Fisher
922 A21429). Animals were dissected at the adult stage (24 h post L4). Imaging was performed on a
923 DeltaVision Elite microscope (GE Healthcare) using a 60x N.A. 1.42 oil-immersion objective, data
924 stacks were collected and deconvolution was performed using the SoftWoRx package. 25 optical
925 sections, for a total 12.5μm sample thickness, are presented as a maximum intensity projection.
926 PSer2 signal intensity was calculated in ImageJ (version 1.53a) using a minimum of 10 individual
927 adult gonads.
928
929 **Live imaging**
930 Live imaging of *C. elegans* embryos was performed in M9 buffer. Young embryos were
931 obtained by dissecting gravid adult *C. elegans*, and old embryos were obtained by manually
932 picking embryos laid on the NGM plate. Live imaging of *C. elegans* adult germline was performed
933 in M9 buffer containing sodium azide to prevent movement. Day-one-adult *C. elegans* were
934 obtained by manually picking L4s and leaving L4s at 20°C for about 24 hours. Imaging was
935 performed on a DeltaVision Elite microscope (GE Healthcare) using a 60x N.A. 1.42 oil-immersion
936 objective. Images were pseudocolored using Adobe Photoshop.
937
938 **Granule number quantification**
939 Granule number quantification was performed in FIJI/ImageJ2 (version 2.9.0). At least 10
940 embryos were imaged on a DeltaVision Elite microscope with 37 optical sections of a total
941 22.20μm sample thickness from the bottom of the sample. Images were deconvolved to eliminate
942 backgrounds. Z stacks were opened using the 3D object counter plugin for FIJI, and the granule
943 counting threshold for each image was manually adjusted to obtain the least background and
944 most granules.
945
946 **Colocalization analysis**

947 Quantitative colocalization analysis between different granules was performed in
948 FIJI/ImageJ2 (version 2.9.0) using the Coloc2 package and 100-cell staged embryos imaged on
949 a DeltaVision Elite microscope. At least 3 granules from each embryo, and at least 4 individual
950 embryos for a total of at least 20 granules were used to calculate Pearson's R value.
951
952 **Western blot**
953 Synchronized adult *C. elegans* were harvested (~72 h at 20 °C after L1 arrest) and 200
954 adults were loaded per lane. Proteins were resolved on 4–12% Bis-Tris polyacrylamide gels
955 (Thermo Fisher, NW04122BOX), transferred to nitrocellulose membranes (Thermo Fisher,
956 LC2001), and probed with rat anti-HA-peroxidase 1:1000 (Roche 12013819001), mouse anti-
957 FLAG 1:1000 (Sigma, F1804), or mouse anti-actin 1:10,000 (Abcam ab3280). Secondary HRP
958 antibodies were purchased from Thermo Fisher. Unedited western blots are provided in the
959 Source Data File.
960
961 **Small RNA library preparation and sequencing**
962 For *C. elegans* embryo staging and collection, synchronized arrested L1s were grown on
963 enriched peptone plates at 17°C until the young adult stage. Adult *C. elegans* stage was
964 monitored carefully under DeltaVision microscope by live imaging. For early embryo collection
965 (<=100-cell), adult animals were washed off from plates with H_2O and bleached as soon as the
966 first animals had 1-4 eggs (around 68-70 hours depending on the strain and the incubator
967 temperature). For late embryo collection (>=300-cell), adult animals were washed off from plates
968 with H_2O and bleached when about half of the worms had 1~6 eggs (~70-72 hours depending on
969 the strain and the incubator temperature). After bleaching, embryos were washed twice with M9
970 buffer, and filtered through 40µm cell strainers (Fisherbrand™ Sterile Cell Strainers, 40µm) twice
971 to clear the residual worm body. To reach >=300-cell stage for late embryo collection, embryos
972 were additionally incubated in M9 buffer at 20°C for 4.5 hours. Then embryos were washed once
973 with IP buffer (50 mM Tris-Cl pH 7.5, 100 mM KCl, 2.5 mM MgCl2, 0.1% Nonidet P40 substitute)
974 containing Protease Inhibitor (Thermo Fisher A32965). Embryos were kept on ice during washes
975 to prevent further development. 500,000 embryos were collected for each replicate. Following
976 washes, embryos were flash-frozen by placing tubes in a container with ethanol and dry ice. A
977 small aliquot of embryos was examined on the Deltavision microscope to confirm the
978 developmental stage immediately before freezing. Frozen embryos were stored at -80°C until
979 immunoprecipitation.

For immunoprecipitation followed by small RNA sequencing in embryos, ~500,000 synchronized embryos were sonicated with Fisher Sonifier 550 with a microtip (15s on, 45s off, 10% power, total 2 minutes on time). After sonication, insoluble particulate was removed by centrifugation at 21,000g for 30 minutes. Immunoprecipitation was performed using anti-FLAG Affinity Matrix (Sigma Aldrich, A2220). NRDE-3-bound RNAs were isolated using TRIzol reagent (Thermo Fisher, 15596018), followed by chloroform extraction and isopropanol precipitation. Small RNAs (18 to 30-nt) were size selected on homemade 10% Urea-polyacrylamide gels from total RNA samples. Small RNAs were treated with 5' RNA polyphosphatase (Epicenter RP8092H) and ligated to 3' pre-adenylated adapters with Truncated T4 RNA ligase (NEB M0373L). Small RNAs were then hybridized to the reverse transcription primer, ligated to the 5' adapter with T4 RNA ligase (NEB M0204L), and reverse transcribed with Superscript III (Thermo Fisher 18080-051). Small RNA libraries were amplified using Q5 High-Fidelity DNA polymerase (NEB M0491L) and size selected on a homemade 10% polyacrylamide gel. Library concentration was determined using the Qubit 1X dsDNA HS Assay kit (Thermo Fisher Q33231) and quality was assessed using the Agilent BioAnalyzer. Libraries were sequenced on the Illumina NextSeq2000 (SE 75-bp reads) platform. Primer sequences are available in Supplementary File 2. Differentially expressed gene lists and gene lists used in this paper can be found in Supplementary File 3. Sequencing library statistics summary can be found in Supplementary File 4.

Bioinformatic analysis

For small RNA libraries, sequences were parsed from adapters and quality filtered using FASTX-Toolkit (version 0.0.13) (Greg Hannon 2010). Filtered reads were mapped to the *C. elegans* genome, WS258, using Bowtie2 (version 2.5.0) (Langmead and Salzberg 2012). Mapped reads were assigned to genomic features using featureCounts which is part of the Subread package (version 2.0.1) (Liao et al. 2014). Differential expression analysis was performed using edgeR (3.40.2) (Robinson et al. 2010). To define gene lists from IP experiments, a twofold-change cutoff, an edgeR adjusted p-value of ≤0.05, and at least 10 RPM in the IP libraries were required to identify genes with significant changes in small RNA levels.

Data Availability

The RNA sequencing data generated in this study are available through Gene Expression Omnibus (GEO) under accession code GSE273239. Source data file is provided with this paper.

Acknowledgements

We thank the members of the Phillips lab for helpful discussions and feedback on the manuscript, the labs of Julie Claycomb, John Kim, Heng-Chi Lee, and Mihail Sarov for generously providing strains, and the lab of Matt Michael for sharing the PSer2 antibody and advising on conditions for staining and quantification. This work was supported by the National Institute of Health grant R35 GM119656 (to CMP). Some strains were provided by the CGC, which is funded by NIH Office of Research Infrastructure Programs (P40 OD010440). Next generation sequencing was performed by the USC Molecular Genomics Core, which is supported by award number P30 CA014089 from the National Cancer Institute.

Author contributions

S.C.: Conceptualization, Investigation, Formal analysis, Writing–original draft, Writing–reviewing and editing, Visualization

C.M.P.: Conceptualization, Formal Analysis, Writing–original draft, Writing–reviewing and editing, Supervision, Funding Acquisition.

Competing interests

The authors declare no competing interests.

Reference

Abramson J, Adler J, Dunger J, Evans R, Green T, Pritzel A, Ronneberger O, Willmore L, Ballard AJ, Bambrick J, et al. 2024. Accurate structure prediction of biomolecular interactions with AlphaFold 3. *Nature* **630**: 493–500.

Aoki K, Moriguchi H, Yoshioka T, Okawa K, Tabara H. 2007. In vitro analyses of the production and activity of secondary small interfering RNAs in C. elegans. *EMBO J* **26**: 5007–5019.

Ashe A, Bélicard T, Le Pen J, Sarkies P, Frézal L, Lehrbach NJ, Félix M-A, Miska EA. 2013. A deletion polymorphism in the Caenorhabditis elegans RIG-I homolog disables viral RNA dicing and antiviral immunity ed. D. Weigel. *eLife* **2**: e00994.

Belew MD, Chien E, Michael WM. 2023. Characterization of factors that underlie transcriptional silencing in C. elegans oocytes. *PLOS Genet* **19**: e1010831.

Billi AC, Alessi AF, Khivansara V, Han T, Freeberg M, Mitani S, Kim JK. 2012. The Caenorhabditis elegans HEN1 Ortholog, HENN-1, Methylates and Stabilizes Select Subclasses of Germline Small RNAs. *PLOS Genet* **8**: e1002617.

Brangwynne CP, Eckmann CR, Courson DS, Rybarska A, Hoege C, Gharakhani J, Jülicher F, Hyman AA. 2009. Germline P Granules Are Liquid Droplets That Localize by Controlled Dissolution/Condensation. *Science* **324**: 1729–1732.

Brenner S. 1974. THE GENETICS OF CAENORHABDITIS ELEGANS. *Genetics* **77**: 71–94.

1050 Buck AH, Blaxter M. 2013. Functional diversification of Argonautes in nematodes: an expanding
1051 universe. *Biochem Soc Trans* **41**: 881–886.

1052 Buckley BA, Burkhart KB, Gu SG, Spracklin G, Kershner A, Fritz H, Kimble J, Fire A, Kennedy
1053 S. 2012. A nuclear Argonaute promotes multigenerational epigenetic inheritance and
1054 germline immortality. *Nature* **489**: 447–451.

1055 Burton NO, Burkhart KB, Kennedy S. 2011. Nuclear RNAi maintains heritable gene silencing in
1056 Caenorhabditis elegans. *Proc Natl Acad Sci* **108**: 19683–19688.

1057 Charlesworth AG, Seroussi U, Lehrbach NJ, Renaud MS, Sundby AE, Molnar RI, Lao RX, Willis
1058 AR, Woock JR, Aber MJ, et al. 2021. Two isoforms of the essential C. elegans
1059 Argonaute CSR-1 differentially regulate sperm and oocyte fertility. *Nucleic Acids Res* **49**:
1060 8836–8865.

1061 Chen C-CG, Simard MJ, Tabara H, Brownell DR, McCollough JA, Mello CC. 2005. A Member of
1062 the Polymerase β Nucleotidyltransferase Superfamily Is Required for RNA Interference
1063 in C. elegans. *Curr Biol* **15**: 378–383.

1064 Chen S, Phillips CM. 2024a. HRDE-2 drives small RNA specificity for the nuclear Argonaute
1065 protein HRDE-1. *Nat Commun* **15**: 957.

1066 Chen S, Phillips CM. 2024b. Silencing of a NRDE-3 transgene in C. elegans germ cells and
1067 early embryos is mediated by the RNAi pathway. *MicroPublication Biol*.
1068 https://www.micropublication.org/journals/biology/micropub-biology-001308 (Accessed
1069 December 25, 2024).

1070 Chen X, Wang K, Mufti FUD, Xu D, Zhu C, Huang X, Zeng C, Jin Q, Huang X, Yan Y, et al.
1071 2024. Germ granule compartments coordinate specialized small RNA production. *Nat*
1072 *Commun* **15**: 5799.

1073 Claycomb JM, Batista PJ, Pang KM, Gu W, Vasale JJ, Wolfswinkel JC van, Chaves DA,
1074 Shirayama M, Mitani S, Ketting RF, et al. 2009. The Argonaute CSR-1 and Its 22G-RNA
1075 Cofactors Are Required for Holocentric Chromosome Segregation. *Cell* **139**: 123–134.

1076 Conine CC, Batista PJ, Gu W, Claycomb JM, Chaves DA, Shirayama M, Mello CC. 2010.
1077 Argonautes ALG-3 and ALG-4 are required for spermatogenesis-specific 26G-RNAs and
1078 thermotolerant sperm in Caenorhabditis elegans. *Proc Natl Acad Sci* **107**: 3588–3593.

1079 DeRenzo C, Reese KJ, Seydoux G. 2003. Exclusion of germ plasm proteins from somatic
1080 lineages by cullin-dependent degradation. *Nature* **424**: 685–689.

1081 Derrien B, Baumberger N, Schepetilnikov M, Viotti C, De Cillia J, Ziegler-Graff V, Isono E,
1082 Schumacher K, Genschik P. 2012. Degradation of the antiviral component
1083 ARGONAUTE1 by the autophagy pathway. *Proc Natl Acad Sci* **109**: 15942–15946.

1084 Ding S-W, Li H, Lu R, Li F, Li W-X. 2004. RNA silencing: a conserved antiviral immunity of
1085 plants and animals. *Virus Res* **102**: 109–115.

1086 Du Z, Shi K, Brown JS, He T, Wu W-S, Zhang Y, Lee H-C, Zhang D. 2023. Condensate
1087 cooperativity underlies transgenerational gene silencing. *Cell Rep* **42**.

1088 https://www.cell.com/cell-reports/abstract/S2211-1247(23)00870-7 (Accessed May 16,
1089 2024).

1090 Fassnacht C, Tocchini C, Kumari P, Gaidatzis D, Stadler MB, Ciosk R. 2018. The CSR-1
1091 endogenous RNAi pathway ensures accurate transcriptional reprogramming during the
1092 oocyte-to-embryo transition in Caenorhabditis elegans. *PLOS Genet* **14**: e1007252.

1093 Félix M-A, Ashe A, Piffaretti J, Wu G, Nuez I, Bélicard T, Jiang Y, Zhao G, Franz CJ, Goldstein
1094 LD, et al. 2011. Natural and Experimental Infection of Caenorhabditis Nematodes by
1095 Novel Viruses Related to Nodaviruses. *PLOS Biol* **9**: e1000586.

1096 Fire A, Xu S, Montgomery MK, Kostas SA, Driver SE, Mello CC. 1998. Potent and specific
1097 genetic interference by double-stranded RNA in Caenorhabditis elegans. *Nature* **391**:
1098 806–811.

1099 Fischer SEJ, Montgomery TA, Zhang C, Fahlgren N, Breen PC, Hwang A, Sullivan CM,
1100 Carrington JC, Ruvkun G. 2011. The ERI-6/7 Helicase Acts at the First Stage of an
1101 siRNA Amplification Pathway That Targets Recent Gene Duplications. *PLOS Genet* **7**:
1102 e1002369.

1103 Gallo CM, Munro E, Rasoloson D, Merritt C, Seydoux G. 2008. Processing bodies and germ
1104 granules are distinct RNA granules that interact in *C. elegans* embryos. *Dev Biol* **323**:
1105 76–87.

1106 Gent JI, Lamm AT, Pavelec DM, Maniar JM, Parameswaran P, Tao L, Kennedy S, Fire AZ.
1107 2010. Distinct Phases of siRNA Synthesis in an Endogenous RNAi Pathway in C.
1108 elegans Soma. *Mol Cell* **37**: 679–689.

1109 Gibbings D, Mostowy S, Jay F, Schwab Y, Cossart P, Voinnet O. 2012. Selective autophagy
1110 degrades DICER and AGO2 and regulates miRNA activity. *Nat Cell Biol* **14**: 1314–1321.

1111 Greg Hannon. 2010. FASTX-Toolkit: FASTQ/a short-reads pre-processing tools.
1112 http://hannonlab.cshl.edu/fastx_toolkit/.

1113 Gu W, Shirayama M, Conte D, Vasale J, Batista PJ, Claycomb JM, Moresco JJ, Youngman EM,
1114 Keys J, Stoltz MJ, et al. 2009. Distinct Argonaute-Mediated 22G-RNA Pathways Direct
1115 Genome Surveillance in the C. elegans Germline. *Mol Cell* **36**: 231–244.

1116 Guang S, Bochner AF, Pavelec DM, Burkhart KB, Harding S, Lachowiec J, Kennedy S. 2008.
1117 An Argonaute Transports siRNAs from the Cytoplasm to the Nucleus. *Science* **321**: 537–
1118 541.

1119 Han T, Manoharan AP, Harkins TT, Bouffard P, Fitzpatrick C, Chu DS, Thierry-Mieg D, Thierry-
1120 Mieg J, Kim JK. 2009. 26G endo-siRNAs regulate spermatogenic and zygotic gene
1121 expression in Caenorhabditis elegans. *Proc Natl Acad Sci* **106**: 18674–18679.

1122 Han W, Sundaram P, Kenjale H, Grantham J, Timmons L. 2008. The Caenorhabditis elegans
1123 rsd-2 and rsd-6 Genes Are Required for Chromosome Functions During Exposure to
1124 Unfavorable Environments. *Genetics* **178**: 1875–1893.

1125 Höck J, Meister G. 2008. The Argonaute protein family. *Genome Biol* **9**: 210.

1126 Huang X, Feng X, Yan Y, Xu D, Wang K, Zhu C, Dong M, Huang X, Guang S, Chen X. 2024.
1127 Compartmentalized localization of perinuclear proteins within germ granules in C.
1128 elegans. 2024.03.25.586584.
1129 https://www.biorxiv.org/content/10.1101/2024.03.25.586584v1 (Accessed December 25,
1130 2024).

1131 Ishidate T, Ozturk AR, Durning DJ, Sharma R, Shen E, Chen H, Seth M, Shirayama M, Mello
1132 CC. 2018. ZNFX-1 Functions within Perinuclear Nuage to Balance Epigenetic Signals.
1133 *Mol Cell* **70**: 639-649.e6.

1134 Ji CH, Kwon YT. 2017. Crosstalk and Interplay between the Ubiquitin-Proteasome System and
1135 Autophagy. *Mol Cells* **40**: 441–449.

1136 Jin Q, Feng X, Hong M, Wang K, Chen X, Cheng J, Kuang Y, Si X, Xu M, Huang X, et al. 2024.
1137 Peri-centrosomal localization of small interfering RNAs in C. elegans.
1138 2024.07.11.603161. https://www.biorxiv.org/content/10.1101/2024.07.11.603161v1
1139 (Accessed December 25, 2024).

1140 Klionsky DJ. 2005. The molecular machinery of autophagy: unanswered questions. *J Cell Sci*
1141 **118**: 7–18.

1142 Langmead B, Salzberg SL. 2012. Fast gapped-read alignment with Bowtie 2. *Nat Methods* **9**:
1143 357–359.

1144 Lewis A, Berkyurek AC, Greiner A, Sawh AN, Vashisht A, Merrett S, Flamand MN,
1145 Wohlschlegel J, Sarov M, Miska EA, et al. 2020. A Family of Argonaute-Interacting
1146 Proteins Gates Nuclear RNAi. *Mol Cell* **78**: 862-875.e8.

1147 Liao Y, Smyth GK, Shi W. 2014. featureCounts: an efficient general purpose program for
1148 assigning sequence reads to genomic features. *Bioinformatics* **30**: 923–930.

1149 Liu J, Carmell MA, Rivas FV, Marsden CG, Thomson JM, Song J-J, Hammond SM, Joshua-Tor
1150 L, Hannon GJ. 2004. Argonaute2 Is the Catalytic Engine of Mammalian RNAi. *Science*
1151 **305**: 1437–1441.

1152 Ma J-B, Yuan Y-R, Meister G, Pei Y, Tuschl T, Patel DJ. 2005. Structural basis for 5′-end-
1153 specific recognition of guide RNA by the A. fulgidus Piwi protein. *Nature* **434**: 666–670.

1154 Manage KI, Rogers AK, Wallis DC, Uebel CJ, Anderson DC, Nguyen DAH, Arca K, Brown KC,
1155 Cordeiro Rodrigues RJ, de Albuquerque BF, et al. 2020. A tudor domain protein, SIMR-
1156 1, promotes siRNA production at piRNA-targeted mRNAs in C. elegans eds. O. Hobert
1157 and J.L. Manley. *eLife* **9**: e56731.

1158 Mao H, Zhu C, Zong D, Weng C, Yang X, Huang H, Liu D, Feng X, Guang S. 2015. The Nrde
1159 Pathway Mediates Small-RNA-Directed Histone H3 Lysine 27 Trimethylation in
1160 Caenorhabditis elegans. *Curr Biol* **25**: 2398–2403.

1161 McEwan DL, Weisman AS, Hunter CP. 2012. Uptake of Extracellular Double-Stranded RNA by
1162 SID-2. *Mol Cell* **47**: 746–754.

1163 Meister G, Landthaler M, Patkaniowska A, Dorsett Y, Teng G, Tuschl T. 2004. Human
1164 Argonaute2 Mediates RNA Cleavage Targeted by miRNAs and siRNAs. *Mol Cell* **15**:
1165 185–197.

1166 Mizushima N. 2007. Autophagy: process and function. *Genes Dev* **21**: 2861–2873.

1167 Nakatogawa H, Suzuki K, Kamada Y, Ohsumi Y. 2009. Dynamics and diversity in autophagy
1168 mechanisms: lessons from yeast. *Nat Rev Mol Cell Biol* **10**: 458–467.

1169 Nedelsky NB, Todd PK, Taylor JP. 2008. Autophagy and the ubiquitin-proteasome system:
1170 Collaborators in neuroprotection. *Biochim Biophys Acta BBA - Mol Basis Dis* **1782**: 691–
1171 699.

1172 Nguyen DAH, Phillips CM. 2021. Arginine methylation promotes siRNA-binding specificity for a
1173 spermatogenesis-specific isoform of the Argonaute protein CSR-1. *Nat Commun* **12**:
1174 4212.

1175 Ouyang JPT, Folkmann A, Bernard L, Lee C-Y, Seroussi U, Charlesworth AG, Claycomb JM,
1176 Seydoux G. 2019. P Granules Protect RNA Interference Genes from Silencing by
1177 piRNAs. *Dev Cell* **50**: 716-728.e6.

1178 Padeken J, Methot S, Zeller P, Delaney CE, Kalck V, Gasser SM. 2021. Argonaute NRDE-3
1179 and MBT domain protein LIN-61 redundantly recruit an H3K9me3 HMT to prevent
1180 embryonic lethality and transposon expression. *Genes Dev* **35**: 82–101.

1181 Pak J, Fire A. 2007. Distinct Populations of Primary and Secondary Effectors During RNAi in C.
1182 elegans. *Science* **315**: 241–244.

1183 Parker R, Sheth U. 2007. P Bodies and the Control of mRNA Translation and Degradation. *Mol*
1184 *Cell* **25**: 635–646.

1185 Phillips CM, McDonald KL, Dernburg AF. 2009. Cytological Analysis of Meiosis in
1186 Caenorhabditis elegans. In *Meiosis: Volume 2, Cytological Methods* (ed. S. Keeney),
1187 *Methods in Molecular Biology*, pp. 171–195, Humana Press, Totowa, NJ
1188 https://doi.org/10.1007/978-1-60761-103-5_11 (Accessed July 21, 2023).

1189 Phillips CM, Montgomery BE, Breen PC, Roovers EF, Rim Y-S, Ohsumi TK, Newman MA, van
1190 Wolfswinkel JC, Ketting RF, Ruvkun G, et al. 2014. MUT-14 and SMUT-1 DEAD Box
1191 RNA Helicases Have Overlapping Roles in Germline RNAi and Endogenous siRNA
1192 Formation. *Curr Biol* **24**: 839–844.

1193 Phillips CM, Montgomery TA, Breen PC, Ruvkun G. 2012. MUT-16 promotes formation of
1194 perinuclear Mutator foci required for RNA silencing in the C. elegans germline. *Genes*
1195 *Dev* **26**: 1433–1444.

1196 Pitt JN, Schisa JA, Priess JR. 2000. P Granules in the Germ Cells of *Caenorhabditis elegans*
1197 Adults Are Associated with Clusters of Nuclear Pores and Contain RNA. *Dev Biol* **219**:
1198 315–333.

1199 Putnam A, Thomas L, Seydoux G. 2023. RNA granules: functional compartments or incidental
1200 condensates? *Genes Dev* **37**: 354–376.

1201 Quarato P, Singh M, Cornes E, Li B, Bourdon L, Mueller F, Didier C, Cecere G. 2021. Germline
1202 inherited small RNAs facilitate the clearance of untranslated maternal mRNAs in C.
1203 elegans embryos. *Nat Commun* **12**: 1441.

1204 Reinke V, Gil IS, Ward S, Kazmer K. 2004. Genome-wide germline-enriched and sex-biased
1205 expression profiles in Caenorhabditis elegans. *Development* **131**: 311–323.

1206 Robinson MD, McCarthy DJ, Smyth GK. 2010. edgeR: a Bioconductor package for differential
1207 expression analysis of digital gene expression data. *Bioinformatics* **26**: 139–140.

1208 Sakaguchi A, Sarkies P, Simon M, Doebley A-L, Goldstein LD, Hedges A, Ikegami K, Alvares
1209 SM, Yang L, LaRocque JR, et al. 2014. Caenorhabditis elegans RSD-2 and RSD-6
1210 promote germ cell immortality by maintaining small interfering RNA populations. *Proc*
1211 *Natl Acad Sci* **111**: E4323–E4331.

1212 Sarkies P, Miska EA. 2013. RNAi pathways in the recognition of foreign RNA: antiviral
1213 responses and host–parasite interactions in nematodes. *Biochem Soc Trans* **41**: 876–
1214 880.

1215 Seroussi U, Li C, Sundby AE, Lee TL, Claycomb JM, Saltzman AL. 2022. Mechanisms of
1216 epigenetic regulation by C. elegans nuclear RNA interference pathways. *Semin Cell Dev*
1217 *Biol* **127**: 142–154.

1218 Seroussi U, Lugowski A, Wadi L, Lao RX, Willis AR, Zhao W, Sundby AE, Charlesworth AG,
1219 Reinke AW, Claycomb JM. 2023. A comprehensive survey of C. elegans argonaute
1220 proteins reveals organism-wide gene regulatory networks and functions eds. D.E.
1221 James, A. Pasquenelli, and S. Kennedy. *eLife* **12**: e83853.

1222 Seydoux G, Dunn MA. 1997. Transcriptionally repressed germ cells lack a subpopulation of
1223 phosphorylated RNA polymerase II in early embryos of Caenorhabditis elegans and
1224 Drosophila melanogaster. *Development* **124**: 2191–2201.

1225 Seydoux G, Fire A. 1994. Soma-germline asymmetry in the distributions of embryonic RNAs in
1226 Caenorhabditis elegans. *Development* **120**: 2823–2834.

1227 Sheth U, Pitt J, Dennis S, Priess JR. 2010. Perinuclear P granules are the principal sites of
1228 mRNA export in adult C. elegans germ cells. *Development* **137**: 1305–1314.

1229 Shirayama M, Stanney W, Gu W, Seth M, Mello CC. 2014. The Vasa Homolog RDE-12
1230 Engages Target mRNA and Multiple Argonaute Proteins to Promote RNAi in C. elegans.
1231 *Curr Biol* **24**: 845–851.

1232 Shukla A, Yan J, Pagano DJ, Dodson AE, Fei Y, Gorham J, Seidman JG, Wickens M, Kennedy
1233 S. 2020. poly(UG)-tailed RNAs in genome protection and epigenetic inheritance. *Nature*
1234 **582**: 283–288.

1235 Sijen T, Fleenor J, Simmer F, Thijssen KL, Parrish S, Timmons L, Plasterk RHA, Fire A. 2001.
1236 On the Role of RNA Amplification in dsRNA-Triggered Gene Silencing. *Cell* **107**: 465–
1237 476.

1238 Singh M, Cornes E, Li B, Quarato P, Bourdon L, Dingli F, Loew D, Proccacia S, Cecere G.
1239 2021. Translation and codon usage regulate Argonaute slicer activity to trigger small
1240 RNA biogenesis. *Nat Commun* **12**: 3492.

1241 Spracklin G, Fields B, Wan G, Becker D, Wallig A, Shukla A, Kennedy S. 2017. The RNAi
1242 Inheritance Machinery of Caenorhabditis elegans. *Genetics* **206**: 1403–1416.

1243 Strome S, Wood WB. 1983. Generation of asymmetry and segregation of germ-line granules in
1244 early C. elegans embryos. *Cell* **35**: 15–25.

1245 Tijsterman M, May RC, Simmer F, Okihara KL, Plasterk RHA. 2004. Genes Required for
1246 Systemic RNA Interference in Caenorhabditis elegans. *Curr Biol* **14**: 111–116.

1247 Uebel CJ, Agbede D, Wallis DC, Phillips CM. 2020. Mutator Foci Are Regulated by
1248 Developmental Stage, RNA, and the Germline Cell Cycle in Caenorhabditis elegans. *G3*
1249 *GenesGenomesGenetics* **10**: 3719–3728.

1250 Uebel CJ, Manage KI, Phillips CM. 2021. SIMR foci are found in the progenitor germ cells of C.
1251 elegans embryos. *MicroPublication Biol*.
1252 https://www.micropublication.org/journals/biology/micropub-biology-000374 (Accessed
1253 May 16, 2024).

1254 Uebel CJ, Rajeev S, Phillips CM. 2023. Caenorhabditis elegans germ granules are present in
1255 distinct configurations and assemble in a hierarchical manner. *Dev Camb Engl* **150**.
1256 http://eutils.ncbi.nlm.nih.gov/entrez/eutils/elink.fcgi?dbfrom=pubmed&id=38009921&retm
1257 ode=ref&cmd=prlinks.

1258 Updike D, Strome S. 2010. P Granule Assembly and Function in Caenorhabditis elegans Germ
1259 Cells. *J Androl* **31**: 53–60.

1260 Vasale JJ, Gu W, Thivierge C, Batista PJ, Claycomb JM, Youngman EM, Duchaine TF, Mello
1261 CC, Conte D. 2010. Sequential rounds of RNA-dependent RNA transcription drive
1262 endogenous small-RNA biogenesis in the ERGO-1/Argonaute pathway. *Proc Natl Acad*
1263 *Sci* **107**: 3582–3587.

1264 Walker AK, Boag PR, Blackwell TK. 2007. Transcription reactivation steps stimulated by oocyte
1265 maturation in *C. elegans*. *Dev Biol* **304**: 382–393.

1266 Wan G, Fields BD, Spracklin G, Shukla A, Phillips CM, Kennedy S. 2018. Spatiotemporal
1267 regulation of liquid-like condensates in epigenetic inheritance. *Nature* **557**: 679–683.

1268 Wang JT, Seydoux G. 2013. Germ Cell Specification. In *Germ Cell Development in C. elegans*
1269 (ed. T. Schedl), *Advances in Experimental Medicine and Biology*, pp. 17–39, Springer,
1270 New York, NY https://doi.org/10.1007/978-1-4614-4015-4_2 (Accessed November 15,
1271 2023).

1272 Winston WM, Sutherlin M, Wright AJ, Feinberg EH, Hunter CP. 2007. Caenorhabditis elegans
1273 SID-2 is required for environmental RNA interference. *Proc Natl Acad Sci* **104**: 10565–
1274 10570.

1275 Woodland HR. 1987. Gene activity in early development. Third edition. *Cell* **49**: 305–306.

1276 Yang H, Vallandingham J, Shiu P, Li H, Hunter CP, Mak HY. 2014. The DEAD Box Helicase
1277 RDE-12 Promotes Amplification of RNAi in Cytoplasmic Foci in C. elegans. *Curr Biol* **24**:
1278 832–838.

1279 Yigit E, Batista PJ, Bei Y, Pang KM, Chen C-CG, Tolia NH, Joshua-Tor L, Mitani S, Simard MJ,
1280 Mello CC. 2006. Analysis of the C. elegans Argonaute Family Reveals that Distinct
1281 Argonautes Act Sequentially during RNAi. *Cell* **127**: 747–757.

1282 Zagoskin MV, Wang J, Neff AT, Veronezi GMB, Davis RE. 2022. Small RNA pathways in the
1283 nematode Ascaris in the absence of piRNAs. *Nat Commun* **13**: 837.

1284 Zhang C, Montgomery TA, Fischer SEJ, Garcia SMDA, Riedel CG, Fahlgren N, Sullivan CM,
1285 Carrington JC, Ruvkun G. 2012. The Caenorhabditis elegans RDE-10/RDE-11 Complex
1286 Regulates RNAi by Promoting Secondary siRNA Amplification. *Curr Biol* **22**: 881–890.

1287 Zhang L, Ward JD, Cheng Z, Dernburg AF. 2015. The auxin-inducible degradation (AID) system
1288 enables versatile conditional protein depletion in C. elegans. *Development* **142**: 4374–
1289 4384.

1290 Zhang P, Zhang H. 2013. Autophagy modulates miRNA-mediated gene silencing and
1291 selectively degrades AIN-1/GW182 in C. elegans. *EMBO Rep* **14**: 568–576.

1292 Zhang Y, Yan L, Zhou Z, Yang P, Tian E, Zhang K, Zhao Y, Li Z, Song B, Han J, et al. 2009.
1293 SEPA-1 Mediates the Specific Recognition and Degradation of P Granule Components
1294 by Autophagy in C. elegans. *Cell* **136**: 308–321.

1295

1296 **Figure Legends**

1297 **Figure 1. SIMR-1 and ENRI-2 colocalize at somatic granules in embryos.**

1298 A. Summary of IP-mass spectrometry interactions detected between NRDE-3, ENRI-2,
1299 ENRI-1, and SIMR-1 from previously published studies (Chen and Phillips, 2024, Lewis
1300 *et al.*, 2021). The number of replicates from which the interaction was detected relative
1301 to the total number of replicates performed is indicated.

1302 B. Live imaging of GFP::3xFLAG::NRDE-3 and SIMR-1::mCherry::2xHA; ENRI-
1303 2::2xTy1::GFP embryos at different stages (4-cell, 8-cell, 28-cell, 100-cell, 200-cell, and
1304 comma). Boxes identify the location of Z_2 and Z_3 primordial germ cells, showing that
1305 SIMR-1 is present in germ granules while ENRI-2 is not. At least five individual embryos
1306 were imaged for each genotype and stage. Scale bars, 5 µm.

1307 C. Box plot of SIMR-1::mCherry::2xHA granule number quantification at different embryonic
1308 stages (4-cell, 8-cell, 28-cell, 100-cell, and 200-cell). At least ten individual embryos at
1309 each stage were used for quantification. Each dot represents an individual embryo, and
1310 all data points are shown. Bolded midline indicates median value, box indicates the first
1311 and third quartiles, and whiskers represent the most extreme data points within 1.5 times
1312 the interquartile range. Lines connect the mean granule number for each stage, illustrating
1313 the change in number of SIMR granules across the developmental stages of the embryo.
1314 Two-tailed t-tests were performed to determine statistical significance and p-values were
1315 adjusted for multiple comparisons. See Materials and Methods for a detailed description
1316 of quantification methods.

1317

1318 **Figure 1—figure supplement 1. Summary of NRDE-3 and CSR-1 small RNA pathway and**
1319 **components.**

1320 A. Illustration of NRDE-3 and CSR-1 pathways in *C. elegans*. In the NRDE-3 pathway,
1321 primary ERGO-class 26G-RNAs are synthesized by the ERI complex, including ERI-1.
1322 The primary Argonaute protein, ERGO-1, is loaded with the ERGO-class 26G-RNAs.
1323 The secondary ERGO-dependent 22G-RNAs, a subset of the WAGO-class 22G-RNAs,
1324 are synthesized from ERGO-1-targeted mRNAs. Their synthesis depends on the Mutator
1325 complex, which includes the RNA-dependent RNA polymerase, RRF-1, and the
1326 poly(UG) polymerase, RDE-3. They are subsequently loaded into NRDE-3 and other
1327 cytoplasmic WAGO-family Argonaute proteins to promote gene silencing. In the CSR-1
1328 pathway, the CSR-class 22G-RNAs are synthesized by the RNA-dependent RNA

1329 polymerase, EGO-1. CSR-1 is loaded with CSR-class 22G-RNAs to promote gene
1330 licensing in the germline and clearance of maternal transcripts in early embryos.
1331 B. A table summarizing the function of some key proteins in NRDE-3 and CSR-1 pathways.
1332
1333 **Figure 1—figure supplement 2. Expression of NRDE-3, SIMR-1, and ENRI-1.**
1334 A. Live imaging of the germline from SIMR-1::mCherry::2xHA; GFP::3xFLAG::NRDE-3 day-
1335 one-old adult animals. Late pachytene (left) and oocyte (right) regions are shown,
1336 revealing that SIMR-1 and NRDE-3 do not colocalize in the germline. At least seven
1337 individual germlines were imaged. Scale bars, 5 μm.
1338 B. Live imaging of SIMR-1::GFP(R159C)::GFP::3xFLAG embryo at 100-cell stage, showing
1339 that SIMR-1(R159C) fails to not localize to cytoplasmic granules. At least five individual
1340 embryos were imaged. Scale bars, 5 μm.
1341 C. Live imaging of 2xTy1::GFP::ENRI-1 (top two rows) and ENRI-1::mCherry::2xHA
1342 (bottom two rows) embryos at different stages (4-cell, 8-cell, 28-cell, 100-cell, 200-cell,
1343 and comma). Fluorescence and brightfield channels are shown, demonstrating that
1344 ENRI-1 does not show prominent localization in embryos. At least seven individual
1345 embryos were imaged for each genotype and stage. Scale bars, 5 μm.
1346 D. Western blot of ENRI-1::mCherry::2xHA (left lane) and wild-type (right lane) gravid adult
1347 animals (72 hours at 20°C after L1 arrest), showing that the ENRI-1::mCherry::2xHA is
1348 expressed in this strain. Anti-HA-HRP and anti-actin antibodies were used for the
1349 western blot. Source data of the original blot is provided.
1350
1351 **Figure 2. Unloaded NRDE-3 localizes to cytoplasmic granules with SIMR-1.**
1352 A. Live imaging of GFP::3xFLAG::NRDE-3 embryos in *eri-1*, *rde-3*, and *nrde-3(HK-AA)*
1353 mutants at 8-cell, 100-cell, and comma stage embryos. At least five individual embryos
1354 were imaged for each genotype and stage. Arrows point to granule localization of
1355 NRDE-3 in the 100-cell stage. Asterisks highlight the nuclear localization of NRDE-3 in
1356 somatic cells of the 100-cell stage embryos and in the primordial germ cells of the
1357 comma stage embryos. Scale bars, 5 μm.
1358 B. Box plot of GFP::3xFLAG::NRDE-3 granule number quantification in different mutants.
1359 C. Box plot of GFP::3xFLAG::NRDE-3(HK-AA) granule number quantification at different
1360 embryonic stages. Lines connect the mean granule number (red dots) for each stage,
1361 illustrating the change in change in number of NRDE-3 granules across embryonic
1362 development.

1363 D. Live imaging of SIMR-1::mCherry::2xHA; GFP::3xFLAG::NRDE-3(HK-AA) at 100-cell
1364 stage. Arrows and insets show examples of colocalization between SIMR-1 and NRDE-
1365 3(HK-AA). At least ten individual embryos were imaged. Scale bars, 5 μm.
1366 For box plots in B and C, at least twelve individual embryos in each mutant were used for
1367 quantification. Each dot represents an individual embryo, and all data points are shown.
1368 Bolded midline indicates median value, box indicates the first and third quartiles, and
1369 whiskers represent the most extreme data points within 1.5 times the interquartile range.
1370 Two-tailed t-tests were performed to determine statistical significance and p-values were
1371 adjusted for multiple comparisons. See Materials and Methods for a detailed description
1372 of quantification methods.
1373

1374 **Figure 2—figure supplement 1. NRDE-3 and SIMR-1 localization and expression in**
1375 **various mutants.**

1376 A. Live imaging of GFP::3xFLAG::NRDE-3 embryos in the *simr-1* mutant, *enri-1* mutant,
1377 *enri-2* mutant, and *enri-1; enri-2* double mutant in 8-cell, 100-cell, and comma stage
1378 embryos. At least five individual embryos were imaged for each genotype and stage.
1379 B. Western blot of wild-type N_2, GFP::NRDE-3, and GFP::NRDE-3(HK-AA) mixed staged
1380 embryos, showing that the level of NRDE-3 protein is not significantly changed in the
1381 *nrde-3(HK-AA)* mutant compared to GFP::NRDE-3. Anti-FLAG and anti-ACTIN
1382 antibodies to detect NRDE-3 and ACTIN, respectively.
1383 C. Live imaging of SIMR-1::mCherry::2xHA; GFP::3xFLAG::NRDE-3 embryos in an *eri-1*
1384 mutant at the 100-cell stage. Arrows point to examples of colocalization between SIMR-1
1385 and NRDE-3. At least five individual embryos were imaged. Dotted white line indicates
1386 the outline of the embryo.
1387 D. Box plot quantifying the number of SIMR-1::mCherry::2xHA granules in a *nrde-3(HK-AA)*
1388 mutant at different embryonic stages. At least twelve individual embryos for each
1389 genotype were used for quantification. Each dot represents an individual embryo, and all
1390 data points are shown. Bolded midline indicates median value, box indicates the first and
1391 third quartiles, and whiskers represent the most extreme data points within 1.5 times the
1392 interquartile range. Lines connect the mean granule number (red dots) at each stage,
1393 illustrating the change in number of SIMR-1 granules across embryonic development.
1394 Two-tailed t-tests were performed to determine statistical significance and p-values were
1395 adjusted for multiple comparisons. See Materials and Methods for a detailed description
1396 of quantification methods.

1397 E. Live imaging of germline regions from SIMR-1::mCherry::2xHA; GFP::3xFLAG::NRDE-
1398 3(HK-AA) day-one-old adult animals shows that SIMR-1 and NRDE-3(HK-AA) do not
1399 colocalize and NRDE-3(HK-AA) does not form foci in the germline (late pachytene (top)
1400 and oocyte (bottom)). At least five individual germlines were imaged. All scale bars, 5
1401 μm. Source data are provided as a Source Data file.
1402

1403 **Figure 3. SIMR-1 recruits ENRI-2 and then NRDE-3 to cytoplasmic granules.**

1404 A. Live imaging of GFP::3xFLAG::NRDE-3(HK-AA) embryos in *simr-1* and *enri-2* mutants,
1405 and GFP::3xFLAG::NRDE-3 embryos in a *simr-1; eri-1* double mutant at 8-cell, 100-cell,
1406 and comma stages. At least five individual embryos were imaged for each genotype and
1407 stage. Asterisk marks the nuclear localization of GFP::NRDE-3 in the *simr-1; eri-1*
1408 mutant, visible in somatic cells of 8- and 100-cell stage embryos and in a primordial
1409 germ cell of the comma stage embryo. Scale bars, 5 μm.
1410 B. Live imaging of ENRI-2::2xTy1::GFP embryos in a *simr-1* mutant and SIMR-
1411 1::GFP::3xFLAG embryos in an *enri-2* mutant. At least five individual embryos were
1412 imaged for each genotype and stage. Arrows point to examples of cytoplasmic SIMR
1413 granules still visible in the *enri-2* mutant. Box surrounds a primordial germ cell displaying
1414 germ granule localization of SIMR-1. Scale bars, 5 μm.
1415

1416 **Figure 3—figure supplement 1**. **NRDE-3(HK-AA) and ENRI-1 localization in various**
1417 **mutants.**

1418 A. Western blot of wild-type (N2), GFP::NRDE-3, GFP::NRDE-3; *simr-1*, GFP::NRDE-3(HK-
1419 AA), GFP::NRDE-3(HK-AA); *simr-1* mixed staged embryos, showing that the
1420 GFP::NRDE-3 and GFP::NRDE-3(HK-AA) does not exhibit higher expression level in the
1421 *simr-1* mutant. Anti-FLAG and anti-ACTIN antibodies were used to detect NRDE-3 and
1422 ACTIN, respectively.
1423 B. Live imaging of GFP::3xFLAG::NRDE-3(HK-AA) embryos in an *enri-1* mutant and an
1424 *enri-1; enri-2* double mutant. At least five individual embryos were imaged for each
1425 genotype and stage. Arrows point to cytoplasmic NRDE-3(HK-AA) granules visible in an
1426 *enri-1* mutant. Scale bars, 5 μm.
1427 C. Live imaging of ENRI-1::mCherry::2xHA embryo in an *enri-2* mutant at 100-cell stage.
1428 Both fluorescence (left) and brightfield (right) channels are shown to demonstrate that no
1429 specific localization can be observed for ENRI-1 in the *enri-2* mutant. At least five
1430 individual embryos were imaged. Scale bars, 5 μm.

1431 D. Live imaging of ENRI-1::mCherry::2xHA; GFP::3xFLAG::NRDE-3(HK-AA) embryo at
1432 100-cell stage, showing that no specific localization can be observed for ENRI-1 in the
1433 *nrde-3(HK-AA)* mutant. Arrows point to cytoplasmic NRDE-3(HK-AA) granules. At least
1434 five individual embryos were imaged. Scale bars, 5 μm.
1435
1436 **Figure 4. CSR and WAGO pathway proteins localize to distinct cytoplasmic granules.**
1437 A. Live imaging of SIMR-1::mCherry::2xHA; RDE-3::GFP embryo at 100-cell stage,
1438 showing that RDE-3 colocalizes with SIMR-1. At least five individual embryos were
1439 imaged for each genotype and stage. Arrowheads and insets show examples of
1440 colocalization between SIMR-1 and RDE-3 at cytoplasmic granules. Scale bars, 5 μm.
1441 B. Box plot of Pearson's R value quantifications among different pairs of proteins at 100-cell
1442 embryonic stage. At least 20 granules from at least 4 individual embryos were used for
1443 quantification. Each dot represents an individual quantification, and all data points are
1444 shown. Box indicates the first and third quartiles, and whiskers represent the most extreme
1445 data points within 1.5 times the interquartile range. See Materials and Methods for a
1446 detailed description of quantification methods.
1447 C. Live imaging of SIMR-1::GFP::3xFLAG; HA::EGO-1::mCherry::RRF-1 at 100-cell stage
1448 embryo, showing that RRF-1 colocalizes with SIMR-1. At least five individual embryos
1449 were imaged for each genotype and stage. Arrowheads and insets show examples of
1450 colocalization between SIMR-1 and RRF-1 at cytoplasmic granules. Scale bars, 5 μm.
1451 D. Live imaging of mCherry::EGO-1::GFP::RRF-1 in a *simr-1* mutant, showing that RRF-1
1452 no longer associates with cytoplasmic granules, while EGO-1 remains associated with
1453 granules in the *simr-1* mutant. At least five individual embryos were imaged. Arrowheads
1454 point to examples of cytoplasmic EGO-1 granules in a *simr-1* mutant. Insets show
1455 examples of cytoplasmic localization of RRF-1 and granule localization of EGO-1 in a
1456 *simr-1* mutant. Scale bars, 5 μm.
1457 E. Live imaging of SIMR-1::mCherry::2xHA embryos in a *mut-16* mutant at 8-cell, 100-cell,
1458 and comma stages. At least five individual embryos were imaged. Asterisks indicate
1459 spindle localization of SIMR-1 in a *mut-16* mutant. Box highlights germ granule
1460 localization of SIMR-1 in a comma-stage, *mut-16* mutant embryo. Scale bars, 5 μm.
1461 F. Live imaging of GFP::3xFLAG::CSR-1 embryos at different stages (4-cell, 28-cell, 100-
1462 cell, 200-cell, and comma), shows that CSR-1 localizes to cytoplasmic granules in early
1463 embryos and is restricted to germ granules in late embryos. At least three individual

1464 embryos were imaged for each stage. Dotted white line marks perimeter of the embryo.
1465 Box marks germ granule localization of CSR-1. Scale bars, 5 μM.
1466 G. Box plot quantifying GFP::3xFLAG::CSR-1 granules at different embryonic stages. At least
1467 ten embryos at each stage were used for quantification. Each dot represents an individual
1468 embryo, and all data points are shown. Bolded midline indicates median value, box
1469 indicates the first and third quartiles, and whiskers represent the most extreme data points
1470 within 1.5 times the interquartile range. Lines connect the mean granule number (red dots)
1471 at each stage, illustrating the change in number of CSR granules across embryonic
1472 development. Two-tailed t-tests were performed to determine statistical significance and
1473 p-values were adjusted for multiple comparisons. See Materials and Methods for a
1474 detailed description of quantification methods.
1475 H. Live imaging of mCherry::EGO-1; GFP::3xFLAG::::CSR-1 embryo at 28-cell stage,
1476 showing CSR-1 colocalization with EGO-1. At least ten individual embryos were imaged.
1477 Arrowheads and insets show examples of CSR-1 and EGO-1 colocalization at
1478 cytoplasmic granules. Scale bars, 5 μm.
1479 I. Live imaging of SIMR-1::mCherry::2xHA; GFP::3xFLAG::CSR-1 embryo at 28-cell stage,
1480 showing the absence of colocalization between SIMR-1 and CSR-1 with occasional
1481 adjacent localization. At least ten individual embryos were imaged. Arrowheads point to
1482 examples of SIMR and CSR granules that do not colocalize. Insets show examples of
1483 SIMR and CSR granules that are found adjacent to each other or fail to colocalize.
1484 Dotted white line marks perimeter of embryo. Scale bars, 5 μm.
1485 J. Model of CSR and SIMR granules in the somatic cells of *C. elegans* embryos. The
1486 RdRP EGO-1, which synthesizes CSR-class 22G-RNAs, localizes to CSR granules,
1487 where CSR-1 loading may take place. The RdRP RRF-1, along with RDE-3, ENRI-2,
1488 and unloaded NRDE-3 localize to SIMR granules. SIMR-1 and ENRI-2 recruits unloaded
1489 NRDE-3 to granule where RRF-1 may synthesize ERGO-dependent 22G-RNAs for
1490 loading into NRDE-3. After loading, NRDE-3 translocates to the nucleus and silences
1491 genes co-transcriptionally.
1492
1493 **Figure 4—figure supplement 1. SIMR-1 does not colocalize with any previously identified**
1494 **embryonic granules.**
1495 A. Live imaging of SIMR-1::GFP::3xFLAG; mCherry::CGH-1 embryo at 100-cell stage,
1496 showing that SIMR-1 does not colocalize with CGH-1. Arrowheads and insets show
1497 examples of SIMR-1 and CGH-1 granules that do not colocalize.

1498 B. Live imaging of mCherry::CGH-1; *eri-1*; GFP::3xFLAG::NRDE-3 at 100-cell stage
1499 embryo, showing that NRDE-3 in the *eri-1* mutant does not colocalize with CGH-1.
1500 Arrowheads and insets show examples of NRDE-3 and CGH-1 granules that do not
1501 colocalize.
1502 C. Live imaging of SIMR-1::GFP::3xFLAG; RSD-2::mCherry embryo at 100-cell stage,
1503 showing that RSD-2 does not localize to cytoplasmic granules in the embryo.
1504 Arrowheads and insets show examples of SIMR granules.
1505 D. Live imaging of SIMR-1::mCherry::2xHA; HRDE-2::2xTy1::GFP embryo at 100-cell
1506 stage, showing that HRDE-2 does not localize to cytoplasmic granules in the embryo.
1507 Arrowheads and insets show examples of SIMR granules.
1508 E. Live imaging of SIMR-1::GFP::3xFLAG; *hrde-2* embryo at 100-cell stage, showing that
1509 SIMR-1 still localizes to cytoplasmic granules in the hrde-2 mutant. Arrowheads and
1510 inset show examples of SIMR granules.
1511 F. Live imaging of SIMR-1::mCherry::2xHA; GFP::3xFLAG::RDE-12 embryo at 100-cell
1512 stage, showing that SIMR-1 does not colocalize with RDE-12. Arrowheads and insets
1513 show examples of RDE-12 and SIMR granules that do not colocalize.
1514 G. Live imaging of SIMR-1::mCherry::2xHA RSD-6::GFP::3xFLAG embryo at 100-cell
1515 stage, showing that SIMR-1 does not colocalize with RSD-6. Arrowheads and insets
1516 show examples of RSD-6 and SIMR granules that do not colocalize.
1517 H. Live imaging of SIMR-1::GFP::3xFLAG; HA::tagRFP::ZNFX-1 embryo at 100-cell stage,
1518 showing that SIMR-1 does not colocalize with ZNFX-1. Arrowheads and insets show
1519 examples of SIMR and ZNFX-1 granules that do not colocalize.
1520 I. Live imaging of SIMR-1::mCherry::2xHA; tubulin::GFP embryo at 100-cell stage,
1521 showing that SIMR-1 does not colocalize with tubulin. Arrowheads and insets show
1522 examples of tubulin and SIMR granules that do not colocalize.
1523 J. Live imaging of MUT-16::GFP at 100-cell stage, showing that MUT-16 localizes to
1524 somatic granules. Arrowheads and inset show examples of MUT-16 somatic granules.
1525 K. Live imaging of RDE-3::GFP in a *mut-16* mutant embryo at 100-cell stage, showing that
1526 RDE-3 no longer associates with granules in the *mut-16* mutant.
1527 L. Live imaging of SIMR-1::GFP::3xFLAG; mCherry::EGO-1 embryo at 100-cell stage,
1528 showing that SIMR-1 does not colocalize with EGO-1. Arrowheads and insets show
1529 examples of SIMR-1 and EGO-1 granules that do not colocalize. At least five individual
1530 embryos were imaged for all experiments. All scale bars, 5 μm.
1531

1532 **Figure 5. Autophagy regulates the removal of SIMR granules and other embryonic**
1533 **granules.**

1534 A. Live imaging of SIMR-1::mCherry and PGL-1::BFP at 8-cell, 100-cell, and comma stage
1535 embryos following treatment of parental animals with control (L4440) and *lgg-1* RNAi. At
1536 least ten individual embryos were imaged for each genotype and stage. Dotted white line
1537 marks perimeter of embryo. Scale bars, 5 μm.

1538 B. Box plot quantifying the number of SIMR granules at the 100-cell stage following
1539 treatment of parental animals with control (L4440) and *lgg-1* RNAi. Fourteen embryos at
1540 each stage were used for quantification. Each dot represents an individual embryo, and
1541 all data points are shown. Bolded midline indicates median value, box indicates the first
1542 and third quartiles, and whiskers represent the most extreme data points within 1.5 times
1543 the interquartile range. Two-tailed t-test was performed to determine statistical
1544 significance.

1545 C. Live imaging of GFP::CSR-1 and RFP::ZNFX-1 at 8-cell, 100-cell, and comma stage
1546 embryos following treatment of parental animals with control (L4440) and *lgg-1* RNAi. At
1547 least ten individual embryos were imaged for each genotype and stage. Dotted white line
1548 marks perimeter of embryo. Scale bars, 5 μm.

1549 D. Live imaging of SIMR-1::GFP; RFP::ZNFX-1; PGL-1::BFP embryo and SIMR-
1550 1::mCherry; GFP::CSR-1 embryo at 100-cell stage embryos following treatment of
1551 parental animals with *lgg-1* RNAi. At least ten individual embryos were imaged for each
1552 genotype. Dotted white line marks perimeter of embryo. Insets show examples of
1553 granule adjacency. Scale bars for embryos, 5 μm. Scale bars for insets, 0.2 μm.

1554 Images in A, C-D are maximum projections of deconvolved 12.5 μm z-stacks (about two-
1555 third of embryo depth).

1556

1557 **Figure 5—figure supplement 1. Components of the SIMR granule are regulated by**
1558 **autophagy.**

1559 A. Live imaging of GFP::NRDE-3; *eri-1* at 8-cell, 100-cell, and comma stage embryos
1560 following treatment of parental animals with control (L4440) and *lgg-1* RNAi . At least ten
1561 individual embryos were imaged for each genotype and stage. Scale bars, 5 μm. Images
1562 are maximum projections of deconvolved 12.5 μm z-stacks (about two-third of embryo
1563 depth).

1564 B. Box plot quantifying Pearson's R values of SIMR-1 with ENRI-2, RDE-3/MUT-2, RRF-1,
1565 and NRDE-3; *eri-1* at comma stage on *lgg-1* RNAi condition. At least twenty embryos at

1566 each stage were used for quantification. Each dot represents an individual embryo, and
1567 all data points are shown. Bolded midline indicates median value, box indicates the first
1568 and third quartiles, and whiskers represent the most extreme data points within 1.5 times
1569 the interquartile range.
1570
1571 **Figure 6. NRDE-3 switches small RNA targets during development.**
1572 A. Diagram of IP-sRNA seq on NRDE-3 early embryos (<=100-cell stage) and late embryos
1573 (>=300-cell). GFP::FLAG::NRDE-3 was immunoprecipitated from embryo lysate and its
1574 associated small RNAs were isolated for sequencing.
1575 B. Box plots depicting $\log_2$(fold change small RNA abundance) in NRDE-3 IP compared to
1576 input for at least two biological replicates.
1577 C. Normalized NRDE-3-bound small RNA read distribution across a CSR-target gene (*ztf-*
1578 *27*) and an ERGO-target gene (Y37E11B.2) in early embryos, late embryos, and young
1579 adults. One representative replicate is shown.
1580 D. Normalized NRDE-3 IP compared to input small RNA reads in early embryos, late
1581 embryos, and young adults. CSR-target and ERGO-target genes are indicated in blue
1582 and red, respectively. One representative replicate is shown. Insets are pie charts
1583 describing numbers of CSR targets, ERGO targets, and other targets that are
1584 significantly enriched in the NRDE-3 IP. The enriched targets were defined as small
1585 RNAs with at least 2-fold enrichment in IP compared to input, average RPM >10, and p-
1586 values ≤0.05.
1587 E. Box plot depicting $\log_2$(fold change small RNA abundance) in mutants compared to wild-
1588 type in late embryos for two or three biological replicates.
1589 F. Box plots depicting $\log_2$(fold change of ERGO-class small RNA abundance) in NRDE-3
1590 IP compared to input in wild-type and mutants in late embryos for two or three biological
1591 replicates.
1592 G. Box plots depicting $\log_2$(fold change of CSR-class small RNA abundance) in NRDE-3 IP
1593 compared to input in wild-type and mutants in late embryos for two or three biological
1594 replicates.
1595 For box plots in B,E-G, bolded midline indicates median value, box indicates the first and
1596 third quartiles, and whiskers represent the most extreme data points within 1.5 times the
1597 interquartile range, excluding outliers. Two-tailed t-tests were performed to determine
1598 statistical significance and p-values were adjusted for multiple comparisons.
1599

1600 **Figure 6—figure supplement 1. Defining NRDE-3-bound ERGO-target genes.**

1601 A. Normalized NRDE-3 IP compared to input small RNA reads in young adults (left), *nrde-3*
1602 mutant compared to wild-type small RNA reads in mixed-stage embryos (middle), *nrde-3*
1603 mutant compared to wild-type mRNA reads in mixed-stage embryos (right). ERGO-
1604 target genes from *Manage et al (2020)* are indicated in yellow. One representative
1605 replicate is shown.

1606 B. Normalized NRDE-3 IP compared to input small RNA reads in young adults (left), *nrde-3*
1607 mutant compared to wild-type small RNA reads in mixed-stage embryos (middle), *nrde-3*
1608 mutant compared to wild-type mRNA reads in mixed-stage embryos (right). ERGO-
1609 target genes from *Fischer et al (2011)* are indicated in green. One representative
1610 replicate is shown.

1611 C. Normalized NRDE-3 IP compared to input small RNA reads in young adults (left), *nrde-3*
1612 mutant compared to wild-type small RNA reads in mixed-stage embryos (middle), *nrde-3*
1613 mutant compared to wild-type mRNA reads in mixed-stage embryos (right). NRDE-3-
1614 bound, ERGO-target genes are defined as genes with at least four-fold enrichment and
1615 an average of 100 RPM from the young adult NRDE-3 IP-sRNA seq libraries, and are
1616 indicated in red. One representative replicate is shown.

1617 D. Venn diagrams indicate overlap of ERGO - Manage and ERGO - Fischer targets gene
1618 lists with the newly defined NRDE-3-bound, ERGO-target genes.

1619 E. Box plots depicting log2(fold change of small RNA abundance) in a *nrde-3* mutant
1620 compared to wild-type in mixed-stage embryos for three biological replicates.

1621 F. Box plots depicting log2(fold change of mRNA abundance) in a *nrde-3* mutant compared
1622 to wild-type in mixed-stage embryos for three biological replicates.

1623 For box plots in E,F, bolded midline indicates median value, box indicates the first and
1624 third quartiles, and whiskers represent the most extreme data points within 1.5 times the
1625 interquartile range, excluding outliers. Two-tailed t-tests were performed to determine
1626 statistical significance and p-values were adjusted for multiple comparisons. Adjusted p-
1627 values are a comparison of the indicated gene list to all genes in the mixed-stage
1628 embryos.

1629

1630 **Figure 6—figure supplement 2. NRDE-3-bound small RNA in different mutants.**

1631 A. Normalized NRDE-3 IP compared to input small RNA reads in *eri-1* mutant early (left)
1632 and late (right) embryos. CSR-target and ERGO-target genes are indicated in blue and
1633 red, respectively. One representative replicate is shown.

1634 B. Normalized NRDE-3 IP compared to input small RNA reads in *simr-1* mutant (left) and
1635 *enri-2* mutant (right) late embryos. CSR-target and ERGO-target genes are indicated in
1636 blue and red, respectively. One representative replicate is shown.
1637
1638 **Figure 7. NRDE-3 associates with CSR-class 22G-RNAs in early embryos.**
1639 A. Venn diagrams indicate overlap of NRDE-3 IP enriched targets in early embryos (this
1640 work), CSR-1 IP enriched targets in young adults (Nguyen *et al.*, 2021), and CSR-1 IP
1641 enriched targets in embryos (Quarato *et al.*, 2021).
1642 B. Normalized NRDE-3 IP compared to input small RNA reads in early embryos. CSR-
1643 target genes with 1-50 RPM, with 50-100 RPM, and with more than 150 RPM are
1644 indicated in light blue, medium blue, and dark blue, respectively. One representative
1645 replicate is shown.
1646 C. Density plot of small RNA enrichment on CSR targets in CSR-1 IP (dark blue), NRDE-3
1647 IP (light blue) in embryos (left) and adults (right). Transcription start site (TSS) to
1648 transcription end site (TES) were plotted using normalized small RNA reads. All
1649 replicates are shown as individual lines.
1650 D. Box plot quantifying the number of embryos laid per adult *csr-1::degron* or *csr::degron,*
1651 *gfp::nrde-3(HK-AA)* animal on 4mM auxin plate. At least 65 individuals from each strain
1652 were scored. Each dot represents an individual animal, and all data points are shown.
1653 E. Box plot depicting $\log_2$(fold change of H3K9me3 level in IP vs input) in wild-type (grey)
1654 and *nrde-3* mutant (green) mixed-stage embryos, indicating that the H3K9me3 level of
1655 NRDE-3 targets in early embryos are not affected in *nrde-3* mutant. Anti-H3K9me3
1656 ChIP-seq data was obtained from Padeken *et al.* (2021).
1657 For box plots in D-E, bolded midline indicates median value, box indicates the first and
1658 third quartiles, and whiskers represent the most extreme data points within 1.5 times the
1659 interquartile range, excluding outliers. Two-tailed t-tests were performed to determine
1660 statistical significance and p-values were adjusted for multiple comparisons.
1661
1662 **Figure 7—figure supplement 1. NRDE-3 associates different classes of small RNAs**
1663 **during development.**
1664 A. Normalized NRDE-3 IP compared to input small RNA reads in late embryos (left) and
1665 young adults (right). CSR-target genes with 1-50 RPM, with 50-100 RPM, and with more
1666 than 150 RPM are indicated in light blue, medium blue, and dark blue, respectively. One
1667 representative replicate is shown.

1668 B. Density plot of small RNA enrichment on ERGO targets in CSR-1 IP (dark red), NRDE-3
1669 IP (light red) in the embryos (left) and adults (right). Transcription start site (TSS) to
1670 transcription end site (TES) were plotted using normalized small RNA reads. All
1671 replicates are shown as individual lines.
1672 C. Box plots depicting normalized log2(fold change of small RNA abundance in IP vs input)
1673 in a NRDE-3 IP in early embryos and CSR IP in embryos for two or three biological
1674 replicates. All genes list includes all genes expressed in IP or input. Early degraded
1675 mRNAs are maternal mRNAs that show at least twofold reduction in mRNA levels in
1676 early embryos (4 to 20 cell-stage) compared to 1-cell embryos (*Quarato et al., 2021*).
1677 Late degraded mRNAs are maternal mRNAs that show stable levels of mRNAs in early
1678 embryos and at least twofold reduction in late embryos (more than 20-cell stage)
1679 (*Quarato et al., 2021*). Zygotic mRNAs are mRNAs that are not detectable in 1-cell
1680 embryos but accumulate in early and late embryos (*Quarato et al., 2021*).
1681 D. Box plot depicting mRNA RPM in one-cell embryo (dark blue), early embryo (medium
1682 blue), and late embryo (light blue) on NRDE-3 targets in early embryos (this study) and
1683 CSR-1 targets in embryos (*Quarato et al., 2021*) (left), and mRNA RPM in one-cell
1684 embryo (dark pink), early embryo (medium pink), and late embryo (light pink) on ERGO
1685 targets (this study) (right). All biological replicates (two or three) are included. mRNA-seq
1686 data was obtained from *Quarato et al. (2021).*
1687 E. Quantification of the fertility for *csr-1::degron* and *csr-1::degron, gfp::nrde-3(HK-AA)*
1688 animals on ethanol and 4mM auxin plate. The fertility of each animal was categorized
1689 as: hatched (some embryos laid by the animal hatched), >=50 dead embryos (animal
1690 laid at least 50 unhatched embryos and no hatched embryos), <50 dead embryos
1691 (animal laid less than 50 unhatched embryos and no hatched embryos), no embryos
1692 (animal did not lay any embryos). At least 65 individual adult animals of each strain and
1693 each condition were used for quantification.
1694
1695 **Figure 8. NRDE-3 associates with CSR-class 22G-RNAs to represses RNA Polymerase II**
1696 **in oocytes.**
1697 A. Live imaging of GFP::3xFLAG::NRDE-3 in one-day-adult germlines for wild-type, *eri-1*,
1698 *rde-3*, and *nrde-3(HK-AA)* mutants, showing that NRDE-3 localizes to the nuclei of
1699 oocytes in wild-type, *eri-1* mutant, and *rde-3* mutants, and to the cytoplasm in the *nrde-*
1700 *3(HK-AA)* mutant. At least five individual gonads were imaged for each genotype. Dotted

1701 white line traces the proximal portion of the *C. elegans* gonad and outlines the individual
1702 oocytes. Scale bars, 25 μm.
1703 B. Live imaging of one-day-adult germlines and 8-cell embryos for EGO-1::degron;
1704 GFP::3xFLAG::NRDE-3 (top) and EGO-1::degron; GFP::3xFLAG::NRDE-3 in a *rde-3*
1705 mutant (bottom) with ethanol (control) and 4mM auxin treatment, showing that loss of
1706 both WAGO-class and CSR-class 22G-RNAs (*rde-3* mutant and degron-mediated EGO-
1707 1 depletion) is necessary to result in cytoplasmic localization of NRDE-3 in both oocytes
1708 and early embryos. At least five individual gonads and embryos were imaged for each
1709 treatment condition. Dotted white line traces the proximal portion of the *C. elegans*
1710 gonad and outlines the individual oocytes. Arrowheads indicate granule localized NRDE-
1711 3 in 8-cell stage embryos. Scale bars, 25 μm in adults and 5 μm in embryos.
1712 C. Box plot quantifying the RNA Pol II PSer2 signal intensity in oocytes of wild-type
1713 (GFP::NRDE-3 strain), and *nrde-3(HK-AA)* mutant (GFP::NRDE-3(HK-AA) strain),
1714 showing that PSer2 signal is significantly increased in all oocytes in the *nrde-3(HK-AA)*
1715 mutant. Each dot represents an individual oocyte, and all data points are shown. Bolded
1716 midline indicates median value, box indicates the first and third quartiles, and whiskers
1717 represent the most extreme data points within 1.5 times the interquartile range. Two-
1718 tailed t-tests were performed to determine statistical significance. See Materials and
1719 Methods for a detailed description of quantification methods.
1720 D. Bar plot quantifying the RNA Pol II PSer2 expression pattern in wild-type (GFP::NRDE-3
1721 strain), and *nrde-3(HK-AA)* mutant (GFP::NRDE-3(HK-AA) strain) oocytes, showing that
1722 the PSer2 signal is retained on DNA longer in the *nrde-3(HK-AA)* mutant. At least 10
1723 oocytes were used for quantification for each strain. Examples of three patterns of PSer2
1724 signal are shown on right. Arrows point to a region of DNA to highlight PSer2 enrichment
1725 or exclusion. Scale bars, 2 μm.
1726 E. Immunofluorescence imaging of PSer2 signal and DAPI stained DNA in oocytes of wild-
1727 type (GFP::NRDE-3), and *nrde-3(HK-AA)* mutant (GFP::NRDE-3(HK-AA)), showing that
1728 the PSer2 signal appears earlier on DNA in the *nrde-3(HK-AA)* mutant. Images are
1729 maximum intensity projections of 12.5 μm z-stack, which allows for optimal visualization
1730 of the DNA-associated PSer2 signal, but obscures the 'excluded from DNA' pattern. At
1731 least five individual animals for each genotype. Arrows indicate the PSer2 signal on
1732 DNA. Scale bars, 25 μm.
1733
1734 **Figure 9. Model for temporally- and developmentally-regulated NRDE-3 function.**

Model of NRDE-3, SIMR-1, and CSR-1 function during *C. elegans* development. In early embryos, CSR-1 and EGO-1 localize to CSR granules and synthesize CSR 22G-RNAs to slice and clear maternal mRNAs. NRDE-3 binds CSR 22G-RNA in the nucleus, which are inherited from the oocytes. During mid-embryogenesis (e.g. around the 100-cell stage), unloaded NRDE-3, ENRI-2, RRF-1, and RDE-3 are localized to SIMR granules in somatic cells dependent on SIMR-1, where we propose that ERGO-dependent 22G-RNAs are produced and loaded into NRDE-3. In late embryos, NRDE-3 binds ERGO-dependent 22G-RNAs and silences ERGO-target genes in the nucleus, while autophagy controls selective degradation of SIMR and other embryonic granules. In adult *C. elegans*, somatic localized NRDE-3 associates with ERGO-dependent 22G-RNAs to transcriptionally silence ERGO-target genes, while germline localized NRDE-3 associates with CSR-class 22G-RNAs to globally repress transcription and promote chromatin compaction in oocytes, ultimately being deposited into early embryos.

Figure 9—figure supplement 1. Predicted structures of SIMR-1, nuclear Argonaute proteins, and interactors.

A. Graph displaying disorder tendency for the SIMR-1 protein sequence and AlphaFold3 predicted structures of SIMR-1. The disorder prediction was made using PONDR (http://www.pondr.com) with VSL2 and VSL3 parameters. Regions with PONDR scores of greater than 0.5 indicate disorder and regions with PONDR score less than 0.5 indicate order. The AlphaFold3 predicted confidence score of SIMR-1 is shown. The extended Tudor domain (aa. 89-259) of SIMR-1 is highlighted in orange.
B. AlphaFold3 predicted structures of HRDE-1 - HRDE-2, and NRDE-3 - ENRI-2 complexes, showing that the C-terminus of HRDE-2 and ENRI-2 are inserted into small RNA binding pockets of HRDE-1 and NRDE-3 respectively. Domains of HRDE-1 and NRDE-3 are indicated and AlphaFold3 predicted confidence scores are shown.

Supplementary Files

Supplementary File 1. Reagents, resources, and strains used in this study.

Supplementary File 2. Oligonucleotides sequences used in this study.

Supplementary File 3. Small RNA enrichment in NRDE-3 immunoprecipitations.

Supplementary File 4. Sequencing library statistics.

Source Data Files

Figure 1—source data 1
This file contains the raw data used to generate the graph of SIMR granule number shown in Figure 1C.

Figure 1—figure supplement 2—source data 1
This file contains the original western blots of ENRI-1::mCherry::2xHA used in creating Figure 1—figure supplement 2D.

Figure 2—source data 1
This file contains the raw data used to generate the graphs of NRDE-3 granule number shown in Figure 2B-C.

Figure 2—figure supplement 1—source data 1
This file contains the original western blots of GFP::NRDE-3 used in creating Figure 2—figure supplement 1B and the raw data used to generate the graphs of NRDE-3 granule number shown in Figure 2—figure supplement 1D.

Figure 3—figure supplement 1—source data 1
This file contains the original western blots of GFP::NRDE-3 used in creating Figure 3—figure supplement 1A.

Figure 4—source data 1
This file contains the raw data used to generate the graphs of colocalization analysis and CSR-1 granule number shown in Figure 4B, G.

Figure 5—source data 1
This file contains the raw data used to generate the graph of SIMR granule number shown in Figure 5B.

Figure 5—figure supplement 1—source data 1

This file contains the raw data used to generate the graphs of colocalization analysis shown in Figure 5—figure supplement 1—source data 1B.

Figure 7—source data 1

This file contains the raw data used to generate the graph of number of embryos laid shown in Figure 7D.

Figure 8—source data 1

This file contains the raw data used to generate the graphs of oocyte PSer2 signal intensity and pattern number shown in Figure 8C-D.

A

mass spectrometry interactions				
	SIMR-1	NRDE-3	ENRI-2	ENRI-1
SIMR-1 IP (adult)	NA	2/3	0/3	0/3
NRDE-3 IP (embryo)	2/5	NA	2/5	5/5
ENRI-2 IP (embryo)	3/3	3/3	NA	0/3
ENRI-1 IP (embryo)	0/3	3/3	0/3	NA

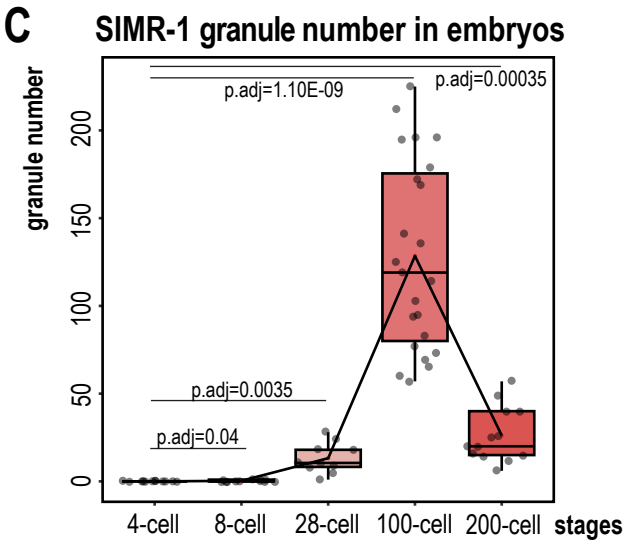

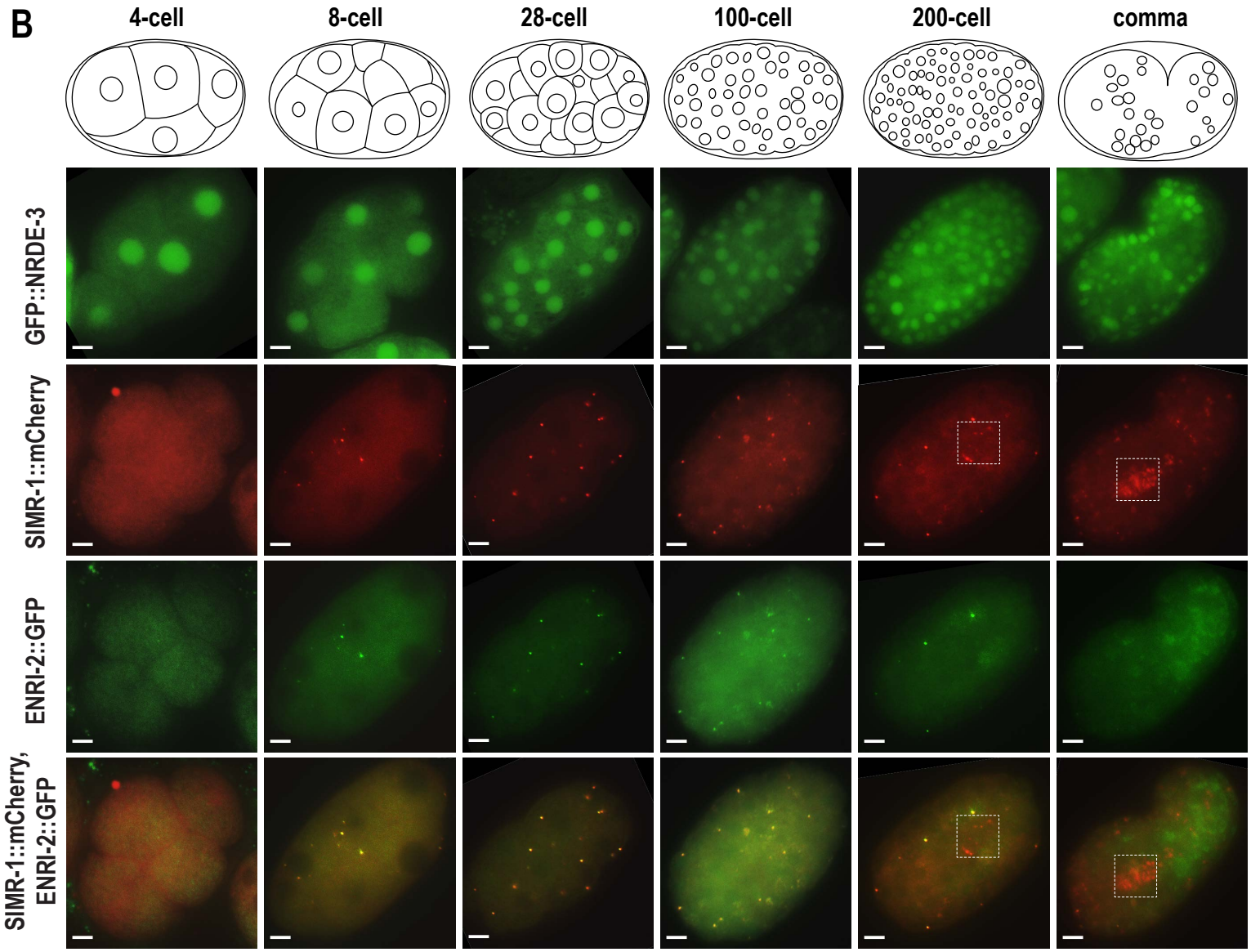

Figure 1. SIMR-1 and ENRI-2 colocalize at somatic granules in embryos.

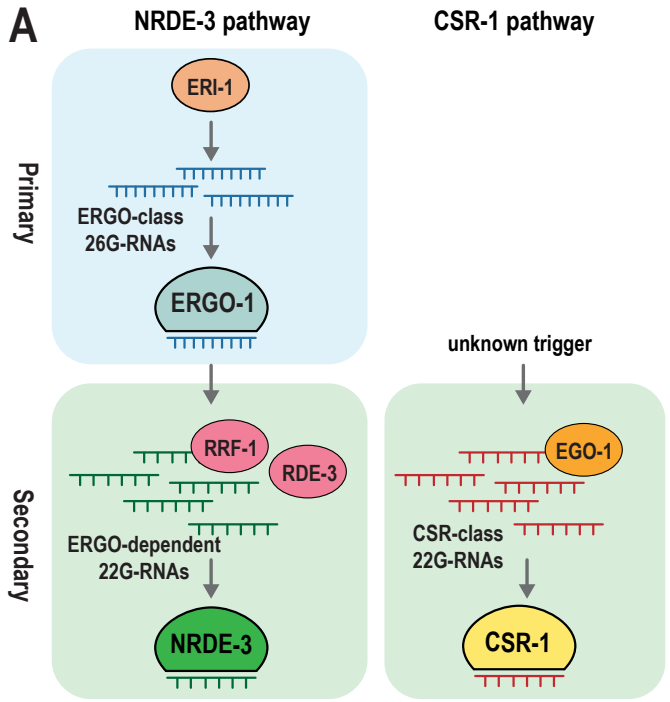

B

Summary of NRDE-3 and CSR-1 small RNA pathway proteins			
	Gene name	Description	References
NRDE-3 pathway	ERI-1	DEDDh-like 3' to 5' exonuclease, member of the ERI complex, required for 26G-RNA biogenesis	Kennedy et al., 2004
	ERGO-1	Primary Argonaute protein, binds to 26G-RNAs	Yigit et al., 2006
	RRF-1	RdRP, required for WAGO-class 22G-RNA biogenesis, and required redundantly with EGO-1 for CSR-class 22G-RNA biogenesis	Aoki et al., 2007; Gu et al., 2009
	RDE-3/MUT-2	Poly(UG) polymerase, required for WAGO-class 22G-RNA biogenesis	Phillips et al., 2012; Shukla et al., 2020
	NRDE-3	Nuclear Argonaute protein, binds to ERGO-dependent 22G-RNAs for gene silencing	Guang et al., 2008
CSR-1 pathway	EGO-1	RdRP, required for biogenesis of CSR-class 22G RNAs	Gu et al., 2009
	CSR-1	Argonaute protein, binds to CSR-class 22G-RNAs for gene licencing in the germline, and maternal transcripts clearance in early embryos	Claycomb et al., 2009; Quarato et al., 2021

Figure 1—figure supplement 1. Summary of NRDE-3 and CSR-1 small RNA pathway and components.

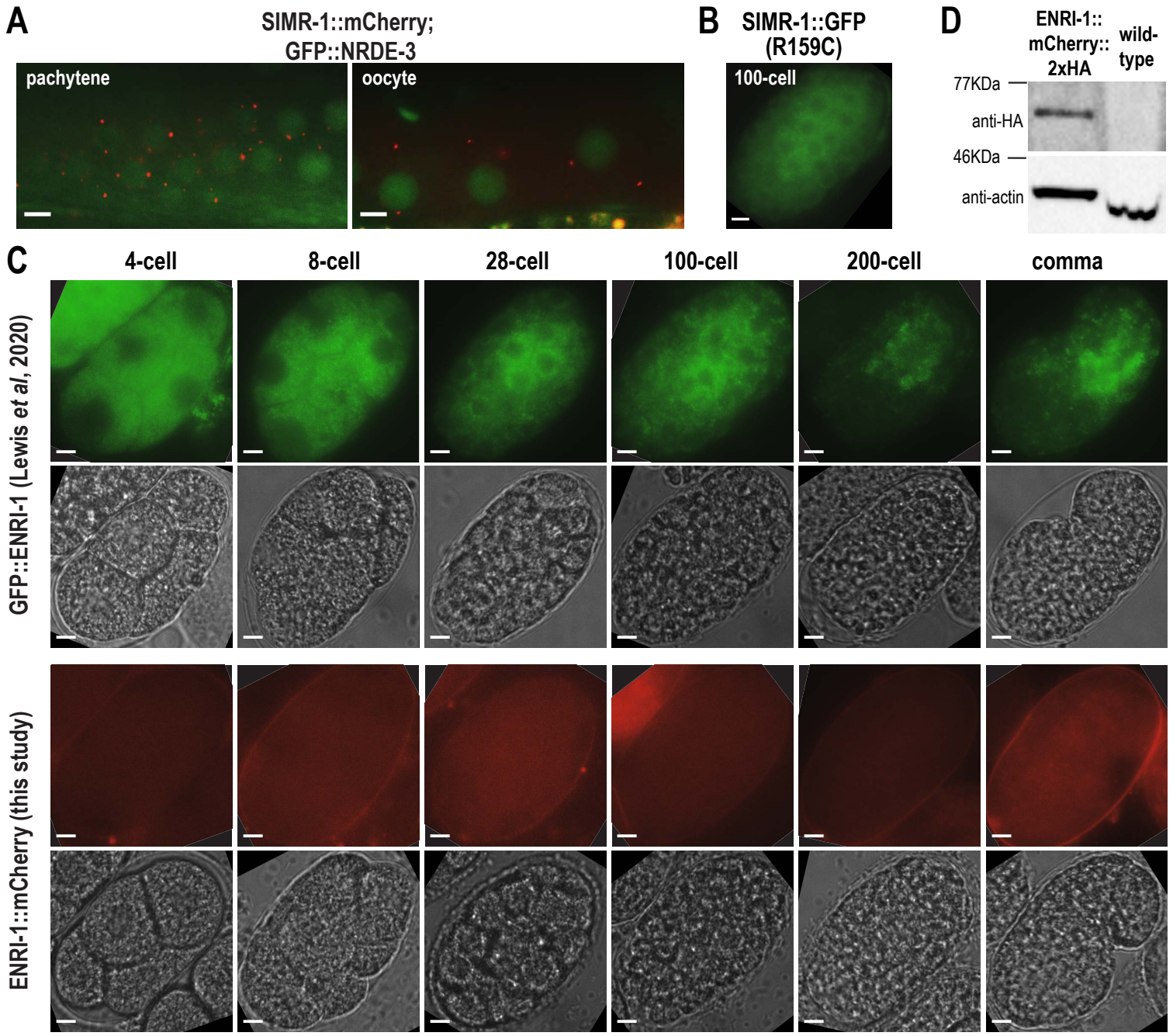

Figure 1—figure supplement 2. Expression of NRDE-3, SIMR-1, and ENRI-1.

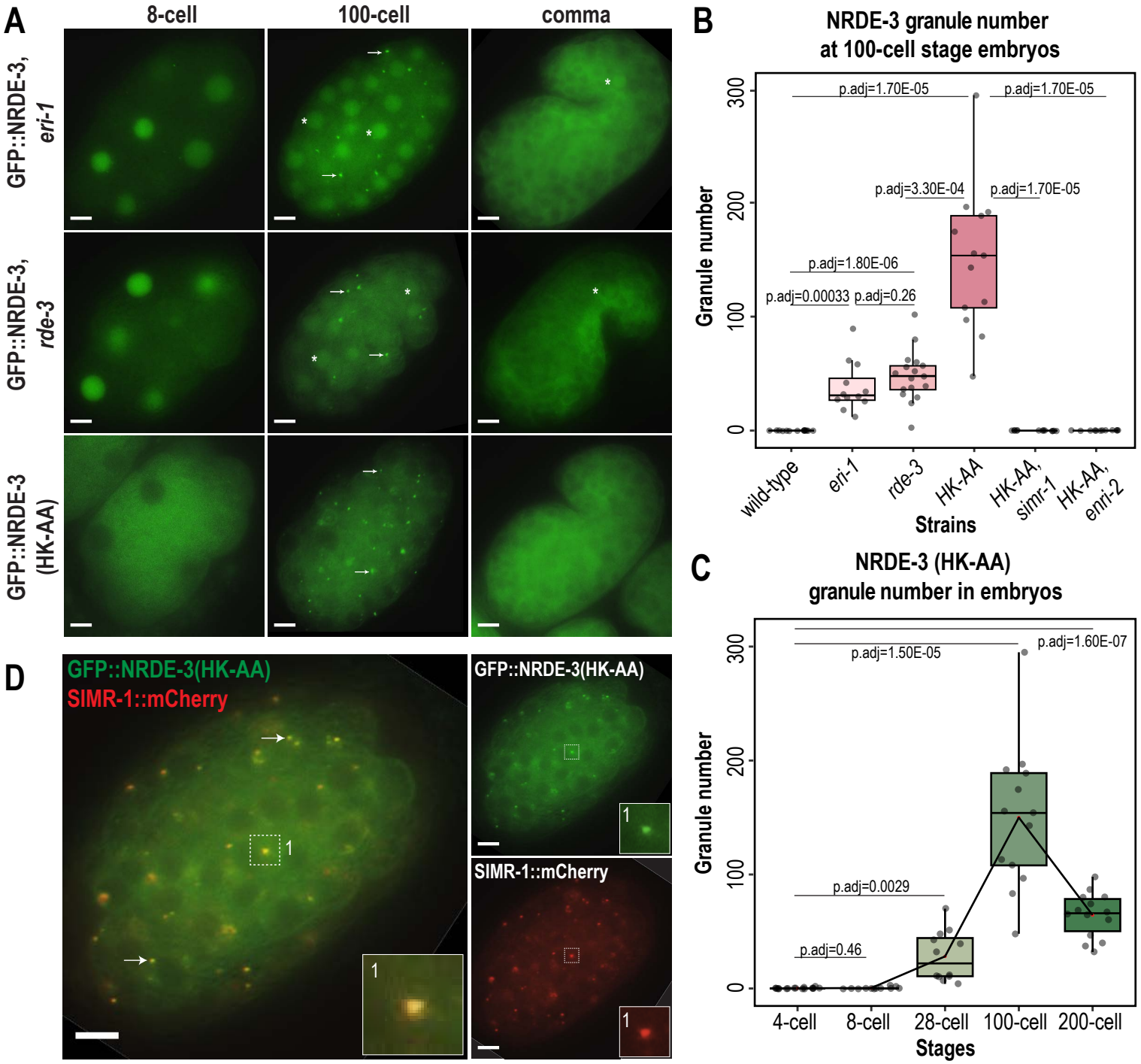

Figure 2. Unloaded NRDE-3 localizes to cytoplasmic granules with SIMR-1.

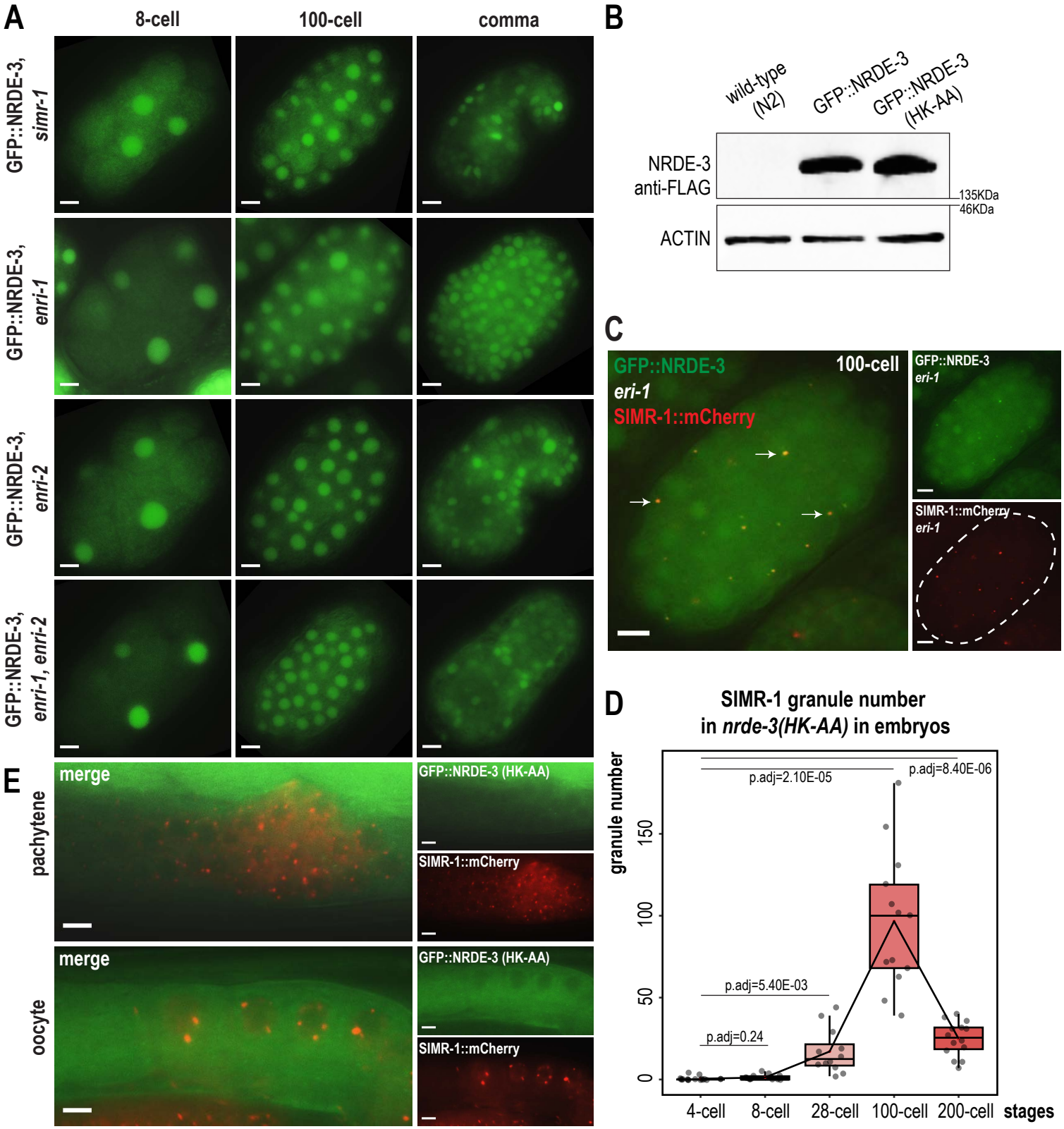

Figure 2—figure supplement 1. NRDE-3 and SIMR-1 localization and expression in various mutants.

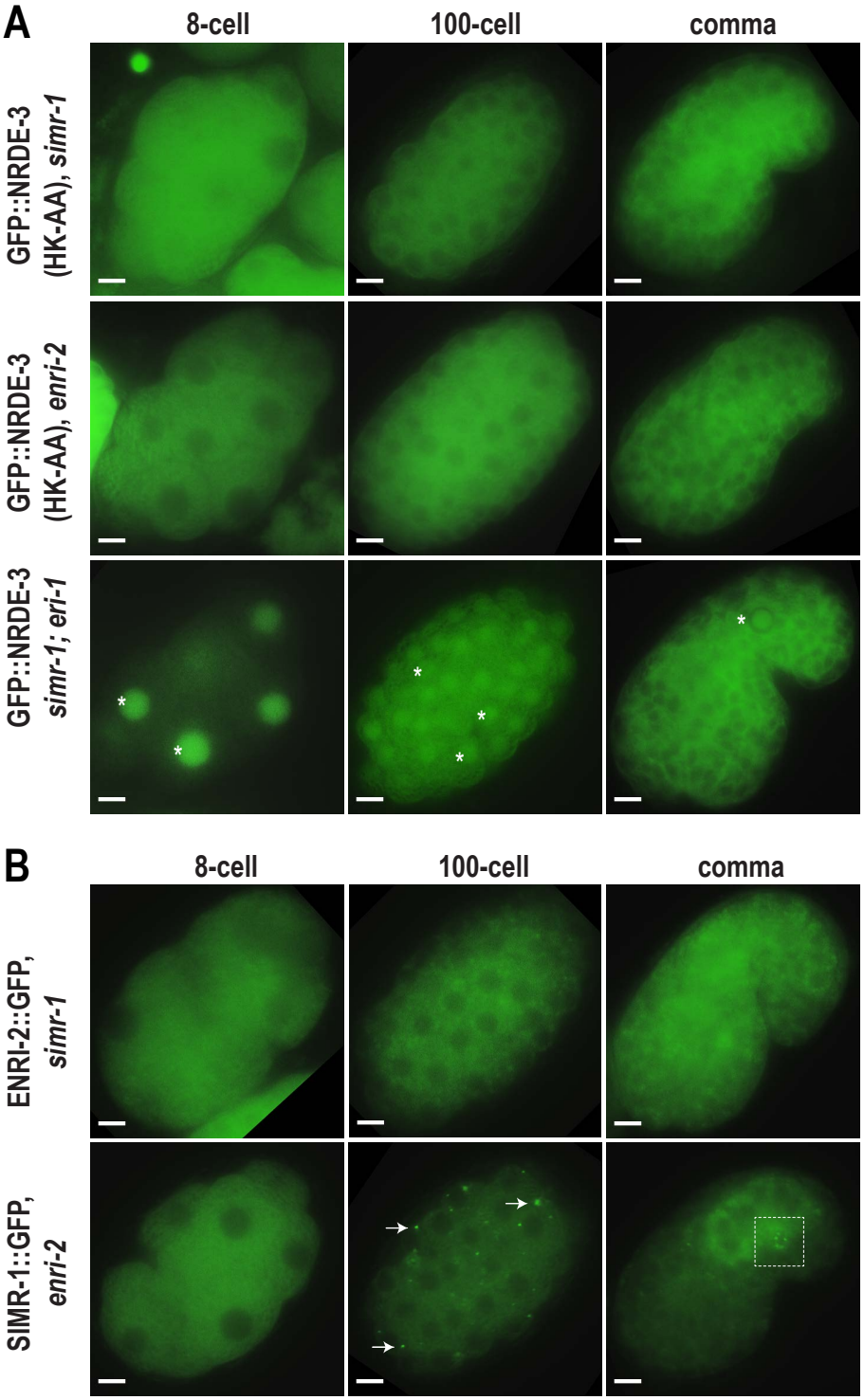

Figure 3. SIMR-1 recruits ENRI-2 and then NRDE-3 to cytoplasmic granules.

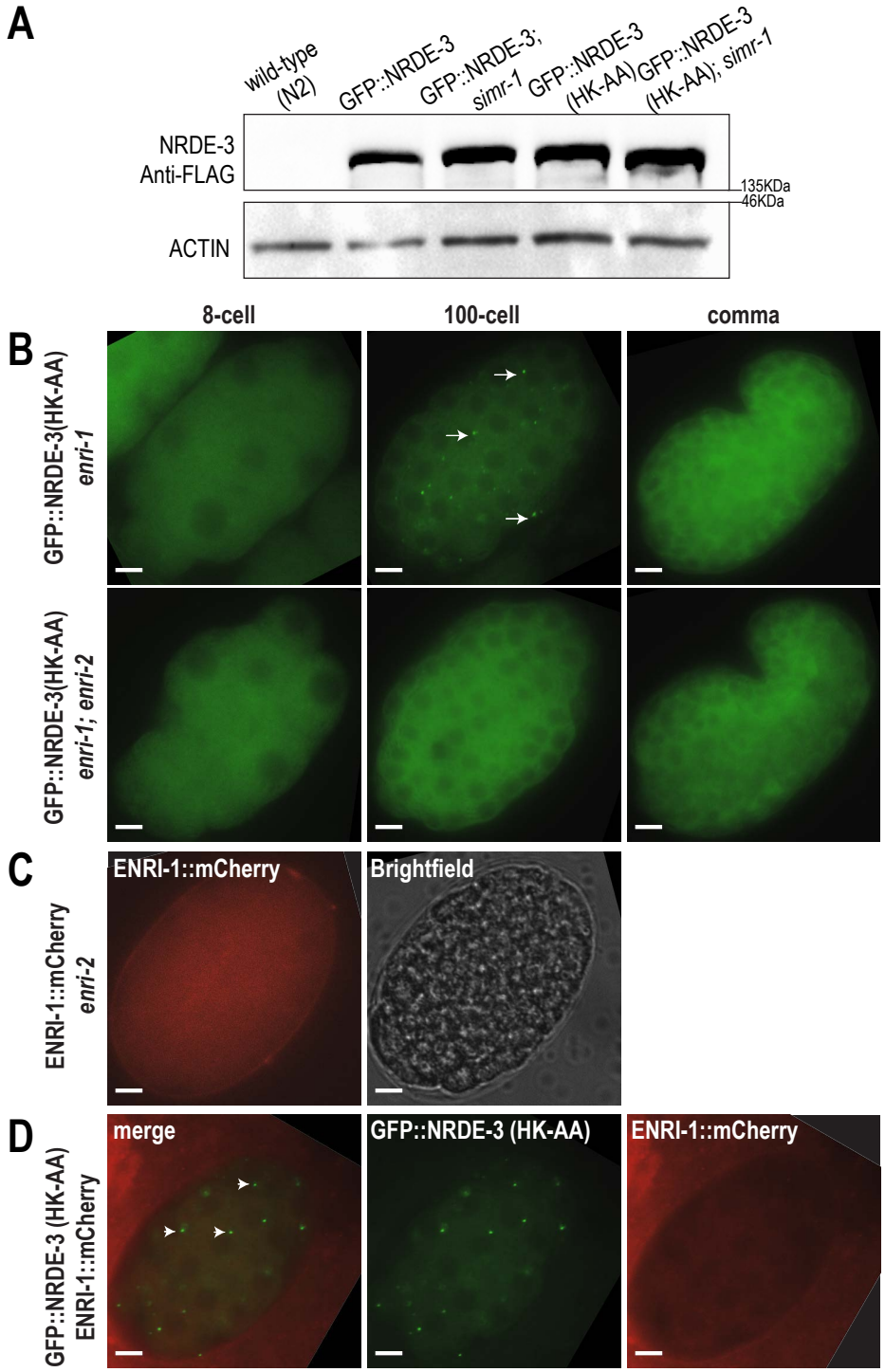

Figure 3—figure supplement 1. NRDE-3(HK-AA) and ENRI-1 localization in various mutants.

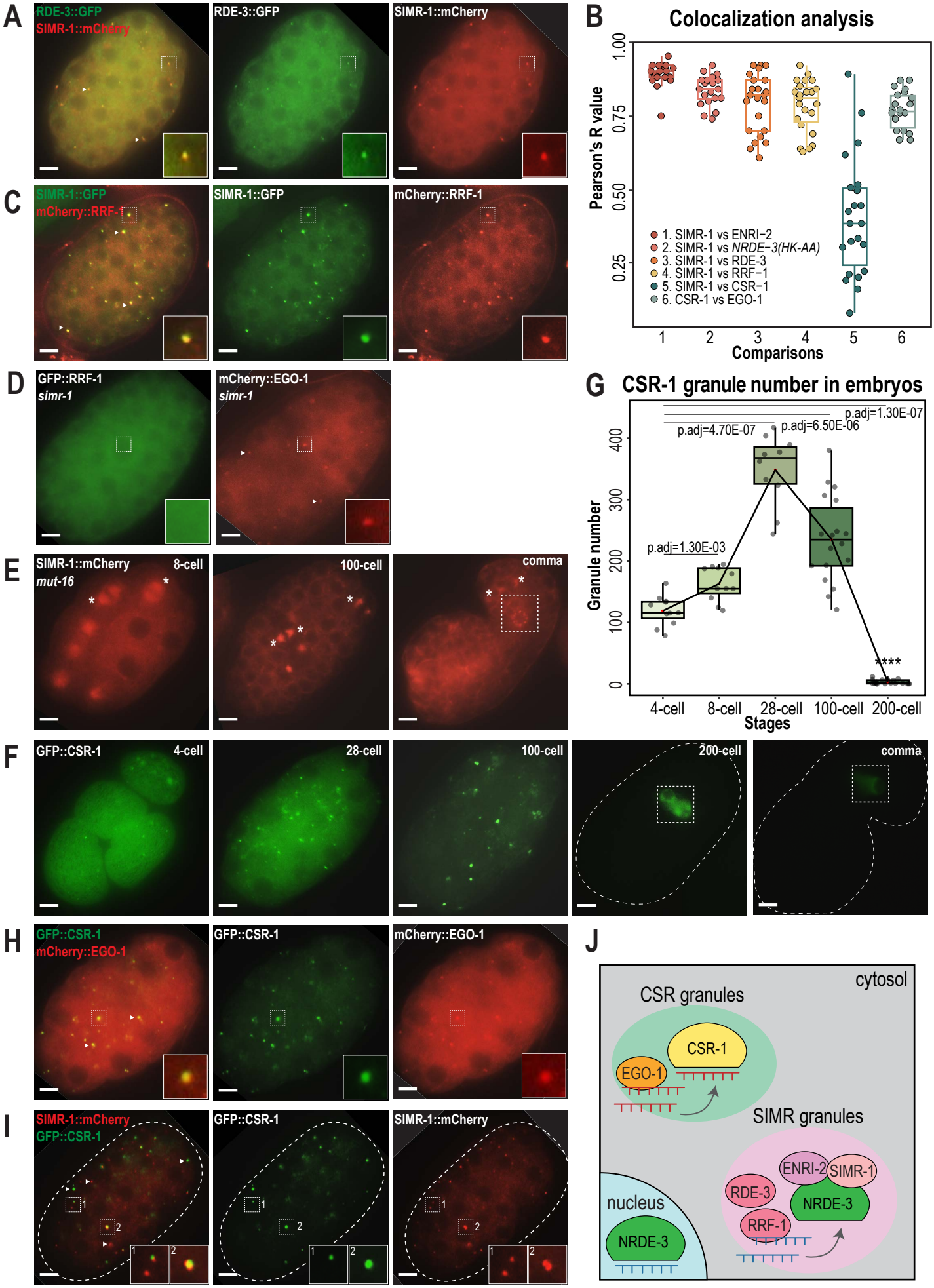

Figure 4. CSR and WAGO pathway proteins localize to distinct cytoplasmic granules.

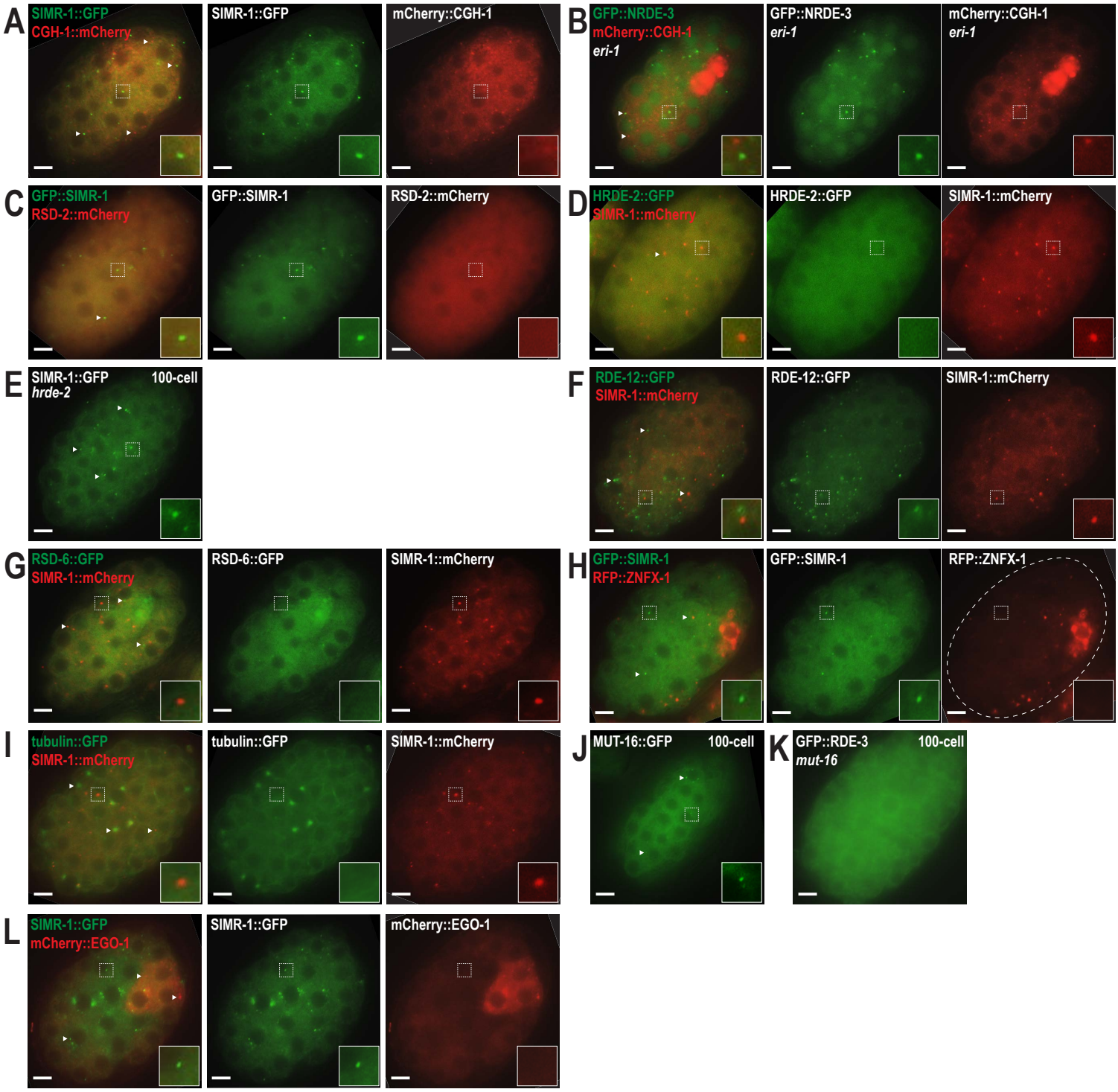

Figure 4—figure supplement 1. SIMR-1 does not colocalize with any previously identified embryonic granules.

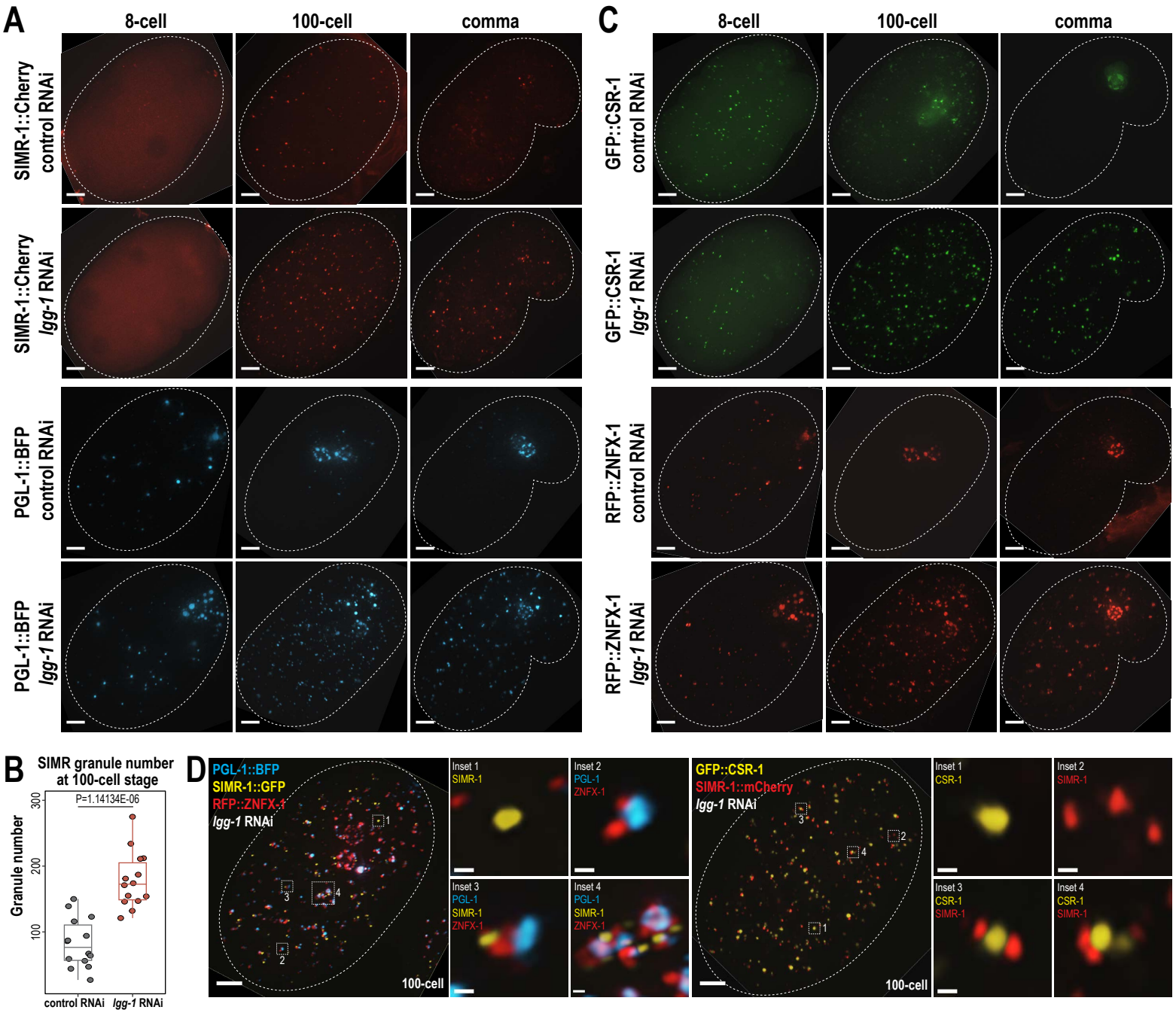

Figure 5. Autophagy regulates the removal of SIMR granules and other embryonic granules.

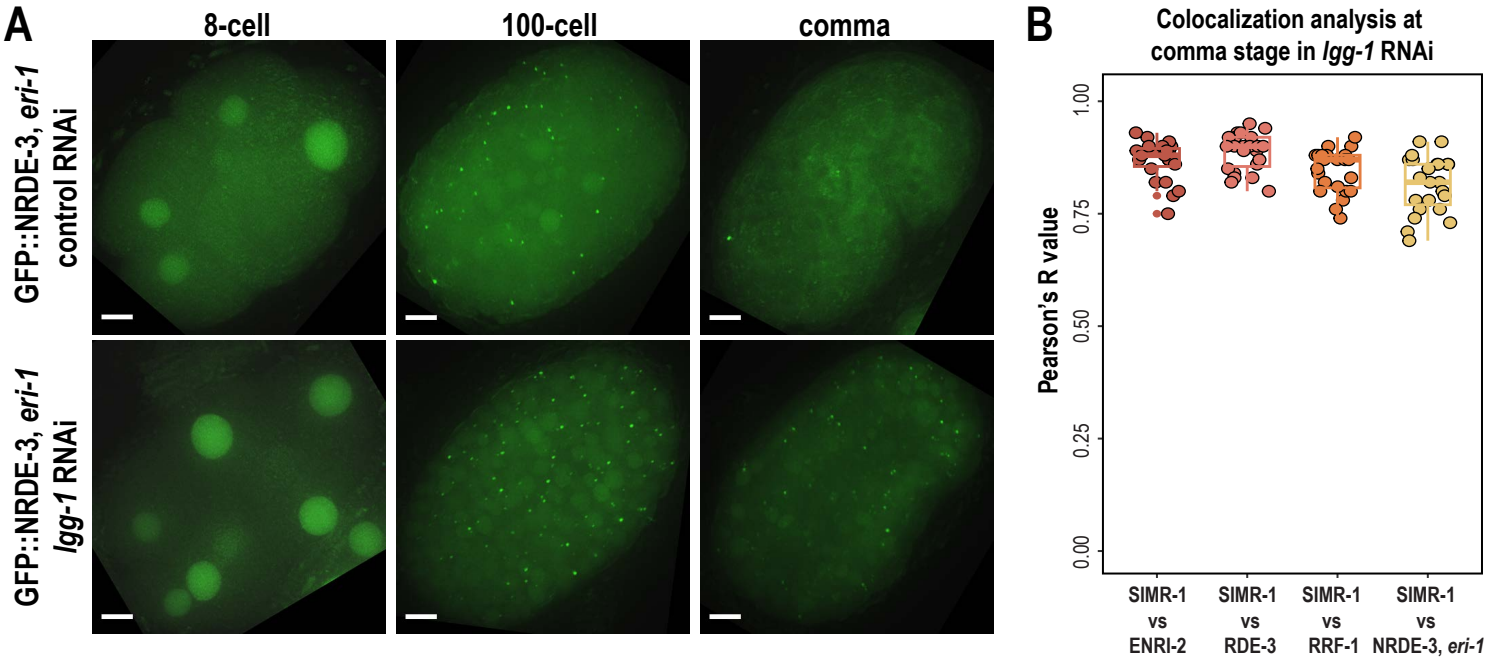

Figure 5—figure supplement 1. Components of the SIMR granule are regulated by autophagy.

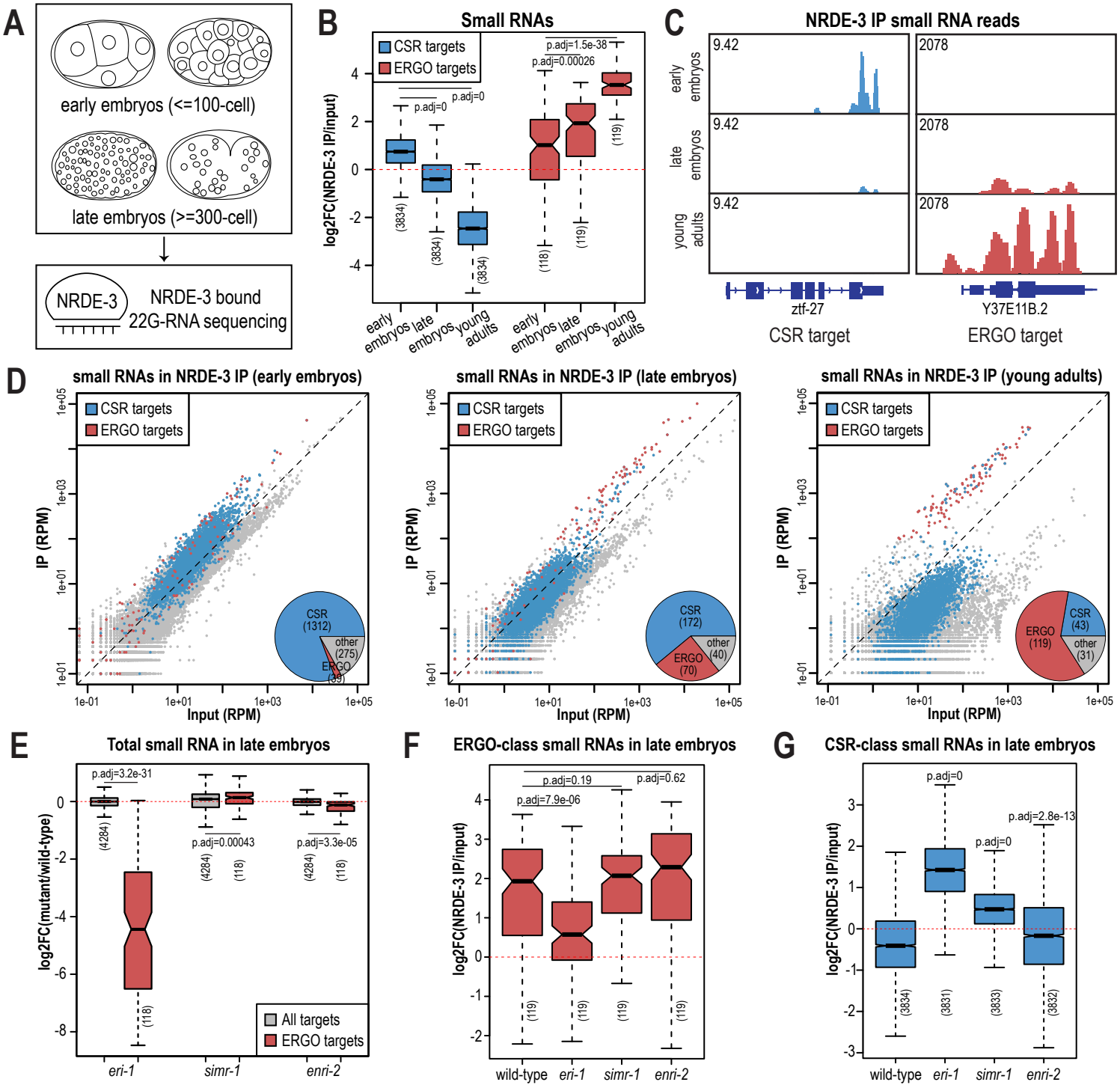

Figure 6. NRDE-3 switches small RNA targets during development.

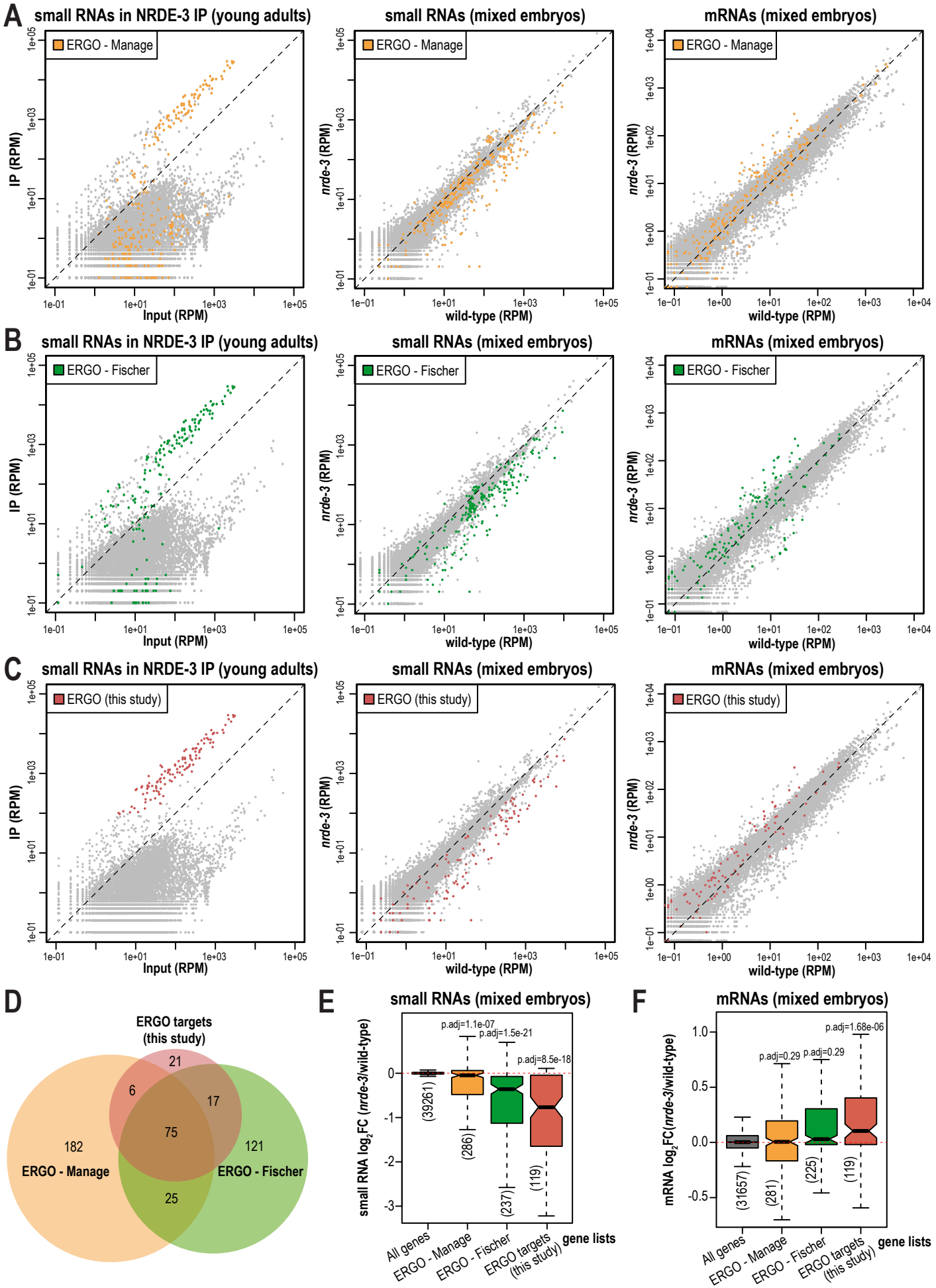

Figure 6—figure supplement 1. Defining NRDE-3-bound ERGO-target genes.

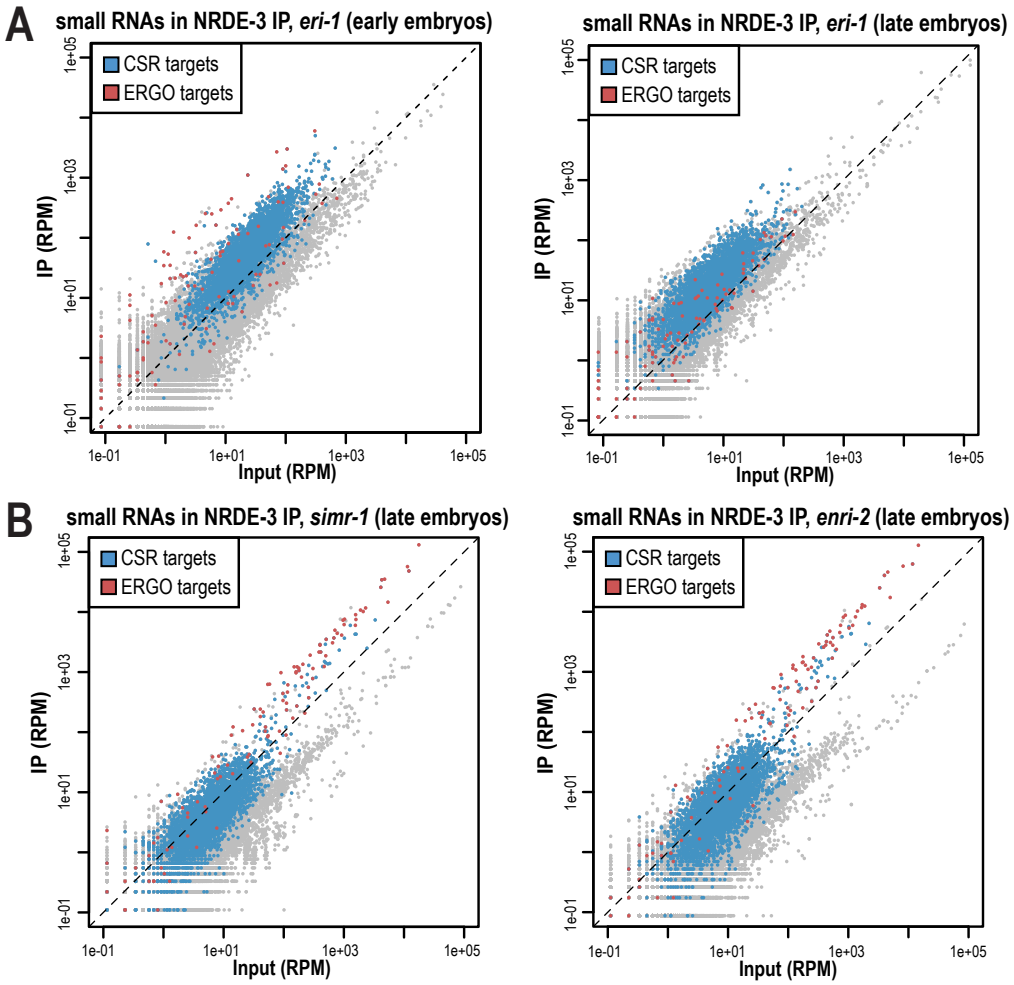

Figure 6—figure supplement 2. NRDE-3 bound small RNA in different mutants.

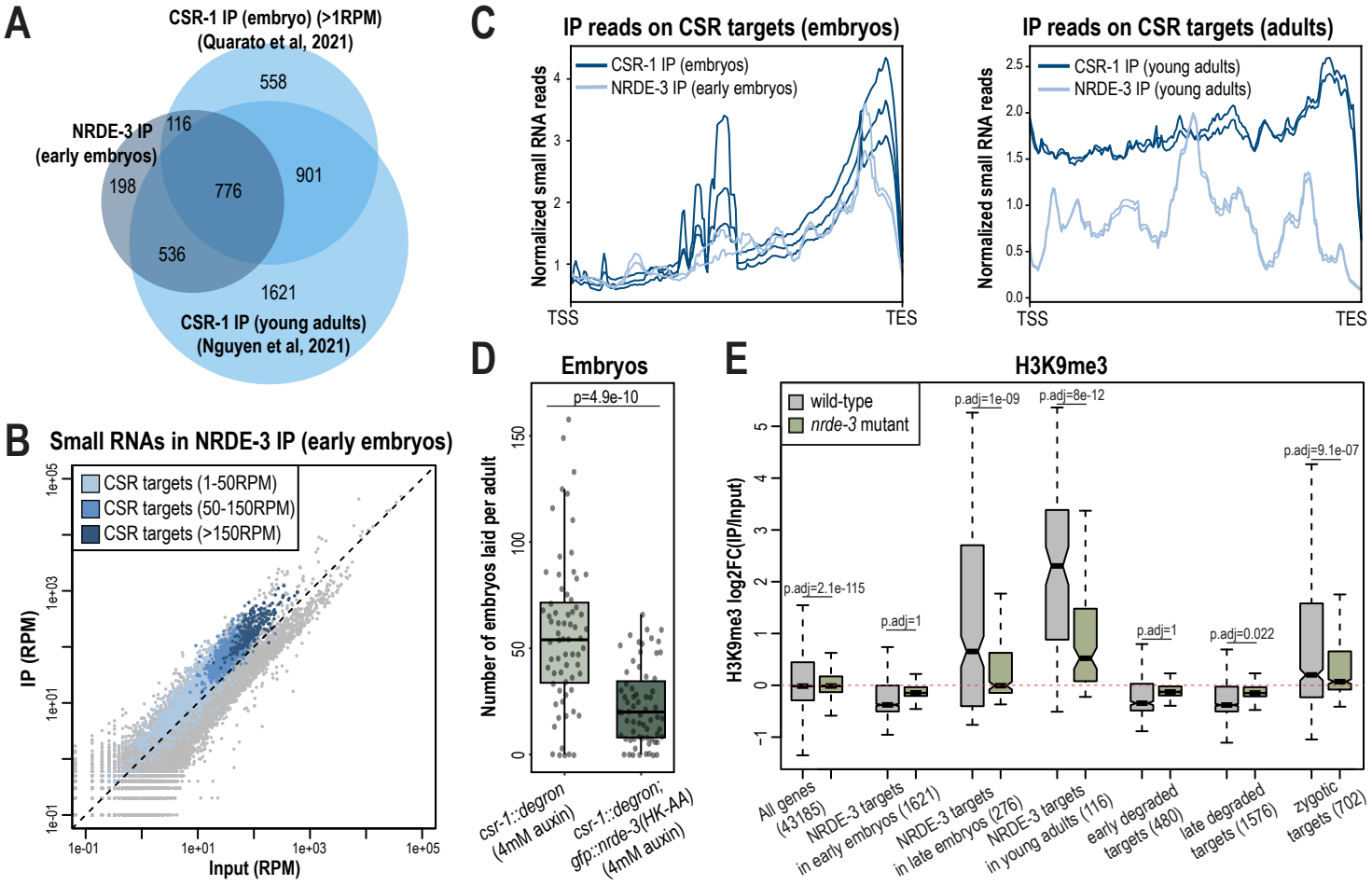

Figure 7. NRDE-3 associates with CSR-class 22G-RNAs in early embryos.

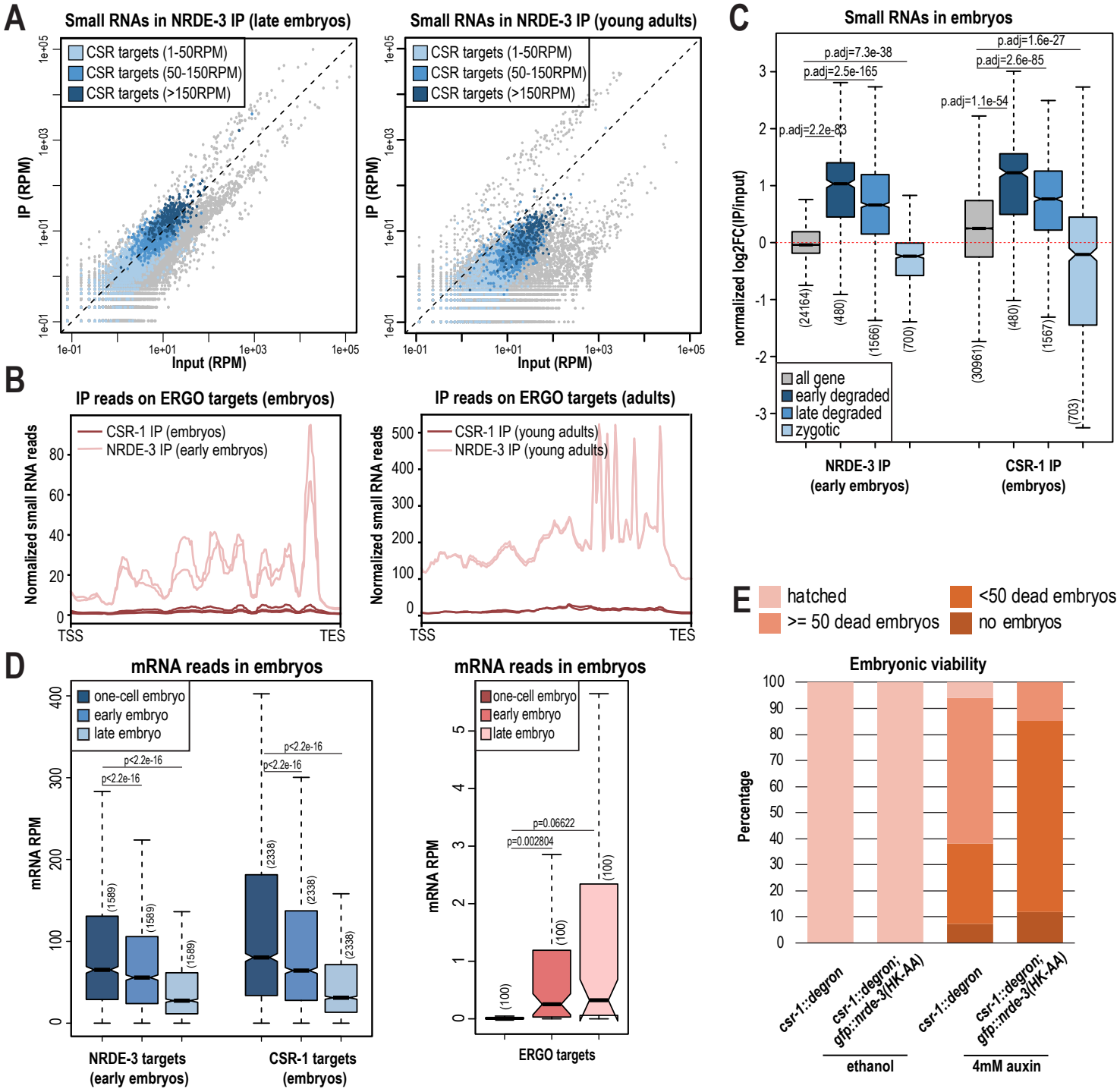

Figure 7—figure supplement 1. NRDE-3 associates different classes of small RNAs during development.

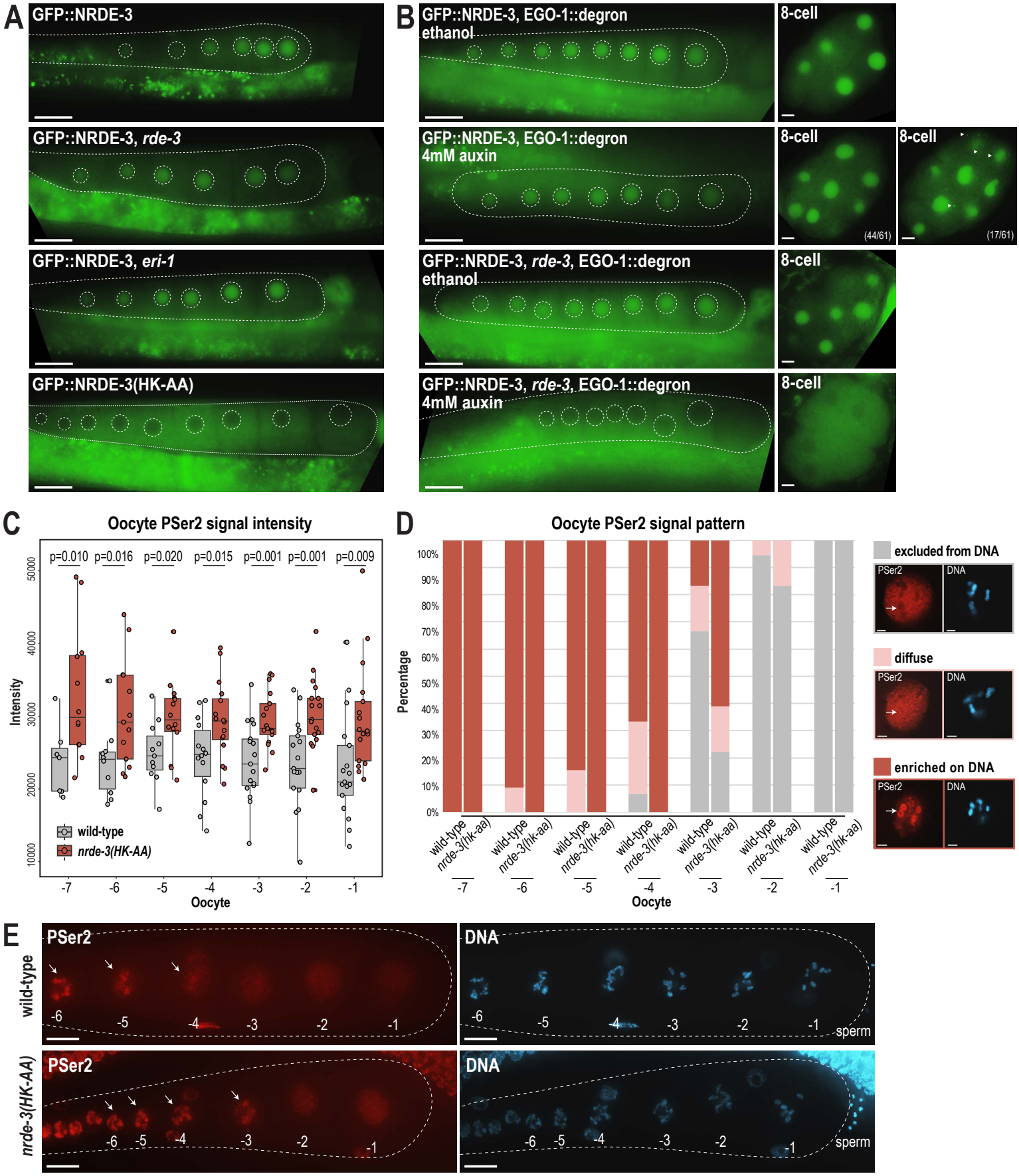

Figure 8. NRDE-3 associates with CSR-class 22G-RNAs to represses RNA Polymerase II in oocytes.

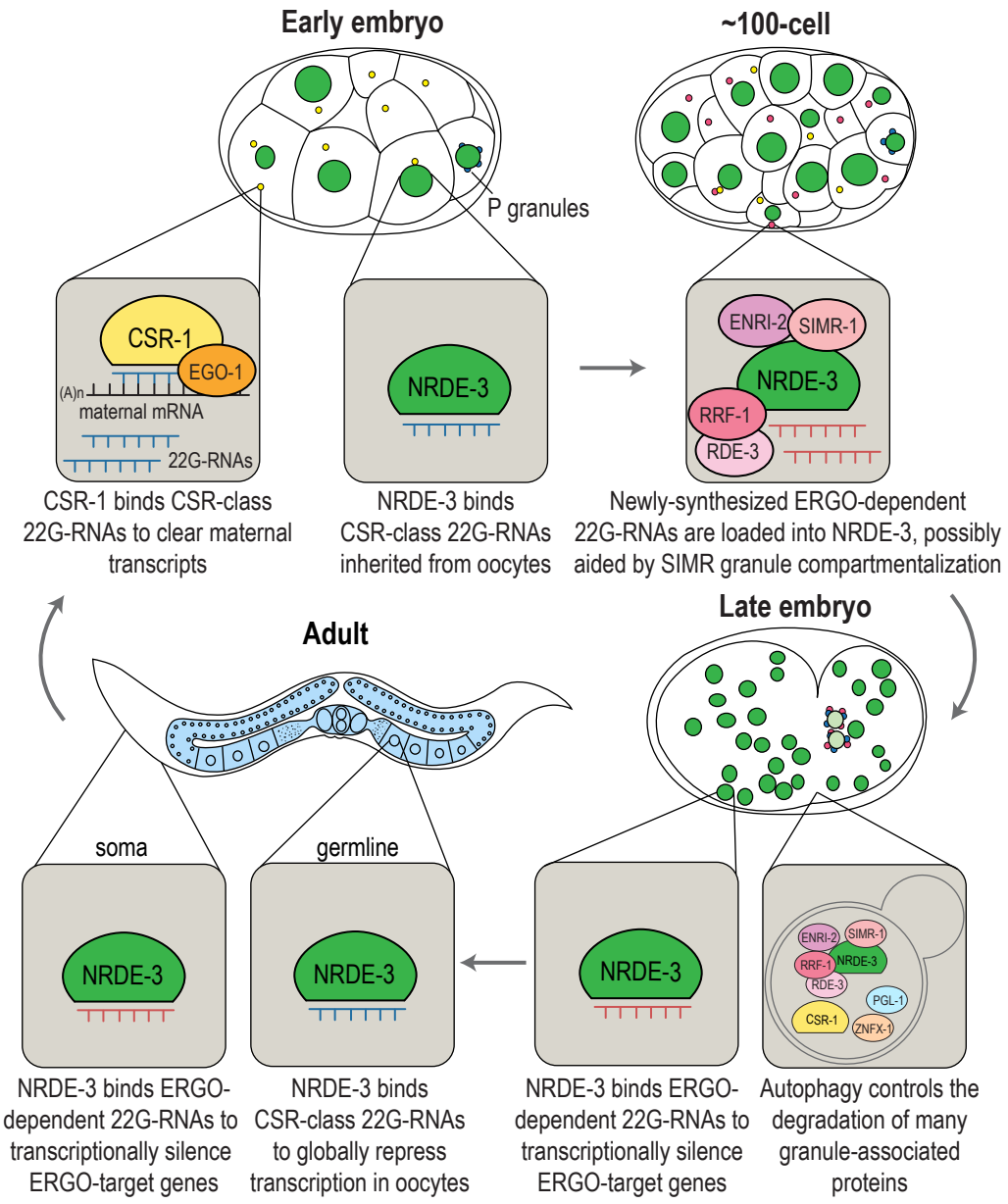

Figure 9. Model for temporally- and developmentally-regulated NRDE-3 function.

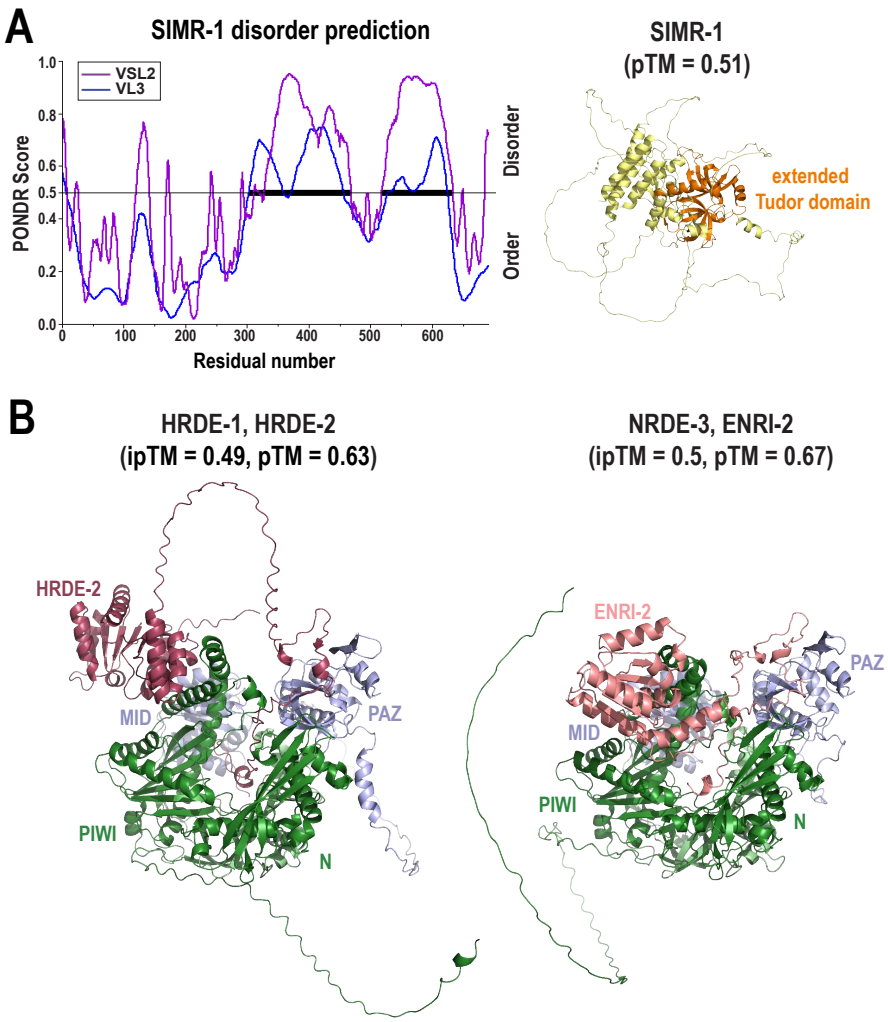

Figure 9—figure supplement 1. Predicted structures of SIMR-1, nuclear Argonaute proteins, and interactors.